Three Flavor Oscillation Analysis of Atmospheric Neutrinos in Super-Kamiokande

by
Roger Alexandre Wendell

A dissertation submitted to the faculty of the University of North Carolina at Chapel Hill in partial fulfillment of the requirements for the degree of Doctor of Philosophy in the Department of Physics and Astronomy.

Chapel Hill
2008

Approved by:

Kate Scholberg

Hugon Karwowski

Tom Clegg

Ryan Rohm

Bruce Carney

ABSTRACT

ROGER ALEXANDRE WENDELL: Three Flavor Oscillation Analysis of Atmospheric Neutrinos in Super-Kamiokande
(Under the Direction of Kate Scholberg)

In this dissertation atmospheric neutrino data from the 50 kiloton water-Cherenkov detector, Super-Kamiokande, are studied in the context of neutrino oscillations. Data presented here are taken from the 1489-day SK-I and 803-day SK-II exposures. Super-Kamiokande's atmospheric neutrino sample exhibits a zenith angle dependent deficit of ν_μ interactions which is well explained by maximal two-flavor $\nu_\mu \leftrightarrow \nu_\tau$ oscillations.

This analysis extends the two-flavor framework to include all active neutrino flavors and searches for sub-dominant oscillation effects in the oscillations of atmospheric neutrinos. If the last unknown mixing angle, θ_{13}, is non-zero there is enhancement (suppression) of the $\nu_\mu \rightarrow \nu_e$ three-flavor oscillation probability in matter for several GeV neutrinos with long baselines under the normal (inverted) mass hierarchy. At Super-Kamiokande this effect would manifest itself as an increase in the high energy ν_e event rate coming from below the detector. Searching the SK-I, SK-II and their combined data finds no evidence of a rate excess and yields a best fit to θ_{13} of zero assuming either hierarchy. This extended analysis remains consistent with the current knowledge of two-flavor atmospheric mixing finding best fit values $\sin^2\theta_{23} = 0.5$ and $\Delta m^2 = 2.6 \times 10^{-3}\text{eV}^2$. No preference for either the normal or inverted mass hierarchy is found in the data.

ACKNOWLEDGMENTS

I would like to offer my humblest thanks to all of the people whose efforts have contributed to this work. Special thanks to Kate Scholberg for her kind patience and guidance throughout the thesis process and to Hugon Karwowski for his efforts to ensure that I left graduate school successful and in a timely manner. Chris Walter has also contributed largely to the success of this dissertation and I am grateful for his mentoring. Many thanks to my committee for their useful insights and comments on my dissertation. In particular I would like to thank Ryan Rohm for his extraordinary generosity of time and ideas and Tom Clegg for introducing me to Carolina BBQ six years ago.

In many ways the graduate experience was only survivable with the support of my friends and colleagues. My original cadre of unlikely heroes in graduate school includes Mike Kavic, Joe Newton, Han Zhang and Dmitri Spivak who through their efforts to keep me well rounded outside of the halls of the physics department have enriched my experience to no end. Jentry Mitchell and Bob Ryan have done their best to keep track of me across the many miles and years to remind me that no matter how long I am strapped to academia I am never that far from where we all started. For that I am particularly grateful. I offer my heartfelt appreciation to Aashish Majethia not only for his collaboration on our dehydrated water patent but more importantly for his open laughter, ears and friendship. I would not have made it here without the enduring support of Emma Huang, nor would I want to have.

As an undergraduate I was fortunate to work in the research group of Richard Kurtz and Roger Stockbauer. Though the work was different from where my path in science has eventually led, the foundations of research they instilled in me nearly

ten years ago are still present today. Their two postdocs during my tenure, Reginaldt Madjoe and Alexey Koveshnikov, deserve special recognition for showing me the "ropes" down to their tiniest threads. I would also like to acknowledge Jonathan Toups for his infectious zeal of scientific exploration both in and outside of the lab.

Though I have had many courses and professors who taught them during my time as a student, I would like to single out two for their efforts to improve me as a scholar and human being. Ravi Rau, through his example and mentoring, has instilled within me a critical eye for the details of the scientific method and with a responsibility to partake in the greater world at large outside of physics. I am humbly grateful for his time and tutelage. Carruth McGehee gave me my first introduction to the beauty in the world of mathematics. Moreover, throughout my time as an undergraduate his careful attention to fostering my interests in physics, mathematics, and beyond have made him a valuable mentor and more importantly a great friend.

I would like to thank my collaborators on the Super-Kamiokande experiment. Special thanks goes to Parker Cravens for his unquenchable conversation and to Mike Litos for ensuring I graduate by not attending a North Carolina institution himself. To Jen Raaf I offer my warm thanks for her advice, compassionate ready-to-be-lent-ears and above all, her friendship.

Thanks kindly to Maxim Fechner for his need to protect his family of varying ethnicities and for his sage advice; to Ariana Minot for her warm friendship, mints and bubble teas; to Naho Tanimoto for enriching my life and understanding; and to the neutrino group at Duke, which has been an excellent source of friendship and collaboration - my gratitude goes to you all.

In closing, the love and support of my family, extended and immediate, has been invaluable. Most of all, I thank Dad, Moppy and Amby for their many words of advice, congratulations, encouragement and love.

To My Family

CONTENTS

LIST OF ABBREVIATIONS

MC	Monte Carlo
CC	Charged Current
NC	Neutral Current
FC	Fully Contained
PC	Partially Contained
C.L.	Confidence Level
ID	Inner Detector
OD	Outer Detector
QE	Quasi-Elastic

LIST OF FIGURES

LIST OF TABLES

Chapter 1

Introduction

Physical theories involving neutrinos have existed for more than 70 years and though neutrinos have been the subject of experimental studies for more than 50 years, neutrino physics did not enter the realm of precision science until roughly the last decade. In light of how extremely ubiquitous neutrino are, with billions traversing each cubic centimeter of the Earth every second, this protracted period of scientific development is a testament to their mysterious nature. Indeed, they enter the sea of ordinary particle discourse only through the weak interaction making their reactions with other matter rare and hence difficult to observe despite their large numbers. The problem is further complicated by their ability to spontaneously convert from one observable type (flavor) into another. It is the combination of these two phenomena which has generated increasing interest in their behavior recently.

Wolfgang Pauli postulated the existence of the neutrino in 1930 in an attempt to explain the continuous energy spectrum of β particles emitted in nuclear decays. The process was thought to be a two-body decay which should accordingly produce a discrete energy spectrum. Pauli realized that the spectrum could be explained if a hitherto unobserved neutral spin-1/2 particle with mass not more than that of the electron were among the decay products [2]. In 1934 Fermi created a successful theory based on this three-body decay, modeling the process as the conversion of a neutron into a proton, electron and calling Pauli's third particle the "neutrino [3]."

Pontecorvo suggested [4] in 1946 that by using an inverse β decay process, $\bar{\nu} + p \rightarrow$

$n + e^+$ it is possible to observe neutrinos. Using $CdCl_2$-doped water, Reines and Cowan exploited this reaction to make coincidence measurements of gamma rays from the positron's annihilation with gamma rays from the neutron's delayed capture on cadmium. The experiment was performed at the Savannah River nuclear facility and was the first observation of this electron anti-neutrino [5, 6], for which Reines earned the 1995 Nobel Prize in physics.

Since its discovery the neutrino has enjoyed a considerable amount of attention. It is now known to be a neutral spin-1/2 fundamental particle and is a member of the family of leptons. For each of the charged leptons there is an associated neutrino, the muon neutrino being first observed in 1962 [7] and the tau neutrino in 2001 [8]. With the unification of the electromagnetic and weak forces, the neutrino was thought to be massless and after precision measurements of the width of the Z^0 decay it was shown that there are only three light active neutrinos [9]. Neutrinos are now known to be produced in the nuclear processes of stars, in the natural decays of elements within the Earth's interior, and through the interaction of cosmic rays with the atmosphere. They can even be created artificially at beam lines through the decays of hadrons. Against this backdrop there remains a wealth of information to be learned about their nature.

1.1 Atmospheric Neutrinos

Neutrinos born in the Earth's atmosphere are the focus of this dissertation. Cosmic rays impinging on the atmosphere collide with air nuclei creating pions and occasionally kaons whose subsequent decays produce neutrinos:

$$p + N_{air} \rightarrow \quad \pi^+ \quad + \ldots \tag{1.1}$$

$$\hookrightarrow \quad \mu^+ + \ \nu_\mu \tag{1.2}$$

$$\hookrightarrow \quad e^+ + \nu_e + \bar{\nu}_\mu. \tag{1.3}$$

Note that there are two muon neutrinos and only one electron neutrino. The sister decay of the π^- has in its final state the same pair of muon neutrinos and one electron

anti-neutrino. With this observation the ratio $(\bar{\nu}_\mu + \nu_\mu)/(\bar{\nu}_e + \nu_e)$ is expected to be around two below 1 GeV. Higher energy neutrinos come from more energetic parents, which in the case of muons may reach the surface of the Earth before decaying. Consequently, the number of electron neutrinos decreases and the ratio increases with energy (see for instance Figure 4.2).

Though the uncertainty on the individual fluxes below 100 GeV is roughly 14%, the present error on their ratio is $\sim 2\%$ [10]. Moreover, since the flux of cosmic rays is isotropic about the planet, the flux of neutrinos coming from above the horizon is expected to be roughly the same as from below. Coupled with their enormous variation in path length ($O(10) - O(10^4)$ km) and energy (100 MeV - 1 TeV), this attribute makes atmospheric neutrinos a robust source for studying neutrino oscillations.

1.2 Neutrino Masses

Several limits exist on the masses of the neutrinos. Direct measurements of the electron neutrino mass are made by studying the tail end of tritium β-decay energy spectrum. Currently its mass is constrained to be less than 2.3 eV/c^2 [11], well below the electron's mass. Similarly, by measuring the muon energy spectrum from pion decay at rest, $\pi^+ \rightarrow \mu^+ + \nu_\mu$, an upper limit on the mass of the muon neutrino has been set at 170 keV/c^2 [12]. Limits on the mass of the tau neutrino have been based on the hadronic decays of the tau lepton such as, $\tau^- \rightarrow 2\pi^-\pi^+\nu_\tau$, and restrict its value to be less than 18.2 MeV/c^2 [13].

Direct measurements are not the only means of studying the neutrino mass. Since relativistic neutrino do not cluster they effect the formation galaxy clusters and massive neutrinos lead to a suppression of the matter power spectrum at small scales. Using this property, the authors of Ref. [14] have used data from several experiments measuring comosological structure to compute an upper limit on the sum of the neutrino mass eigenvalues, $\sum_i m_i < 0.75$ eV/c^2. Neutrinoless double-β decay experiments

search for the decay

$$ {}^{Z}_{A}\mathrm{N} \rightarrow {}^{Z+2}_{A}\mathrm{M} + 2e^{+}, \tag{1.4} $$

a reaction which is only possible if neutrinos are Majorana fermions. The decay rate is proportional to a weighted average of the Majorana mass states whose upper limit has recently been measured as $\langle m_{\nu} \rangle < 0.19 - 0.68$ eV/c^2 [15].

Despite the consistent smallness of these measured limits there is now firm evidence that the neutrino mass is non-zero. This evidence comes in the form of neutrino oscillations. If the neutrino electroweak eigenstates are a superposition of their mass eigenstates, and the mass eigenvalues are non-degenerate and non-zero, then the neutrino may "oscillate" from one flavor to another repeatedly as it travels. In the simplest of oscillation modes the frequency is proportional to the difference between the squares of the masses, $\Delta m^2 \equiv m_2^2 - m_1^2$, and its oscillation amplitude is controlled by a mixing angle θ:

$$ P(\nu_{\alpha} \rightarrow \nu_{\beta}) = \sin^2 2\theta \sin^2 \left(\frac{1.27 \Delta m^2 L}{E} \right), \tag{1.5} $$

where L (km) is the neutrino path length in and E GeV its energy. Oscillation experiments using a variety of neutrino sources have determined that there are two such independent mass splittings, and three associated mixing angles that control the amount of oscillation among the neutrino flavors.

Oscillation experiments use Equation 1.5 to search for energy and path length dependent differences in a known flux of neutrinos. Appearance experiments search for an excess of ν_{β} in a beam of ν_{α}. The amount of appearance may then be used to infer limits on Δm^2 and $\sin^2 2\theta$. On the other hand, disappearance measurements look for a reduction in the ν_{α} rate as an indication of oscillations to ν_{β}.

The current status of experimental knowledge of neutrino oscillations is summarized below and the theoretical details are presented in Chapter 2.

1.3 Experimental Status

Neutrino oscillation probabilities are a function of both the neutrino energy and the distance that the neutrino travels. By a suitable choice of either or both, experiments become sensitive to particular domains of oscillation space. Currently there are two primary domains of oscillation: lower frequency "solar" oscillations driven by a small mass splitting and higher frequency "atmospheric" oscillations regulated by a comparatively large mass splitting.

1.3.1 Solar Neutrino Oscillation Experiments

Solar neutrino oscillations have been studied through measurements of the low energy neutrinos produced by the sun's nuclear processes. Approximately 98% of the neutrino flux comes directly from the fusion of protons into helium,

$$4p \rightarrow {}^4\mathrm{He} \ + \ 2\mathrm{e} \ + \ 2\nu_e.$$

However, the neutrinos produced at this stage are difficult to observe because of their low energy. Other significant sources of the flux however come from the β-decay of heavier nuclei produced in separate branches of this process. The fusion of an intermediate ^{3}He nucleus to an existing ^{4}He creates ^{8}B,

$$\begin{aligned} {}^3\mathrm{He} \ + \ {}^4\mathrm{He} &\rightarrow \ {}^7\mathrm{Be} \ + \ \gamma \\ {}^7\mathrm{Be} \ + \ p &\rightarrow \ {}^8\mathrm{B} \ + \ \gamma, \end{aligned}$$

whose decay produces a neutrino with an energy peaking near a more readily observable 8 MeV.

Early radiochemical experiments measured this flux by counting nuclei which are converted into chemically separable species by the electron neutrino's charged current interaction. The Homestake experiment extracted ^{37}Ar atoms from the inverse β-decay of Cl atoms in a reservoir of C_2Cl_4. The experiment ran continuously for nearly 30 years, reporting a final rate of 2.56 interactions per 10^{36} target atoms per second (SNU) [16, 17], against a solar model prediction of 7.6 SNU. Other experiments using

^{71}Ga based targets, SAGE[18, 19] and GALLEX [20, 21] observed this flux deficit which became known as the "solar neutrino problem."

The Kamiokande and Super-Kamiokande water-Cherenkov experiments observe solar ^{8}B neutrinos via neutrino-electron elastic scattering (ES), $\nu_e + e^- \rightarrow \nu_e + e^-$. Both the observed flux at Kamiokande, $2.80 \pm 0.19(\text{stat.}) \pm 0.33(\text{syst.}) \times 10^6$ cm^{-2}s^{-1} [22], and at Super-Kamiokande, $2.35 \pm 0.02 \pm 0.08$ [23], exhibit a deficit relative to a predicted flux of 5.6 from the model in Ref. [24]. However, they are consistent with neutrino oscillations arising from a mass splitting $10^{-8} < \Delta m^2 < 10^{-4}$ eV^2.

Experiments at the Sudbury Neutrino Observatory (SNO) confirmed the oscillation hypothesis by showing there exists an active component to the solar ^{8}B flux beyond the ν_e flux observed above. Using a heavy-water target the SNO experiment studied both neutral-current (NC) and charged-current (CC) scattering off deuterium nuclei in addition to the ES process through the reactions

$$CC: \quad \nu_e + d \rightarrow e^- + p + p \tag{1.6}$$

$$NC: \quad \nu_x + d \rightarrow \nu_x + p + n, \tag{1.7}$$

where ν_x indicates any neutrino flavor. A neutron liberated in the NC reaction will later thermalize and capture on deuterium producing a 6.5 MeV gamma ray. Separation of this signature from the Cherenkov light produced in the ES and CC reaction is done statistically and provides the result shown in Figure 1.1. For each of the three interaction types, the fluxes of ν_e and non-ν_e (ν_μ, ν_τ) components are shown in three bands which intersect. This intersection suggests strongly that the solar neutrino flux is not composed entirely of ν_e. That is, the ν_e flux deficit can be accounted for by oscillations into the other active neutrino flavors, ν_μ and ν_τ.

Another important contribution to solar neutrino oscillation physics came from the KamLAND experiment. KamLAND uses an organic liquid scintillator to observe $\bar{\nu}_e$ coming from local nuclear power plants. These neutrinos have energies similar to those of solar neutrinos and should therefore be subject to the same kind of oscillation phenomena. In the reaction of interest, $\bar{\nu}_e + p \rightarrow e^+ + n$, prompt scintillation light is seen from the outgoing positron and light from a 2.2 MeV gamma ray emitted when the

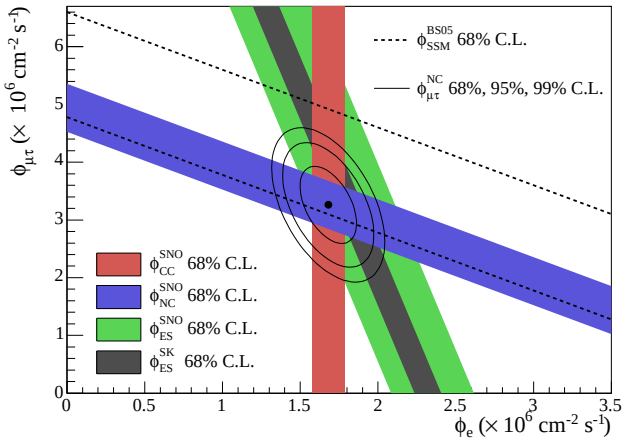

Figure 1.1: ^{8}B ν fluxes extracted from each of the SNO salt phase[25] data samples shown as colored bands whose width represents 1-σ confidence. Dashed lines are the prediction from [24] and the circular contours represent the best fit to all of the data. The Super-K elastic scattering measurement appears in grey.

neutron captures on a proton is seen some 200 μs later. After a 764 ton-year exposure KamLAND observed 258 $\bar{\nu}_e$ candidates against an expectation of 365.2 ± 23.7. This discrepancy is consistent with neutrino oscillations at $\Delta m^2 = 7.9^{+0.6}_{-0.5} \times 10^{-5}$ eV^2 [26]. Assuming CPT invariance this result can be added to the global oscillation fit among all solar neutrino measurements to place a strong constraint on the mass splitting as well as the mixing angle as shown in Figure 1.2.

1.3.2 Atmospheric Neutrino Oscillation Experiments

Early atmospheric neutrino experiments sought to measure the flux of muon neutrinos relative to electron neutrinos, $R \equiv (\nu_\mu + \bar{\nu}_\mu)/(\nu_e + \bar{\nu}_e)$ and frequently reported the double ratio, R_{data}/R_{MC}. The Kamiokande experiment measured this double ratio to be $0.60^{+0.07}_{-0.06}(\text{stat.}) \pm 0.05(\text{syst.})$ [27]. When the IMB water-Cherenkov experiment and the Soudan-2 iron tracking-calorimeter experiment later reported similar values [28, 29, 30] the existence of an "atmospheric neutrino anomaly" was established.

Much like the solar neutrino problem, however, the deficit of muon events can be interpreted as evidence for neutrino oscillations but at a mass difference much larger

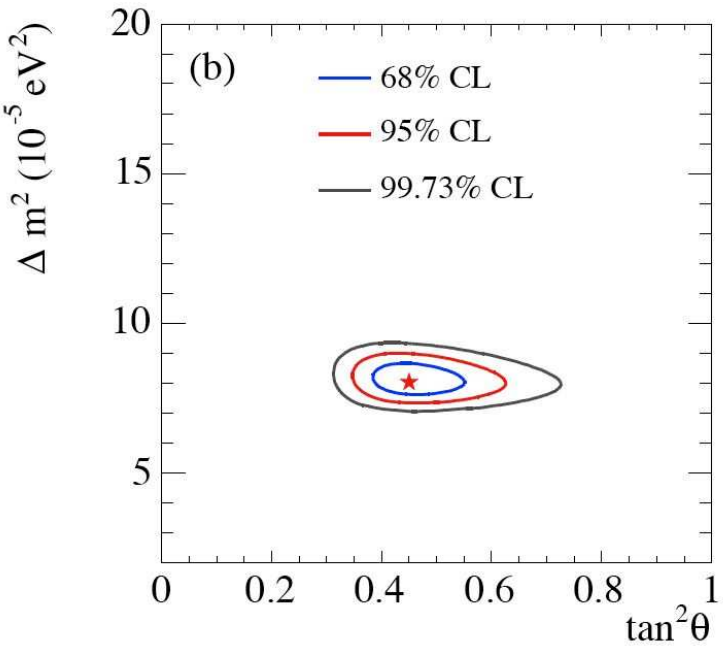

Figure 1.2: The oscillation contours from a global fit of solar neutrino data, taken from Ref. [25]

than that of the solar oscillations. The Kamiokande collaboration observed a high energy zenith angle dependence in the distribution of the double ratio [31] consistent with ν_μ disappearance at $\Delta m^2 \approx 10^{-2}$ eV^2 and $\sin^2 2\theta = 1.0$.

Other experiments confirmed this disappearance with measurements of the flux of high energy muons coming from beneath the horizon. These muons are created by CC ν_μ interactions in the rock below the detector and hence changes in the neutrino flux translate into changes in the observed muon flux. Soudan-2 observed a 50% reduction relative to Monte Carlo expectation in its upward going muon-like events, with no deviation seen in the electron-like sample [30]. This measurement is described well by no ν_e oscillations and ν_μ disappearance bounded by $\Delta m^2 < 0.025$eV^2 with a large mixing angle. Later, the MACRO experiment, a large underground composite detector, refined this measurement after observing a clear deficit of upward going muons corresponding to oscillations at $10^{-3} < \Delta m^2 < 6.5 \times 10^{-3}$ eV^2 and $\sin^2 2\theta > 0.8$ [32].

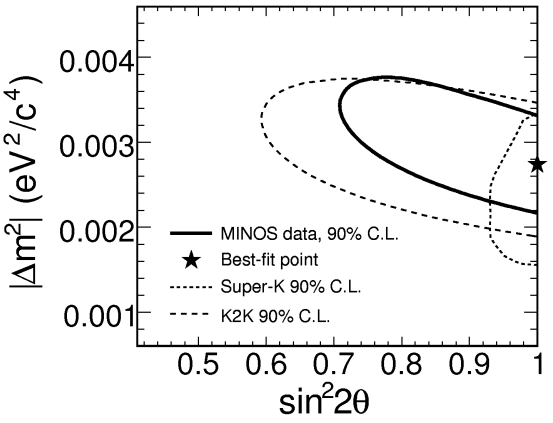

Figure 1.3: 90% C.L. contours for $\nu_\mu \leftrightarrow \nu_\tau$ oscillations. The best fit point shown is from the MINOS data at $\Delta m^2 = 2.74 \times 10^{-3}$ eV^2 with maximal mixing. Taken from [35].

Super-Kamiokande has also made measurements of atmospheric neutrino oscillation parameters using several event sub-samples and analysis techniques. Several of its muon-like samples show good agreement with the oscillation hypothesis, while electron-like samples remain consistent with no disappearance of ν_e. Analyzing these data in a two-flavor oscillation framework further confines the oscillation parameters to the region defined by $\sin^2 2\theta > 0.92$ and $1.5 \times 10^{-3} < \Delta m^2 < 3.4 \times 10^{-3}$ eV^2 [33]. Using a sub-sample with reconstructed resolution in the ratio of path length to energy ratio (L/E) better than 70%, Super-K also observed a dip in the L/E distribution corresponding to the first maximum of the neutrino oscillation probability. This result is direct evidence that the atmospheric data can be explained by the sinusoidal predictions given by $\nu_\mu \leftrightarrow \nu_\tau$ oscillations and disfavors other neutrino disappearance models [34]. Allowed regions from the analyses are shown in Figure 1.3.

1.3.3 Accelerator and Reactor Experiments

Neutrinos can also be produced for study artificially as by-products of nuclear power generation, or from the decays of particles produced at an accelerator. Experiments observing using these sources have the advantage of being able to choose the

neutrino path length (baseline) and energy, allowing selective study of specific regions of the oscillation parameter space.

The K2K long baseline experiment creates neutrinos through the decay of pions created when energetic protons collide with an aluminum target. Pions streaming out the target are magnetically focused into a decay volume where their decay provides a highly pure beam of roughly 1.5 GeV ν_μ. An ensemble of detectors near the beamline is used to measure the beam energy and profile to predict the spectrum at the far detector, Super-K, some 250 km away. At this baseline and energy K2K is able to explore the same region of oscillation parameter space as atmospheric neutrino experiments. K2K observed 112 interactions at Super-K against an expectation of $158.1^{+9.2}_{-8.6}$ events in the absence of neutrino oscillations[36]. Together with the distortion of the Super-K event's energy spectrum this deficit is well described by $\nu_\mu \leftrightarrow \nu_\tau$ oscillations with $1.9 \times 10^{-3} < \Delta m^2 < 3.5 \times 10^{-3}$ eV^2 [36].

MINOS is another long-baseline beamline experiment using hadron decays to create a nearly pure beam of ν_μ. The far detector is 735 km away from the 3 GeV neutrino source. Like the K2K experiment, the MINOS data is again at odds with the no-oscillation hypothesis: it has an observed 215 events relative to an expected 336 ± 14. These data are best fit by an oscillation model in the atmospheric regime with maximal mixing at $\Delta m^2 = 2.74 \times 10^{-3}$ eV^2 [35]. Figure 1.3 shows the oscillation contours for several experiments including the MINOS result.

An experiment at Los Alamos National Laboratory, LSND, observed evidence of neutrino oscillations that did not fit well with results above. LSND used 167 tons of liquid scintillator located 30 m from the neutrino source to observe both ν_e and $\bar{\nu}_e$ appearance in a beam of muon neutrinos. Neutrinos were produced using a decay-in-flight technique similar to the MINOS and K2K, but because of the lower proton beam energy of 800 MeV the resulting neutrino energies range up to 50 MeV. The LSND observation was made using the at-rest decay of positive muons from stopped pions to produce anti-neutrinos and an excess of $87.9 \pm 22.4 \pm 6.0$ events was reported. Combining these two measurements under an oscillation hypothesis suggests neutrino

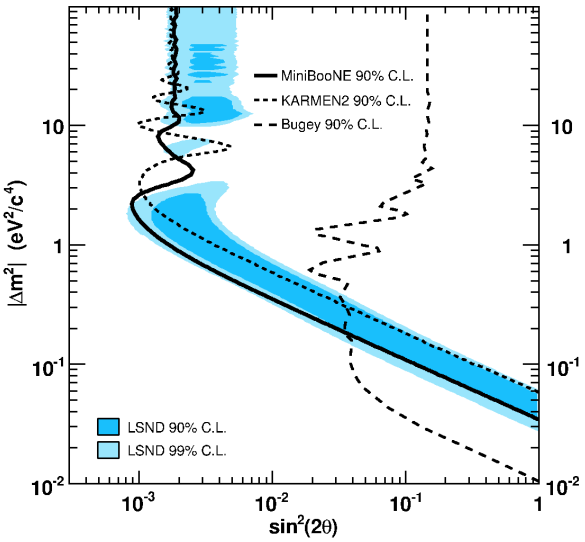

Figure 1.4: Allowed and exclusion contours for various experiments searching for ν_e appearance at large values of Δm^2. The LSND anomaly discussed in the text has been addressed by the MiniBooNE collaboration in Ref. [40] from which this plot is taken.

oscillations $\bar{\nu}_\mu \leftrightarrow \bar{\nu}_e$ occur with small mixing at $\Delta m^2 \sim 1$ eV^2 [37], a value two orders of magnitude larger than the atmospheric mixing mass-squared difference.

What later became know as the LSND anomaly has been further studied by two other collaborations. The KARMEN2 liquid scintillator experiment looked for the appearance of $\bar{\nu}_e$ in a beam of $\bar{\nu}_\mu$ using a decay at rest source. Their observations were consistent with no excess of $\bar{\nu}_e$ and exclude a large swath of the LSND signal region[38]. However, the experiments were still shown to be compatible at the 64% C.L.[39]. More recently, the MiniBooNE experiment, also a liquid scintillator experiment, built with the intent of testing the LSND result, has published a search for $\nu_\mu \rightarrow \nu_e$ in a neutrino beam produced by the in-flight decay of muons. MiniBooNE observes no excess of ν_e for events excluding two-flavor neutrino oscillations of the LSND type at 90% confidence [40]. Figure 1.4 shows the allowed and subsequent excluded regions surrounding the LSND question. Though MiniBooNE appears to resolve the LSND anomaly, the authors of Ref. [41] have suggested that the two experiments are compatible if there exists CP-violation and multiple non-interacting sterile neutrinos.

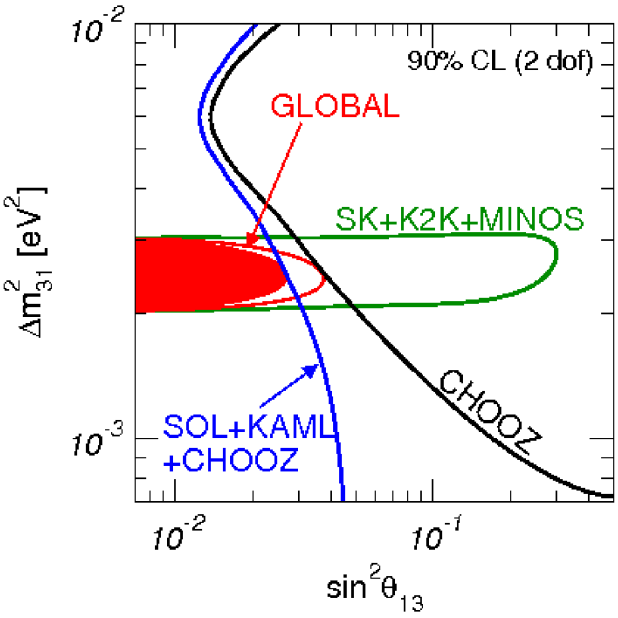

Figure 1.5: Combined analysis of the global data on θ_{13} is showed as the red allowed region. The constraints from the CHOOZ experiment as well as other contributing analyses are also shown. Plot is taken from [1].

The CHOOZ reactor experiment has placed the most stringent independent limit to date on the disappearance of $\bar{\nu}_e$ for mass splittings $\Delta m^2 > 10 \times 10^{-3}$ eV^2. It used liquid scintillator in conjunction with an inverse β-decay process to look for distortions in the $\bar{\nu}_e$ energy spectrum produced by a nuclear reactor 1 km away. The experiment ended with no observed deviation and confirmed that the atmospheric neutrino problem was not caused by $\nu_\mu \leftrightarrow \nu_e$ oscillations, instead producing a limit on $\bar{\nu}_e$ disappearance at $\sin^2 2\theta > 0.16$ for $\Delta m^2 \times 10^{-3}$[42]; see Figure 1.5.

1.4 Unresolved Issues

The collection of experiments described in the previous sections has contributed to a global understanding of neutrino oscillations governed by three massive neutrino states, $m_{\{1,2,3\}}$, and two dominant oscillation modes: solar oscillations driven

by $\Delta m^2_{\odot} \equiv m^2_2 - m^2_1$ and $\theta_{\odot}$ and atmospheric oscillations from $\Delta m^2_A \equiv m^2_3 - m^2_2$ and θ_A. The two regimes differ notably in magnitude and may be interconnected by a third mixing angle, θ_{13}, which governs, for instance, the amount of ν_e appearance in a high energy beam of ν_μ. Despite the success of oscillation experiments summarized in Table 1.1, there remain a few open questions.

Whether or not θ_{13} is non-zero is perhaps the most pressing issue in neutrino physics. A non-zero value of the parameter has yet to be measured and the CHOOZ result above is interpreted as its upper limit. While the other mixing angles have been observed to be large, θ_{13} remains constrained in large part only by the CHOOZ limit. If θ_{13} is found to be non-zero it then becomes possible to address the question of CP-violation in leptons, another long-standing issue. Should it be identically zero or extremely small this question will remain out of the reach of current and next generation experiments.

Several experiments have made searches for signs of θ_{13} including [43, 44] and several proposals for future measurements are underway. The T2K experiment will send a ν_μ beam 295 km across Japan and look for ν_e appearance in its far detector, Super-K, using an off-axis technique to measure θ_{13} [45]. The NOνA experiment will similarly be placed off-axis of the NUMI beam at Fermilab to search for ν_e apperance 810 km away from the beam source in a 30 kton tracking calorimeter [46, 47]. Finally, the Double CHOOZ reactor experiment will use two liquid scintillator detectors, one in the same experimental hall as the original CHOOZ experiment and another a few hundred meters from the neutrino source. A non-zero θ_{13} will manifest itself as a distortion of the neutrino energy spectrum seen in the far detector relative to that measured in the near detector [48].

Since oscillation experiments are sensitive to Δm^2 and not the absolute neutrino masses, it is currently not known what the mass ordering is. That is, under the "normal hierarchy" the atmospheric splitting $(m^2_3 - m^2_1)$ is at a larger absolute value than the solar splitting $(m^2_2 - m^2_1)$, $m_3 \gg m_2 > m_1$. Alternatively, the present data can be equally well described by an "inverted hierarchy", $m_2 > m_1 \gg m_3$. Matter

effects in neutrino oscillation have the possibility of determining the nature of the ordering, particularly in the event that θ_{13} is not too small.

It is the questions of the neutrino mass hierarchy and non-zero θ_{13} that provide the main motivation for this dissertation.

1.5 Dissertation Summary

The organization of this dissertation is as follows. In Chapter 2 a detailed treatment of the theory of neutrino oscillations is presented. Chapter 3 provides the physical description of the Super-Kamiokande detector and Chapter 4 outlines the simulation of neutrino interactions within it. Subsequently, the reduction and event reconstruction algorithms applied to both the data and the Monte Carlo (MC) simulation are discussed in Chapters 5 and 6. Including this introduction, these six chapters represent the core of the experiment upon which the final analyis in Chapter 8 is based. My contributions to the analysis are outlined below.

The central analysis is an extension of a search for non-zero θ_{13} using data taken during the SK-I run period and presented in Ref. [44]. In this dissertation I expanded the data set to include the SK-II run period and implemented several other changes as well. I have perfomed the fit to the SK-I again after these improvements. Further, I undertook a novel, detailed study of the possible signatures a positive value of θ_{13} would provide at Super-K that is presented in Chapter 7.

My improvements to the analysis include refinements to the binning and averaging schemes. I performed detailed studies of the sensitivity to θ_{13} for various binning schemes and the results are presented in Chapter 8. Althought not discussed here, I also studied possible improved sensitivity to the neutrino mass hierarchy in the context of the anti-neutrino induced neutron capture on Gd nuclei in the Super-K water. Tagging of neutrons by adding Gd to Super-K was proposed in Ref. [49]. Studying alternative averaging schemes, I developed an analysis method using tables of oscillation probabilities to improve the analysis run time and combine the neutrino flux weighting and averaging. However, this method is not used in this dissertation.

Table 1.1: Summary table of the global best-fit to recent neutrino oscillation data. Reproduced from Ref. [1].

Parameter	Best-Fit	2 σ C.L.
Δm^2_{21} [10^{-5} eV^2]	7.6	[7.3,8.1]
Δm^2_{31} [10^{-3} eV^2]	2.4	[2.1,2.7]
$\sin^2\theta_{12}$	0.32	[0.23,0.37]
$\sin^2\theta_{23}$	0.50	[0.38,0.63]
$\sin^2\theta_{13}$	0.007	[0.0,0.033]

Finally, since there are many similarities among the oscillation analyses at Super-K, I have rewritten the analysis software to provide a flexible, modular framework incorporating object oriented programming concepts suitable for more generic analyses. Analyses at Super-K not limited to oscillation studies are now using this software and I present further details in Appendix A.

Chapter 2

Neutrino Oscillations

Neutrino oscillations arise from the non-equivalence of neutrino mass states and the eigenstates of the weak interaction Hamiltonian. The latter describe the the neutrino state being of the same flavor as the accompanying lepton at its creation or annihilation. For instance, in the reaction,

$$\nu_\alpha + n \rightarrow l_\alpha^- + p, \tag{2.1}$$

the neutrino ν is of flavor α, since it is paired with the lepton, l_α, where α is one of e, μ or τ. Generally, these flavor states may be written as a coherent superposition of N mass states, ν_i,

$$|\nu_\alpha\rangle = \sum_i U^*_{\alpha,i} |\nu_i\rangle, \tag{2.2}$$

where U is a unitary matrix. In this context, oscillations refer to a neutrino of flavor α at birth being later observed as flavor β. This phenomenon is a result of quantum interference induced by differences in the masses of the ν_i and is discussed below.

2.1 Oscillations in Vacuum

In vacuum the neutrino mass states' time evolution is governed by a Schrödinger equation,

$$\partial_t |\nu_i\rangle = -i \sum_j H_{ij} |\nu_j\rangle. \tag{2.3}$$

The free particle Hamiltonian, having no time dependence itself, allows for an exponential solution to the differential equation,

$$|\nu_i(t)\rangle = \sum_j e^{-H_{ij}t}|\nu_j(0)\rangle, \tag{2.4}$$

where $H_{ij} = \delta_{ij}\sqrt{p^2 + m_i^2}$. For neutrinos whose momentum is much greater than the masses of any of the $|\nu_i\rangle$, these eigenvalues may be re-written using a Taylor expansion, $H_{ij} \approx (p + \frac{m_i^2}{p})\delta_{ij}$.

Neutrino oscillations appear when this evolution is recast in the flavor basis. Using Equation 2.2, the transition amplitude connecting states of flavor β and α after time t is then (neglecting an irrelevant phase factor),

$$\begin{aligned} A_{\alpha\beta}(t) &= \langle\nu_\beta|\nu_\alpha\rangle_t \\ &= e^{-ip}\sum_i U^*_{\alpha i} e^{-i\frac{m_i^2 t}{2p}} U_{\beta i}. \end{aligned} \tag{2.5}$$

The probability that a neutrino of flavor α is later found to be of flavor β is the modulus of this amplitude [50]

$$\begin{aligned} P(\nu_\alpha \to \nu_\beta) &= |A_{\alpha\beta}|^2 \\ &= \delta_{\alpha\beta} - 4\sum_{i>j} \Re\{U^*_{\alpha i}U_{\beta i}U_{\alpha j}U^*_{\beta j}\}\sin^2(\frac{\Delta m^2_{ij}L}{4E}) \\ &\quad +2\sum_{i>j} \Im\{U^*_{\alpha i}U_{\beta i}U_{\alpha j}U^*_{\beta j}\}\sin(\frac{\Delta m^2_{ij}L}{2E}), \end{aligned} \tag{2.6}$$

where $\Delta m^2_{ij} = m^2_j - m^2_i$ and $\Re$ ($\Im$) represents the real (imaginary) part of what follows it. Often the neutrino is highly relativistic and thus the propagation time and neutrino momentum can be replaced by the propagation distance L and the neutrino energy E in this equation. Note that if neutrinos were not massive, or if there were no difference between the masses, there would be no oscillations. Similarly, oscillations vanish when U is diagonal. Completely solving the neutrino problem in vacuum thus only requires specifying the mixing matrix U.

For mixing of three active neutrinos, each associated with one of the three charged leptons, the mixing matrix U is 3×3 and unitary. Unitarity imposes six conditions

which allow for three independent mixing angles, each describing the interference between one state and the remaining two, and one phase. Accordingly, the matrix can be parametrized as the product of three rotations between the states:

$$U = \begin{pmatrix} 1 & 0 & 0 \\ 0 & c_{23} & s_{23} \\ 0 & -s_{23} & c_{23} \end{pmatrix} \begin{pmatrix} c_{13} & 0 & s_{13}e^{-i\delta} \\ 0 & 1 & 0 \\ -s_{13}e^{i\delta} & 0 & c_{13} \end{pmatrix} \begin{pmatrix} c_{12} & s_{12} & 0 \\ -s_{12} & c_{12} & 0 \\ 0 & 0 & 1 \end{pmatrix}, \tag{2.7}$$

where $c_{ij} \equiv \cos(\theta_{ij})$, $s_{ij} \equiv \sin(\theta_{ij})$ and θ_{ij} is the mixing between the i^{th} and j^{th} mass states [50]. A fourth parameter, δ, describes the amount of charge-parity symmetry violation among the neutrinos. This matrix is often referred to as the MNS matrix [51].

2.2 Two-Flavor Oscillations in Vacuum

Often it is sufficient to consider a domain where two-flavor mixing with two mass states is the dominant form of oscillation. With only two mass states there is only one mass squared difference, Δm^2, in Equation 2.6 and the mixing matrix U reduces to a single rotation among them. Up to a phase factor, U can generically be expressed as

$$U = \begin{pmatrix} \cos\theta & \sin\theta \\ -\sin\theta & \cos\theta \end{pmatrix}. \tag{2.8}$$

Accordingly, Equation 2.6 reduces to a convenient closed form

$$P(\nu_\alpha \to \nu_\beta) = \begin{cases} 1 - \sin^2 2\theta \sin^2(\frac{1.27\Delta m^2 L}{E}), & \alpha = \beta \\ \sin^2 2\theta \sin^2(\frac{1.27\Delta m^2 L}{E}), & \alpha \neq \beta \end{cases} \tag{2.9}$$

where to convert from natural units to laboratory units, the change,

$$\frac{\Delta m^2 L}{E} \to \frac{1.27\Delta m^2 L}{E} \quad \left[\frac{\mathrm{eV}^2 \cdot \mathrm{km}}{\mathrm{GeV}}\right], \tag{2.10}$$

has been made to the argument of the sine functions above. It is this argument, notably the L/E dependence, that gives rise to neutrino oscillations. From Equation

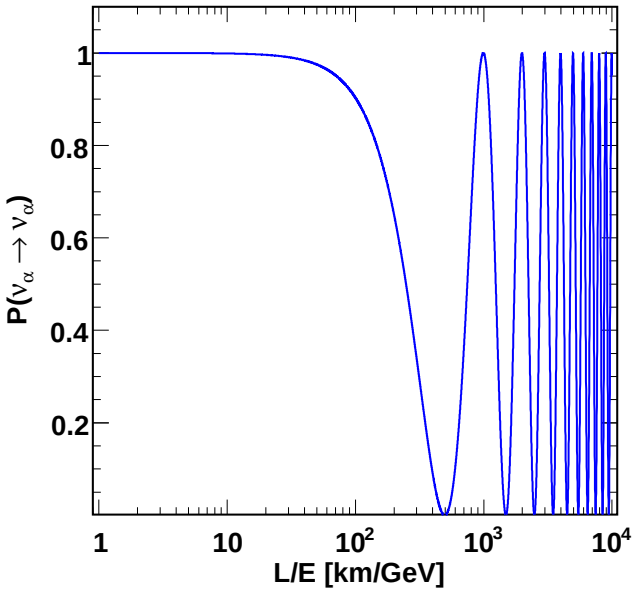

Figure 2.1: The L/E dependence of the neutrino survival probability for the two-flavor oscillation framework. The oscillation parameters are $(\Delta \mathrm{m}^2, \sin^2 2\theta) = (2.5 \times 10^{-3} \mathrm{eV}^2, 1.0)$.

2.9 the oscillation length is $L_{osc} = 4\pi E/\Delta m^2$, approximately $\approx 5,000$ km for 1 GeV neutrinos with $\Delta m^2 = 2.5 \times 10^{-3}$ eV^2. Figure 2.1 illustrates the oscillation probability as a function of L/E.

Though the oscillation probabilities for two-flavor oscillations are tidy and succinct, three-flavor oscillations in vacuum are less straightforward. The probabilities maintain the L/E oscillation characteristic and are best obtained through Equation 2.6. Matter effects in three-flavor oscillations are more relevant to the present work so further discussion is postponed until the next section.

2.3 Matter Oscillations

Neutrinos reaching terrestrial detectors do not travel solely in vacuum. In particular, many atmospheric neutrinos travel large distances through the Earth before

detection. Therefore as particles undergoing weak interactions these neutrinos are subject to scattering effects in matter. Any neutrino may scatter in the medium through the exchange of a Z-boson. Since this reaction is flavor-blind, though, it gives rise to only a common phase factor in the propagation Hamiltonian and is typically ignored in the study of active neutrinos. However, since the Earth contains a large number of electrons, electron neutrinos may additionally interact with them via the $W^{\pm}$ boson while muon and tau neutrinos do not. This asymmetry among the flavors induces an effective potential which is proportional to the density of electrons, n_e, in the surrounding matter,

$$V = \pm\sqrt{2}G_F n_e. \tag{2.11}$$

In Equation 2.11 G_F is the weak interaction coupling constant and the contribution is positive for ν_e and negative for $\bar{\nu}_e$. If the Earth were instead composed primarily of muons an analogous effective potential would arise from interactions with muon neutrinos, and not electron neutrinos. The influence of matter on neutrino oscillations was first pointed out by Wolfenstein [52] and Mikheyev and Smirnov [53] and is often referred to as the MSW effect.

Introducing this potential alters the Schrödinger Equation 2.3 considerably. Let Ψ be the vector of neutrino flavor states and x be the propagation distance,

$$\Psi(x) = \begin{pmatrix} \nu_e \\ \nu_\mu \\ \nu_\tau \end{pmatrix}(x) \tag{2.12}$$

then the evolution equation with the matter potential in Equation 2.11 may be expressed as [54]:

$$i\partial_x \Psi(x) = \frac{1}{2E}(UMU^\dagger + A)\Psi(x), \tag{2.13}$$

where $M = \text{diag}(m_1^2, m_2^2, m_3^2)$ and $A = \text{diag}(\pm\sqrt{2}G_F n_e(x), 0, 0)$. It is possible to rewrite M in terms of mass splittings, $diag(0, \Delta m_{21}^2, \Delta m_{31}^2) + m_3^2 I$, since terms proportional to the identity only contribute an overall phase to the solution and can

thus be discarded. Since the Hamiltonian is now position-dependent it is not possible to write a simple closed form for the oscillation probability as in Equation 2.6. For an arbitrary matter potential this equation may be integrated numerically, but in one which is well represented by piecewise constant slabs of matter the problem is approachable in a few ways. Equation 2.13 is then similarly piecewise constant and can be solved with a product of exponential functions in each of the slabs. By matching wavefunctions propagated across the interfaces and taking the initial value of Ψ to be a pure flavor state the final contents of Ψ can be constructed. However, since this method involves finding the eigenvalues of the matrix $U^{\dagger}MU + A$, though conceptually straightforward it is computationally intensive. A more elegant, less intensive approach incorporating similar ideas is given by Barger *et al.*[55] and is followed closely in the presentation below.

Consider the Hamiltonian in Equation 2.13 instead in the mass basis and let $\psi_i(x)$ represent a wavefunction in this basis,

$$\begin{aligned} i\partial_x \psi_i(x) &= \frac{m_i^2}{2E}\psi_i(x) + \sqrt{2}G_F n_e \sum_j U_{ie}^{\dagger} U_{je} \psi_j(x) && (2.14) \\ &\equiv H_{ji}\psi_j. && (2.15) \end{aligned}$$

Starting with the initial condition that each of the ψ_i are in a pure mass eigenstate, $\psi_i^{(j)}(0) = \delta_{ij}$, they can be arranged to form a square matrix $X_{ij} \equiv \psi_j^{(i)}$. The matrix X thus contains the evolution of each of the mass states. At time zero it is the unit matrix, and under the evolution of Equation 2.15 X_{ij} contains the amplitude for the i^{th} eigenstate to change into the j^{th}. Using the mixing matrix this amplitude can be cast into the flavor basis as

$$A(\nu_\alpha \to \nu_\beta) = \sum_{ij} U_{\alpha i} X_{ij} U_{j\beta}^{\dagger}. \tag{2.16}$$

For matter of constant density the solution of Equation 2.15 in the variable X is again exponential. Once the eigenvalues, $M_i/2E$, of the Hamiltonian H are known, X may be expressed as

$$X = \sum_k \left(\prod_{j \neq k} \frac{2EH - M_j^2 \mathbf{I}}{\Delta M_{kj}^2} \right) \exp^{-i\frac{M_k^2 L}{2E}}, \tag{2.17}$$

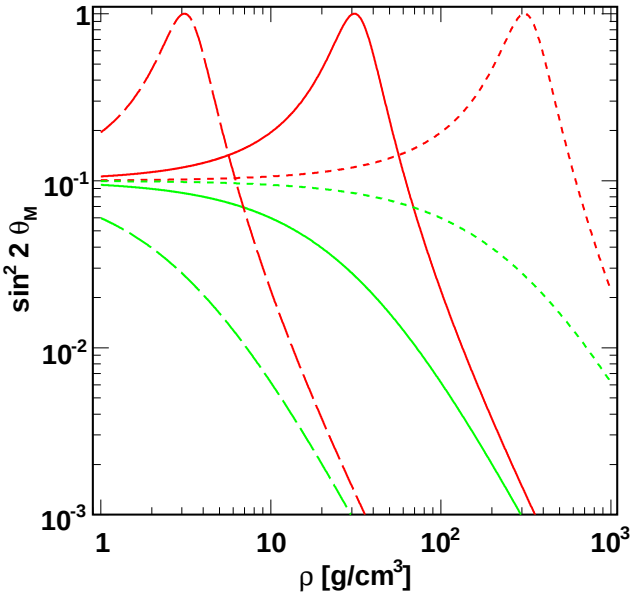

Figure 2.2: Matter mixing angle θ_M as a function of the local density for $\Delta m^2 > 0$ (red) and $\Delta m^2 < 0$ (green). The curves have been generated at $E/|\Delta m^2| = 4000$ (dashed), 400 (solid) and 40 (dotted) GeV/eV^2. Vacuum mixing has been set to $\sin^2 2\theta = 0.1$. The Earth's rock varies in density from 1 to ~ 15g/cm^3.

where $\Delta M^2_{ij} \equiv M^2_j - M^2_i$. With X in hand, oscillation probabilities are obtained through the modulus of Equation 2.16.

Traversing multiple layers of constant density is equally accessible. Solving for X in each of the layers yields a set of amplitudes whose product becomes the complete transition amplitude. For three active neutrino flavors, this approach is particularly useful since the eigenvalues of the Hamiltonian in Equation 2.15 can be found algebraically. The details may be found in Section 2.3.2. Oscillation schemes including more than three flavors can be treated well to first order but are not discussed here.

2.3.1 Two Flavor Matter Oscillations

Like two-flavor oscillations in vacuum, neutrinos traversing matter can be treated in an elegant fashion. In the two-flavor framework U is as in Equation 2.8. Here

the two flavors are labeled as those undergoing matter interactions, e, and those that do not, α. After subtracting a piece proportional to the identity matrix, $V/2$ **I**, and performing some trigonometric substitutions the evolution Equation 2.13 becomes,

$$i\partial_x \Psi(x) = \frac{\Delta m^2}{4E} \begin{pmatrix} \cos 2\theta & \sin 2\theta \\ -\sin 2\theta & \cos 2\theta \end{pmatrix} \Psi(x) + \begin{pmatrix} \frac{V}{2} & 0 \\ 0 & -\frac{V}{2} \end{pmatrix} \Psi(x). \tag{2.18}$$

Under the change of variables,

$$\Delta M^2 = \Delta m^2 \sqrt{\sin^2 2\theta + (\Gamma - \cos 2\theta)^2} \tag{2.19}$$

$$\sin^2 2\theta_M = \frac{\sin^2 2\theta}{\sin^2 2\theta + (\Gamma - \cos 2\theta)^2} \tag{2.20}$$

where $\Gamma = \pm 2\sqrt{2} G_f n_e E / \Delta m^2$, Equation 2.18 becomes,

$$i\partial_x \Psi(x) = \frac{\Delta M^2}{4E} \begin{pmatrix} \cos 2\theta_M & \sin 2\theta_M \\ -\sin 2\theta_M & \cos 2\theta_M \end{pmatrix} \Psi(x). \tag{2.21}$$

In the transformed variables the evolution equation in matter bears a striking resemblance to the two-flavor evolution in vacuum as described by Equation 2.18 with $V = 0$. Indeed, for constant density the matter evolution leads to an oscillation probability analogous to Equation 2.9 but in the "matter" variables ΔM^2 and θ_M,

$$P(\nu_e \to \nu_\alpha) = \sin^2 2\theta_M \sin^2 \left(\frac{1.27 \Delta M^2 L}{E} \right). \tag{2.22}$$

Accordingly, in low density matter, $\Gamma \ll 1$, these variables and therefore the probability in Equation 2.22 reduce to their vacuum counterparts.

Since the "matter" mixing angle now depends on the local matter density, maximal mixing occurs when the vacuum mixing angle θ is non-maximal. That is, a resonance condition can be achieved for any set of vacuum mixing parameters if

$$\cos 2\theta = \Gamma = \pm \frac{f \rho E}{6.5 \times 10^3 \Delta m^2} \quad \left[\frac{\mathrm{g/cm^3 \cdot GeV}}{\mathrm{eV^2}} \right], \tag{2.23}$$

where ρ is the matter density in $\mathrm{g/cm^3}$ and f is the proton to nucleon ratio in the matter. The sign is positive for neutrinos and negative for anti-neutrinos. Accordingly,

for positive values of $\cos 2\theta$ neutrinos are capable of experiencing this resonance when $\Delta m^2 > 0$ while anti-neutrinos do not. If $\Delta m^2 < 0$ the roles are reversed. From Equations 2.23 and 2.22 it is clear that for large values of ρ or E oscillations in matter are suppressed.

Figure 2.2 shows the matter mixing angle in Equation 2.20 as a function of density for neutrinos. The curves in red (green) show positive (negative) Δm^2 values of the parameter for neutrino mixing at small vacuum mixing. Depending on the value of $E/|\Delta m^2|$ the resonance position for $\Delta m^2 > 0$ peaks at different locations and the $\Delta m^2 < 0$ line shows no resonance. However, for densities beyond the resonance the matter mixing is suppressed as discussed above. These characteristics manifest themselves in three-flavor oscillations as well, which are discussed below.

2.3.2 Three Flavor Matter Oscillations

The three neutrino problem in matter cannot generally be solved in a transparent form. With three flavors there are now two independent mass differences and three mixing angles. Despite these additional layers of complexity the system can be solved for constant matter density once the eigenvalues of the Hamiltonian in Equation 2.15 are known. The authors of [55] have found a method to compute them algebraically:

$$M_i^2 = -\frac{2}{3}(\alpha^2 - 3\beta)^{1/2}\cos\left(\frac{1}{3}\cos^{-1}[\frac{2\alpha^3 - 9\alpha\beta + 27\gamma}{2(\alpha^2 - 3\beta)^{3/2}}]\right) + m_1^2 - \frac{\alpha}{3}, \tag{2.24}$$

where,

$$\begin{aligned} \alpha &= -2\sqrt{2}EG_F n_e + \Delta m_{12}^2 + \Delta m_{13}^2 \\ \beta &= \Delta m_{12}^2 \Delta m_{13}^2 - 2\sqrt{2}EG_F n_e[\Delta m_{12}^2(1 - |U_{e2}|^2) + \Delta m_{13}^2(1 - |U_{e3}|^2)] \\ \gamma &= -2\sqrt{2}EG_F n_e \Delta m_{12}^2 \Delta m_{13}^2 |U_{e1}|^2. \end{aligned} \tag{2.25}$$

Since only ΔM^2 appears in Equation 2.17 and not the individual eigenvalues, the dynamics of the problem are contained entirely in the vacuum mass differences Δm_{ij}^2.

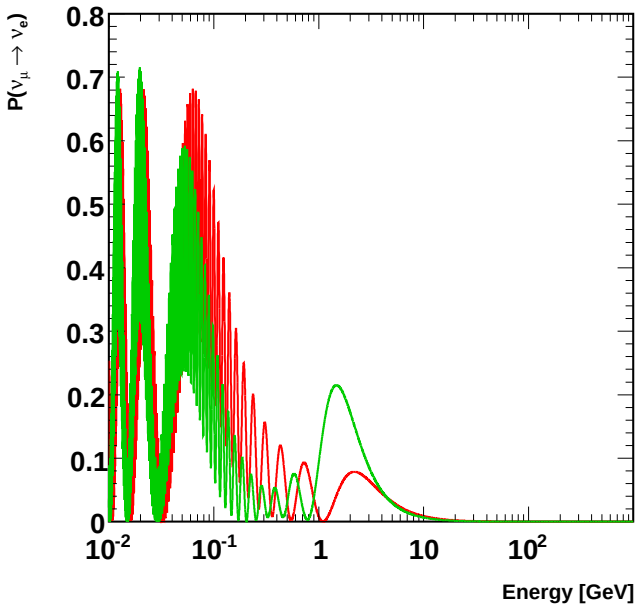

Figure 2.3: Three-flavor $\nu_\mu \rightarrow \nu_e$ oscillation probability for passage through 1000 km of vacuum (red line) and matter with density 13.0 g/cm^3 (green line) . The oscillation parameters are within the $2-\sigma$ bounds of the global best-fit data, $(\Delta m^2_{23}, \sin^2 2\theta_{23}, \Delta m^2_{21}, \sin^2 2\theta_{21}, \sin^2 2\theta_{13}) = (2.5 \times 10^{-3}\text{eV}^2, 1.0, 7.9 \times 10^{-5}\text{eV}^2, 0.825, 0.1536)$, see for instance Ref. [1].

Each of the "matter" eigenvalues is represented by one of the distinct roots of the trigonometric function in Equation 2.24.

Oscillation probabilities computed using this result are shown in Figure 2.3 for two mass differences of considerably different scales. The oscillation parameters used are consistent with the current state of experimental knowledge. Probabilities for oscillations in matter of density 13 g/cm^3 are shown in green and vacuum oscillations appear in red. The $\nu_\mu \rightarrow \nu_e$ probability has two interesting features. At low energies the dominant oscillation is controlled by the smaller of the two mass splitting. In the figure this phenomenon is illustrated by the low frequency sinusoid below 200 MeV that is convolved with another higher frequency sinusoid. Introducing matter has the consequence of slightly augmenting the oscillation probability below 30 MeV while

suppressing it noticeably around 100 MeV. Remembering the parallel effects of energy and matter density, this trend mimics the shape seen in Figure 2.2. The convolved sinusoid is the result of oscillations driven by the larger of the mass splittings and becomes the dominant mode above a few hundred MeV. For these higher frequency oscillations the matter effect appears as a resonance near 2 GeV. The height of this resonance is a function of both the matter density and the size of the parameter θ_{13}.

These general features will persist even when considering oscillations through piece-wise constant matter profiles such as that of the Earth. In this thesis the effects of the smaller, "solar", mass splitting will be neglected as an indirect result of a 100 MeV analysis threshold presented in this analysis. More details concerning oscillations using the three-flavor framework in the Earth are presented in Chapter 7.

Chapter 3

Super-Kamiokande

Super-Kamiokande (Super-K, SK) is the successor experiment to Kamiokande and is a large water Cherenkov detector. It is located 2 km within Mt Ikenoyama in western Japan at a rock overburden of 1,200 m. This overburden reduces the flux of cosmic rays reaching the detector to $\sim$ 3 Hz and corresponds to 2,700 equivalent meters of water. SK functions as a standalone experiment studying proton decay as well as various astrophysics topics and neutrino oscillations. Since 1999 the detector has been integrated into the K2K experiment [36] as the far detector, a role it will play again when the T2K experiment starts taking data [45]. Super-K has been taking data since 1996 in two phases, the SK-I period spanning 1996-2001 and the SK-II period from 2002 to 2005. The physical characteristics of both phases and primary detection methods are described here. More detailed information can be found in Ref. [56].

3.1 The SK Detector

Super-K is a right cylinder filled with 50 kt of ultra pure water. It measures 41.4 meters in height and 39.3 meters in diameter, and is optically separated into two concentric cylinders. The inner volume is referred to as the inner detector (ID) and the outer volume, which serves as both an active and passive veto, is the outer detector (OD). The OD is defined as the region extending 2.05 m inward from the walls of the SK cylinder, and 2.2 m from its top and bottom. Inward of this region is

a 55 cm dead-space spanned by a steel support structure that houses photomultiplier tubes (PMTs) viewing each of the detector regions. On the ID side of the structure PMTs are arranged in modules of 3x4 20 inch tubes spaced 70 cm from each other. To prevent light leaks into the OD the space between the PMTs is lined with a reflective black sheet. The OD side of each module includes only two 8 inch tubes, so light collection efficiency is improved by covering the outer walls of the detector and the empty region of the modules in reflective Tyvek. Tyvek's reflectivity is $\sim 90\%$ at 400 nm. Additionally, to diminish the effect of the earth's 450 mG magnetic field on photoelectrons in the PMTs, 26 Helmholtz coils line the walls of the SK tank reduce it to 50 mG.

The experimental hall has been coated with Mineguard polyurethane in order to prevent naturally occurring radon in the rock from finding its way into the detector volume. The hall itself consists of a dome atop the physical detector and separated from it by a layer of concrete. Inside the dome there are 5 huts containing the front end electronics for the experiment. The dome is connected by tunnel to a control room where the detector can be monitored continuously. Typically, the morning shift runs the experiment from the control room while the evening and midnight shifts are run offsite, remotely accessing the machines in this room. The layout of the experimental site, including a schematic of the SK tank is shown in Figure 3.1.

3.2 Cherenkov Radiation

Charged particles traveling in matter at speeds faster than the speed of light in the medium emit a cone of light in the forward direction. The light production is known as the Cherenkov effect. It can be thought of as an electromagnetic analogue to a sonic boom that occurs when $\beta > 1/n$, where n is the refractive index of the propagation material. Photons are emitted along the Cherenkov cone at an angle $\cos\theta = 1/\beta n$ as shown in Figure 3.2. For water , $n \approx 1.33$ at 580 nm, which corresponds to a critical angle $\theta_c \approx 42^\circ$. The number of photons emitted per unit track length and per unit

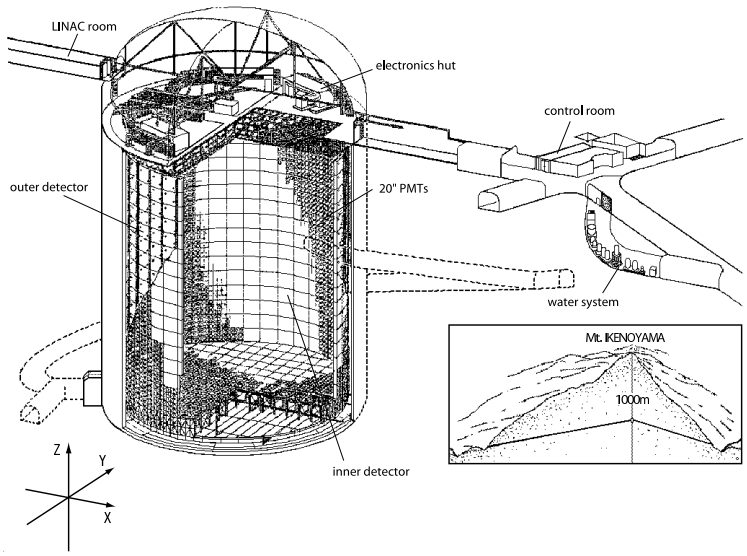

Figure 3.1: Schematic of the layout of the Super-Kamiokande detector. Taken from Ref. [57].

wavelength is given by the expression,

$$\frac{d^2N}{dxd\lambda} = \frac{2\pi\alpha}{\lambda^2}\left(1 - \frac{1}{n^2\beta^2}\right), \tag{3.1}$$

or about 3,400 photons per cm at $\lambda = 300 - 550$ nm. In this region the Super-K PMTs are the most sensitive.

Neutrinos are neutral particles that do not produce Cherenkov radiation. Instead their presence is inferred from the light emitted by the charged particles produced in their interactions. Conical light emitted from these particles paints the walls of the detector, leaving ring-shaped images across the PMTs. The timing, amount of charge in the PMTs and the shape of these rings gives information about the kinds of particles that are present in the detector. In water, the energy threshold for Cherenkov radiation is 0.76 MeV for electrons and 158.7 MeV for muons.

3.3 PMTs

The ID contains approximately 32 kt of water viewed by 11,146 (5183) inward facing Hamamatsu PMTs in SK-I (SK-II) each with a 4∼5 mm thick Pyrex window.

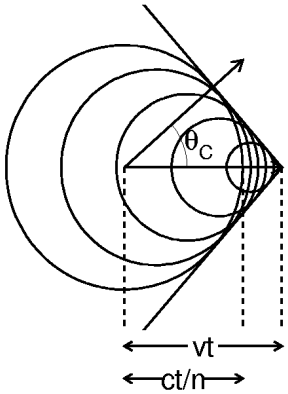

Figure 3.2: Schematic of the Cherenkov wavefront.

The PMT's photocathode is 20 inches (50 cm) in diameter yielding 40% photocoverage in SK-I and 19% in SK-II. These photocathodes are composed of a bialkali material and top an 11 stage dynode chain with a gain of 10^7 between 1.7 and 2.7 kV. The peak quantum efficiency of the PMTs rises sharply to 21% at 400 nm and drops steadily to 11% at 500nm. A diagram of a PMT is shown in Figure 3.3 and a schematic of the PMT support structure can be seen in Figure 3.5.

The OD contains 1885 20 cm Hamamatsu PMTs surrounded by 60 cm square acrylic wavelength-shifting plates to improve light collection. These plates emit blue-green light upon absorption of UV light. Though the light is delayed an additional 5 ns by the wavelength shifters there is a 60% gain in light collection. Since the OD functions primarily as a veto this gain is sufficient compensation for the loss in timing resolution.

3.4 2001 Accident

At the end of the SK-I run period in July 2001 the detector was shut down for scheduled upgrades and PMT refurbishing. By September the work had been completed and the tank filling began. On November 12 the water had been refilled to a

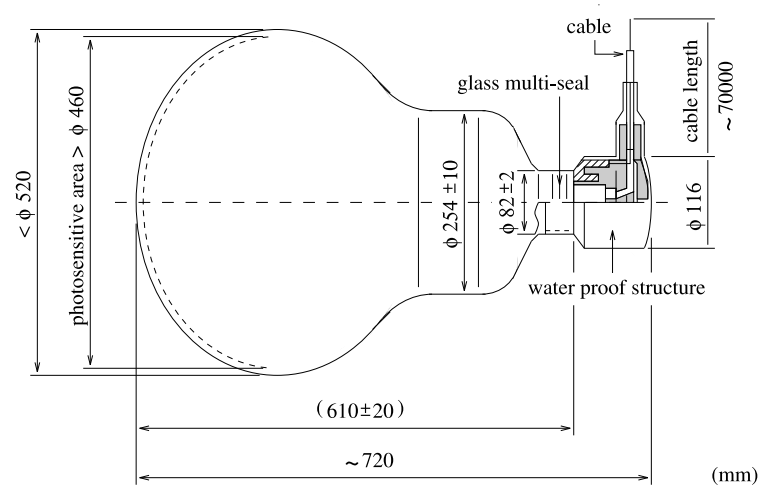

Figure 3.3: Diagram of 20 inch (50 cm) photomultiplier tube from Ref. [56].

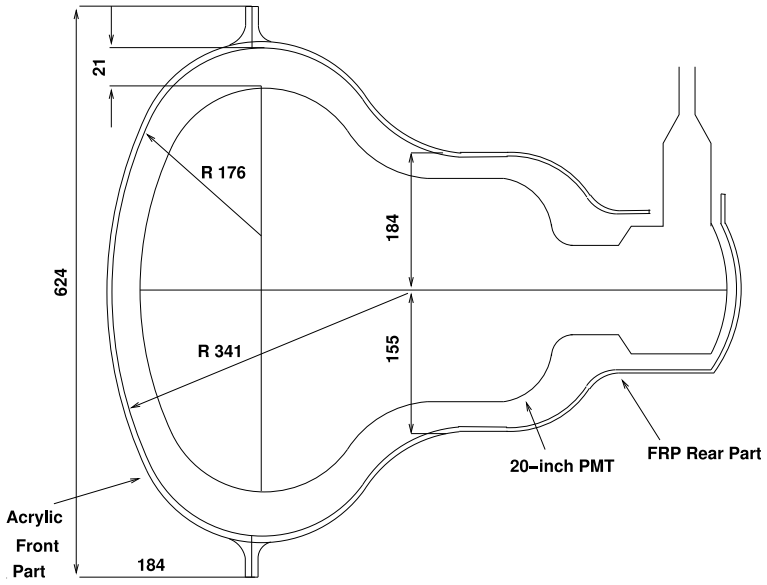

Figure 3.4: Diagram of the FRP+Acrylic PMT casing found in SK-II and SK-III. Units are in mm. Taken from Ref. [58].

height of 32 meters, and under the pressure, a PMT on the bottom of the detector imploded. The implosion created a shock wave which propagated through the water destroying 6779 ID and 885 OD PMTs. Data were being continuously taken during the water filling process, and an examination of the data up to the moments before the accident determined the its source to be among a cluster of nine tubes. Only one of these PMTs had been upgraded that summer. For the older PMTs, pressure incurred by walking atop Styrofoam pads placed over the PMTs during maintenance activities may have caused a failure. In the case of the newer tube, a crack sustained during transportation or rough handling during its installation may have resulted in its failure.

Though it is not possible to fully prevent all failures of either of these kinds, measures have since been taken to prevent a possible shock wave from destroying other PMTs. Each ID tube is encased in a fiber reinforced plastic shell (FRP) at the base and topped with an acrylic window over the photo-sensitive area (see Figure 3.4). These cases have been shown to protect against shock waves from the implosion of neighboring tubes.

Due to time constraints the detector was rebuilt with about half of the original number of ID photo tubes in a configuration known as SK-II. The OD was fully reconstructed. Super-K took data as SK-II from the start of 2003 until fall of 2005 when reconstruction was started to bring the detector back to its full complement of tubes. Reconstruction was finished in the summer of 2006 and data have since been taken as SK-III. This dissertation uses data collected in only SK-I and SK-II , so further discussion of SK-III is omitted. More information on the accident itself may be found in Ref. [59].

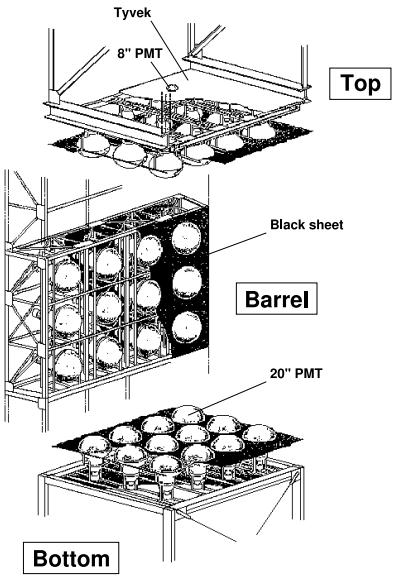

Figure 3.5: Diagram of the module structure of the PMT support frame. Figure taken from Ref. [56].

3.5 Data Acquisition System

3.5.1 ID

Each of the ID's PMTs is connected to one of 12 inputs on an Analogue Timing Module (ATM) for signal processing. The ATMs have two-channel switching at each input allowing one channel to be active while the previous one is digitized. Each is set at a threshold of 1/4 photo-electron (p.e.) equivalent. When a PMT is hit and the channel is triggered, a 15 mV 200 ns wide square wave is issued to the ATM front panel and a 900 ns veto is placed on the channel to prevent after-pulsing hits. An analog sum of all such pulses is known as the "hitsum" and forces a global trigger at 29 PMT hits. This trigger threshold corresponds to roughly 5 MeV of energy. On a trigger, event number information distributed by GONG (Go/No-Go) modules and other header information is stored along with the integrated time and charge information read from all ATM channels to Super Memory Partner boards (SMP). Data stored in the SMPs are later read out by online computers via VME

and assembled as events. There are 946 ATMs, 48 GONGs and 48 SMPs housed in the 4 electronics huts atop the SK tank. The modules themselves are organized into custom designed TRISTAN KEK Online (TK0) modules specially adapted for SK's large number of triggering channels. More details of the DAQ process can be found in Ref. [56].

3.5.2 OD

The Outer Detector phototubes are connected to a separate set of front end electronics. High voltage is distributed to the OD PMTs via "paddle cards." Each paddle card supplies 12 PMTs and is itself powered by one of 4 LeCroy 1454 mainframes. OD tubes receive high voltage and transmit analog signals across a single cable, the latter being extracted by electronics on the paddle card. The extracted signals are fed to custom built charge-to-time conversion (QTC) modules. Hit timing is recorded in the leading edge of the QTC pulse (ECL level) and the integrated charge stored in the channel is recorded in its width. This pulse is generated along with a 25 mV high 200 ns wide analog signal used to create an OD "hitsum," much like its ID counterpart, whenever a PMT exceeds a 0.25 p.e. threshold in a 200 ns wide time window. The logical pulse from the QTC is then fed to a time-to-digital converter (TDC) which is read out across all OD channels when a global trigger is issued. OD data are stored 10 μs before and 6 μs after the trigger and is read out via VME to online computers for analysis.

3.5.3 Triggering

SK triggers on various conditions corresponding roughly to separate physics analyses of interest. As the analog sum of ATM outputs, the ID hitsum signal is proportional to the number of tubes hit in a time window. This number can be subdivided to provide three trigger thresholds. The High Energy trigger corresponds to 31 hits in a 200 ns time window which corresponds to a threshold of -341 mV and fires at a rate of $\sim$ 5 Hz. The Low Energy trigger functions at 29 hits and has a rate of $\sim$ 11 Hz.

Finally, the Super Low Energy trigger has a threshold of -220 mV at 20 in-time hits. This threshold corresponds to roughly 3.5 MeV of energy and is not typically used for atmospheric analysis. These together with the OD trigger (19 hits) represent the four triggers at SK. When a trigger is issued it is sent to a hardware trigger module TRG, which signals the readout of the PMT channels.

3.6 Background Reduction

3.6.1 Water Purification

Since light reaching the PMTs must first travel through water it is important that the SK water be as pure as possible. Water is taken from the mine and passed through a 1 μm filter to remove large particles and cooled to 13° to limit the growth of bacteria. Any bacteria present in the water are killed using UV light. The water is passed through an ion exchanger and radon gas is removed using a cartridge polisher. In the final stage ultra filters are used to remove particulate matter down to 10 nm. Water circulates through the system at about $50m^3$/hr and the entire SK tank can be filled in about 40 days.

3.6.2 Radon Free Air

The air in the mine housing SK naturally contains 100-5,000 Bq/m^3 of radon throughout the year. Varied concentrations occur due to changes in the ventilation of air in the mine. In the cool season air flows from the mine entrance closest to the experiment. In the summer months, though, air flows in the opposite direction and is exposed to more rock before reaching SK and picks up more radon. To limit the amount of this background reaching the detector volume, radon free air is provided to the control room and dome areas of the experiment. The air is purified in a "radon hut" located outside of the mine via a series of compressors and activated charcoal filters and pumped in at a rate of 10 m^3/min. Radon concentrations at the dome are consistently below 100 Bq/m^3 throughout the year and typically measure about 40

Bq/m^3 when supplied with purified air.

3.7 Detector Calibration

3.7.1 Relative PMT Gain

The high voltage for each PMT is set so that all of the PMT gains are approximately the same. To measure the relative gains, an acrylic ball loaded with a wavelength shifting organic scintillator, BBOT, and a powder diffuser, MgO, is lowered into the tank. A Xe lamp generates light which is passed through a UV filter and then fed via an optical fiber into the acrylic ball. The remaining UV light is absorbed and re-emitted by the BBOT at a wavelength of 440 nm. Each PMT observes order 10 p.e. and the intensity of the UV is monitored by two photodiodes and a 2-inch PMT that also serves to trigger the detector. PMT high voltages are set by requiring that the charge accumulated in each tube after corrections for light attenuation, acceptance, and shape of the scintillator ball agree between all of the phototubes. The measurement is performed at various positions of the ball within the tank and at the beginning of SK-I the relative gains distribution had width of 7.0%. Further discrepancies in the distribution are later corrected in analysis software.

3.7.2 Absolute PMT Gain

The absolute gain of each PMT is set by measuring its single-photoelectron distribution (s.p.e), the charge response for one collected photoelectron (p.e.). Knowledge of this distribution can be used to convert the observed charge in a PMT, measured in pico-Coulombs (pC) into p.e.. The s.p.e. response is measured using 9.0 MeV gamma rays isotropically liberated from neutron capture on ^{58}Ni. The apparatus consists of a ^{252}Cf source surrounded by nickel wire shown in Figure 3.6. Neutrons produced by the spontaneous fission of ^{252}Cf (half-life 2.5 years) are emitted with energies of 2-14.2 MeV, but thermalize before being absorbed on a ^{58}Ni nucleus. SK is triggered off of an ionization counter which detects the fission products. Since the emitted photons

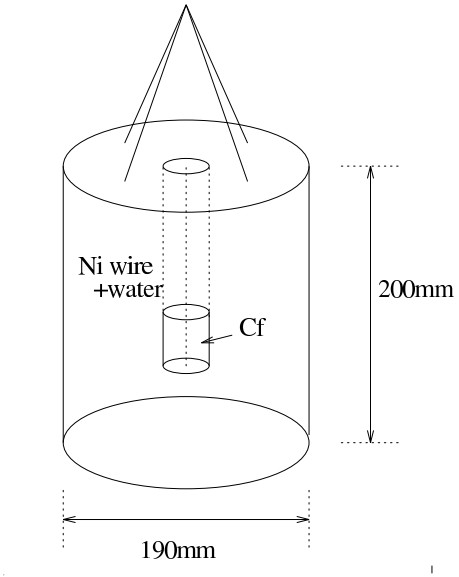

Figure 3.6: Schematic of Ni-Cf source used in absolute gain measurements. Taken from Ref. [57].

are lower in energy, PMTs typically do not register more than one photoelectron. A characteristic distribution appears in Figure 3.7. The conversion from pC to p.e. is taken using the mean of each distribution, which on average is 2.0 pC/p.e.. The large spike near zero in this distribution results from electrons which do not strike the first stage of the dynode chain.

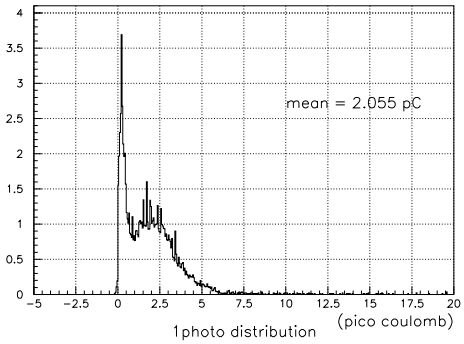

Figure 3.7: Single-photoelectron distribution of a typical ID PMT. The bump at around 2.0 pC corresponds to one p.e.. Taken from Ref. [58].

3.7.3 Relative Timing Calibration

The hit timing of PMTs varies across the detector caused by several factors. Since the SK tank is very large, timing effects arising from differing PMT cable lengths becomes important. Similarly, the timing is a function of the amount of charge collected by a PMT due to slewing in the discriminators. Each PMT's timing response is therefore measured as a function of charge and stored as a look-up table called the time-charge (TQ) map. TQ maps are created using the apparatus in Figure 3.8. Light from an N_2 laser is split into two beams, one feeding a diffuser ball placed in the SK tank and the other to a reference PMT. The laser gives 3 ns long pulses of light shifted to 384 nm and its intensity through the diffuser ball is varied with an optical filter. In this way the PMT timing at differing pulse heights can be measured. At the center of the diffuser ball is a TiO_2 tip which works in conjunction with a silica gel comprised of 20 nm shards of glass to diffuse light without smearing its time profile. A typical TQ map is shown in Figure 3.9 where the width of the distribution at a given charge represents the PMT's timing resolution. Typically the resolution is better than 3 ns at single photoelectron charge level.

3.7.4 Direct Water Transparency Measurement

As light travels through the water it is attenuated by scattering and absorption on molecules. The amount of attenuation is measured directly at Super-K using a laser/CCD camera system. A tunable titanium-sapphire laser pumped by a Nd:YAG laser provides monochromatic light in the range 350-500 nm. The light is dispersed in the tank using the diffuser ball described in Section 3.7.3 and is also coupled to a reference PMT as shown in Figure 3.10. A CCD camera at the top of the tank measures the light intensity at the diffuser ball. By repeating the measurement at several positions within the tank, a fit is made to

$$\frac{I_{ccd}}{I_{PMT^{ref}}} = I_0 \exp\left(\frac{-l}{L(\lambda)}\right) \tag{3.2}$$

to extract the attenuation length, L, at a wavelength λ. Here l is the distance to the

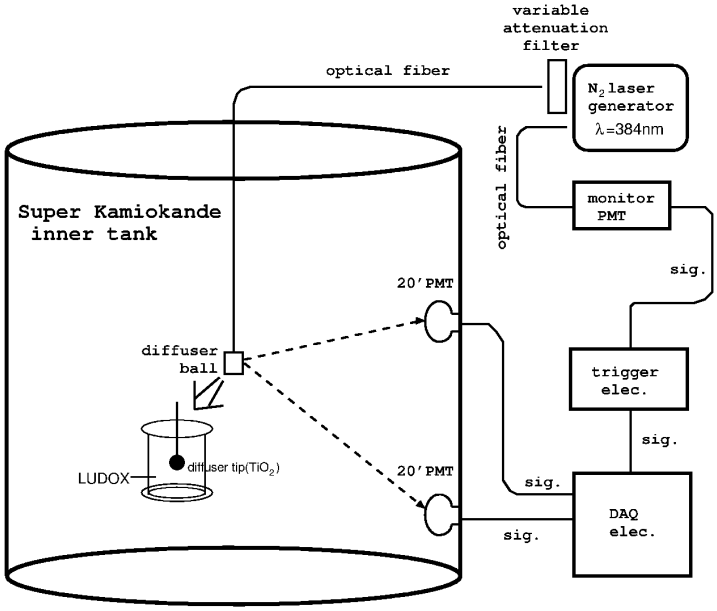

Figure 3.8: Schematic of the laser calibration system used to make TQ maps for the relative timing calibration of the PMTs. The figure is taken from Ref. [57].

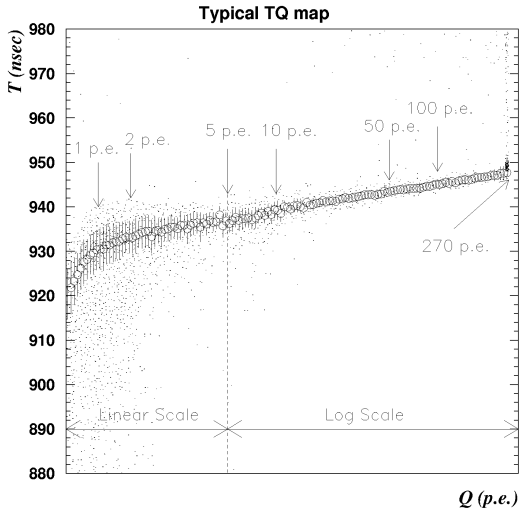

Figure 3.9: A characteristic TQ map for an ID PMT. Taken from Ref. [56].

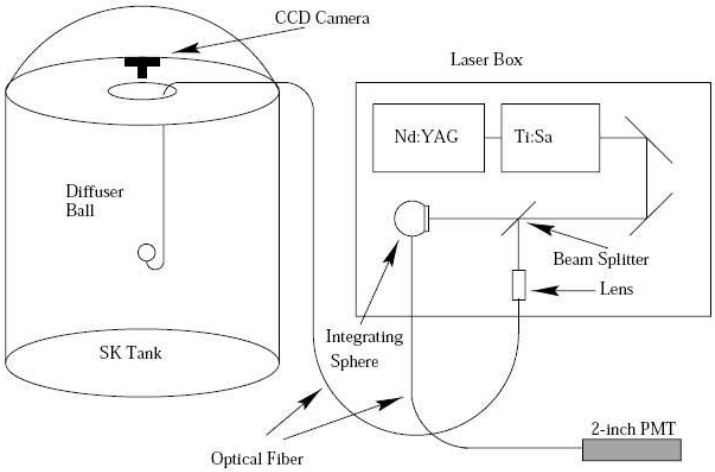

Figure 3.10: Experimental apparatus for measuring water transparency with a titanium-sapphire laser. Taken from Ref. [56].

diffuser ball. The measurement is performed at several wavelengths and at 420 nm the attenuation length is found to be 97.9 ± 3.5 m as can be seen in Figure 3.11.

3.7.5 Indirect Water Transparency Measurement

The water transparency can also be measured using natural sources, namely muons traversing the detector. Muons continuously pass through SK allowing for a continuous measurement of the water transparency. Since they emit a constant number of photons per unit track length through ionization, they serve as an effectively constant source of light. The charge observed by a PMT at a distance l from a muon track can therefore be expressed as,

$$Q = Q_0 \frac{f(\theta)}{l} \exp\left(\frac{-l}{L}\right), \tag{3.3}$$

where Q_0 is a constant and $f(\theta)$ is a factor describing the PMT acceptance. Plotting the quantity $Ql/f(\theta)$ as a function of the path length and fitting to the above exponential yields the absorption length. One measurement is shown in Figure 3.12 and gives an absorption length of 105.4 ± 0.5 m.

The separate scattering and absorption components of the water transparency are

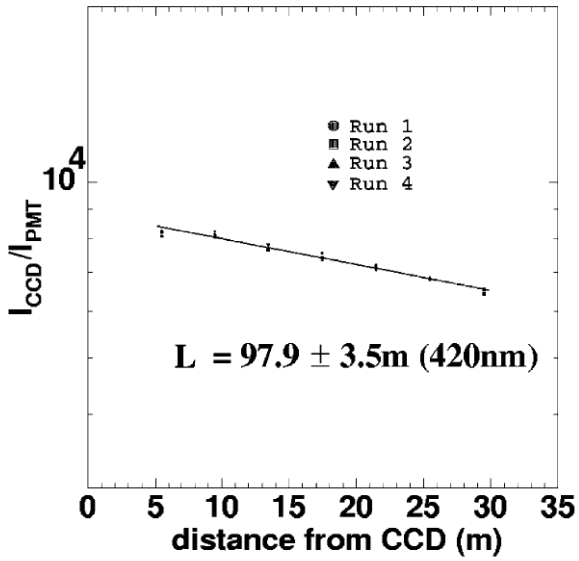

Figure 3.11: Fitted result of direct water transparency measurements at 420 nm from Ref. [56].

also measured at Super-K and details of the method can be found in Ref. [56].

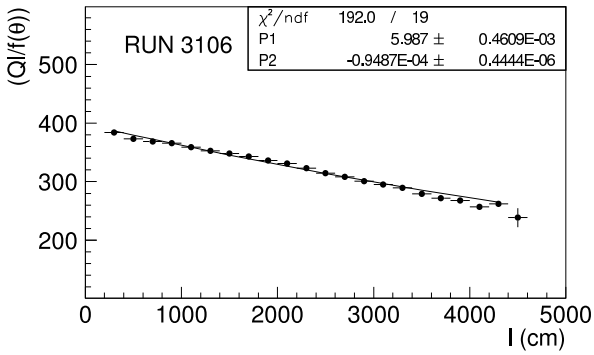

Figure 3.12: Result of water transparency measurement using cosmic-ray muons from Ref. [56].

Chapter 4

Super-Kamiokande Monte Carlo

Super-Kamiokande's measurements rely critically on the expected event distributions in the detector. This expectation is not a simple function or formula and is therefore simulated using the Monte Carlo (MC) method to predict neutrino interaction rates in the detector. Measurements are made by comparing the observed data with this prediction, so it is important that the simulation be as robust as possible. The Monte Carlo simulation at Super-K is done in stages modeling the initial neutrino interactions in the water, subsequent particle tracking inside of the detector volume and the detector's response to those particles. Each of these stages is discussed below.

4.1 Atmospheric Neutrino Flux

Atmospheric neutrino interactions at Super-K are modeled using the Honda [60] flux calculations. Two other flux calculations, the Fluka flux [61] and Bartol flux [62], are also used to compute flux-related systematic errors and as cross-checks for other parts of the analysis. Each of these computations employs a 3-dimensional scheme for tracking the passage of cosmic rays through the atmosphere. Secondary particles are allowed to take trajectories different from their parent particles, unlike previous generations of calculations (c.f. Refs [63, 64]).

The Honda flux takes into consideration several environmental factors in addition to using 3-dimensional tracking. The primary flux is composed almost entirely of H

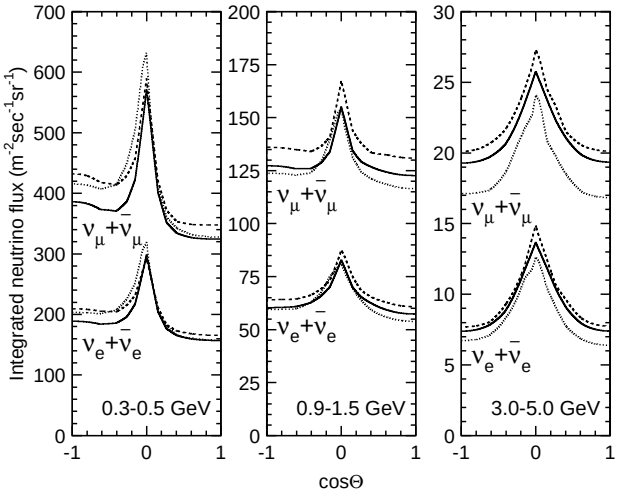

Figure 4.1: Flux of atmospheric neutrinos as predicted by [60] (solid), [62] (dashed) and [61] (dotted) as function of zenith angle for several energies.

nuclei and is influenced by the solar wind. During periods of high solar activity (solar maximum) the flux of low energy (~ 1 GeV) cosmic rays is lower by nearly a factor of two relative to periods of lower activity because of the solar wind's stronger magnetic field. Similarly these low energy primary particles are influenced by the Earth's magnetic field, which gives a rigidity cutoff. Particles lacking sufficient momentum to penetrate the Earth's field are deflected and do not contribute to the neutrino flux. Further, the strength of the magnetic field is at Kamioka is slightly larger than the global average, resulting in a slightly up-down asymmetric neutrino flux. The influence of these phenomena is negligible for higher energy cosmic rays (> 10 GeV), and the effects of both on the neutrino flux are included in the flux calculation.

Figure 4.1 shows the zenith angle distribution of the neutrino flux in the Honda model, which peaks sharply near the horizon. Primary cosmic rays coming near the horizon spend more time traversing the upper atmosphere giving them more time to decay. This effect is more pronounced at lower energies because of deflection of secondaries by the geomagnetic field. The flux at the horizon is enhanced in the Honda calculation, relative to its 1-dimensional predecessors, since the effective area from which a horizontal neutrino can originate is larger when the neutrino is not confined to the direction of its parent. Though not shown in the figure, this effect

gives a lower production height (altitude) for these neutrinos and will play a role in the analysis section. The energy dependence of the neutrino flux and the ratio of flux predictions for different models is shown in Figure 4.2.

4.2 Interaction Monte Carlo

Neutrino interactions within the detector and in the surrounding rock are simulated using the NEUT [65] model. A second model, NUANCE [66], has also been used for various cross-checks but is not discussed here. Within NEUT the interaction of neutrinos is considered on protons, oxygen, and sodium through the following modes,

$$\begin{aligned} \text{CC/NC elastic scattering} \quad & \nu + N \rightarrow \quad l + N' \\ \text{CC/NC meson production} \quad & \nu + N \rightarrow \quad l + N' + m \\ \text{CC/NC coherent pion production} \quad & \nu + {}^{16}\text{O} \rightarrow \quad l + {}^{16}\text{O} + \pi \\ \text{deep inelastic scatting} \quad & \nu + N \rightarrow \quad l + N' + X \end{aligned} \tag{4.1}$$

where l is a lepton, N, N' are nucleons, m is a meson, and X is a hadron. The neutrino cross section for interaction on electrons is a factor of 10^3 times smaller than that on nucleons and is therefore ignored in these simulations. A more detailed account of these interactions is given in Ref. [57].

4.2.1 Elastic Scattering

Elastic scattering in NEUT is implemented through two models. Scattering on free protons is based on the Llewellyn-Smith[67] model and scattering on bound nucleons in ^{16}O nuclei is computed using that of Smith and Moniz [68]. In the latter, the nucleons are approximated as a relativistic Fermi gas where individual nucleon momenta are drawn from a flat distribution up to 225 MeV/c Fermi surface. Pauli-blocking is

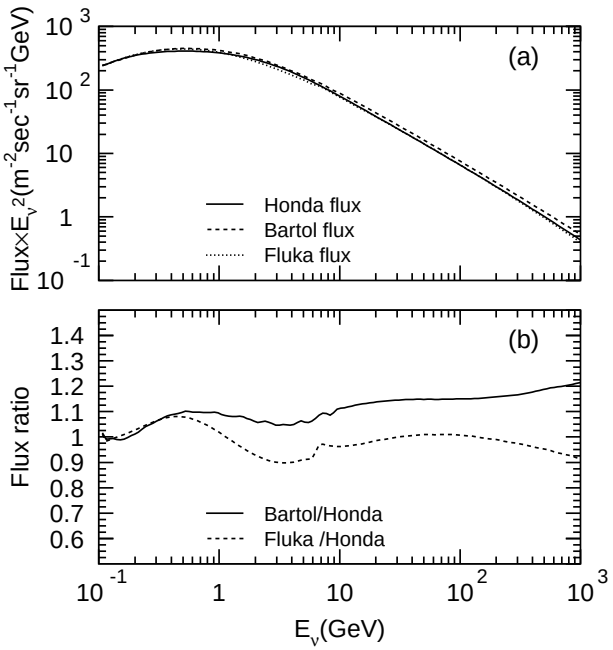

Figure 4.2: Direction averaged flux of $\nu_\mu + \bar{\nu}_\mu$ as predicted by different calculations as a function of energy appears in the top panel. The ratio of the predictions relative to [60] are shown in the bottom panel. Taken from [33].

considered by requiring the recoiling nucleon's momentum be greater than the Fermi-surface momentum. Neutral current interactions are derived from the charged current cross sections. The axial vector mass, M_A, a parameter in the quasi-elastic form factor, has recently been measured as 1.2 GeV at the K2K near detector [69]. However, the simulation used the previous value of 1.1 GeV.

4.2.2 Single Meson Production

Single π, K, and η production is simulated using the Rein and Sehgal model [70, 71] with an intermediate baryon resonance. The excited resonance is restricted to have mass < 2 GeV/c^2 and allowed to decay into a meson and a nucleon. Decay modes producing K and η are important in the prediction of proton decay backgrounds. Pions make up the majority of the produced mesons and their angular distribution is computed from the decay of the $\Delta(1232)$. Pions produced through other resonance decays are assumed to be isotropically distributed. The distribution of π^+ for $\nu_\mu + p \rightarrow$

$\mu^- + p + \pi^+$ has been measured in [72] and is in agreement with these simulations. Roughly 20% of Δ decays, though, will have no pion in the final state [73], an effect that is also simulated.

Instead of interacting with an individual nucleon the neutrino may scatter off the entire ^{16}O nucleus. Since the nucleus is much heavier than the neutrino it is only slightly perturbed and the resulting pion exits with an angular distribution peaked in the forward direction. This coherent production is simulated using the model in Ref. [74].

4.2.3 Deep Inelastic Scattering

The GRV94 [75] parton distribution functions are used to simulate deep inelastic scattering. Hadronic masses greater that 1.3 GeV/c^2 are considered. Since single pion production is handled separately, only multiple pion production is considered in the overlap region between the modes. At masses up to 2.0 GeV/c^2 hadronic final states are computed by [76] and above this threshold PYTHIA/JETSET[77] is used.

The total scattering cross section broken down into the individual components discussed above is shown as a function of neutrino energy in Figure 4.3.

4.2.4 Nuclear Effects

Hadrons generated inside of ^{16}O undergo interactions with the surrounding nucleons before exiting. Since pion production is large around 1 GeV and the interaction cross section for pions with nucleons is also large at these energies their effect is important. In the SK simulation pions are allowed to undergo charge exchange, absorption, and inelastic scattering while inside the nucleus. The position of pions within the nucleus is generated using the Woods-Saxon nucleon density distribution[78]. The mean free path of the pion is calculated using Ref. [79] and used to determine which of the nuclear interactions the pion undergoes. Pauli-blocking is considered in the same manner as above. These simulations were verified using pion scattering on ^{12}C, ^{16}O and pion photo production on carbon from data found in Ref. [80].

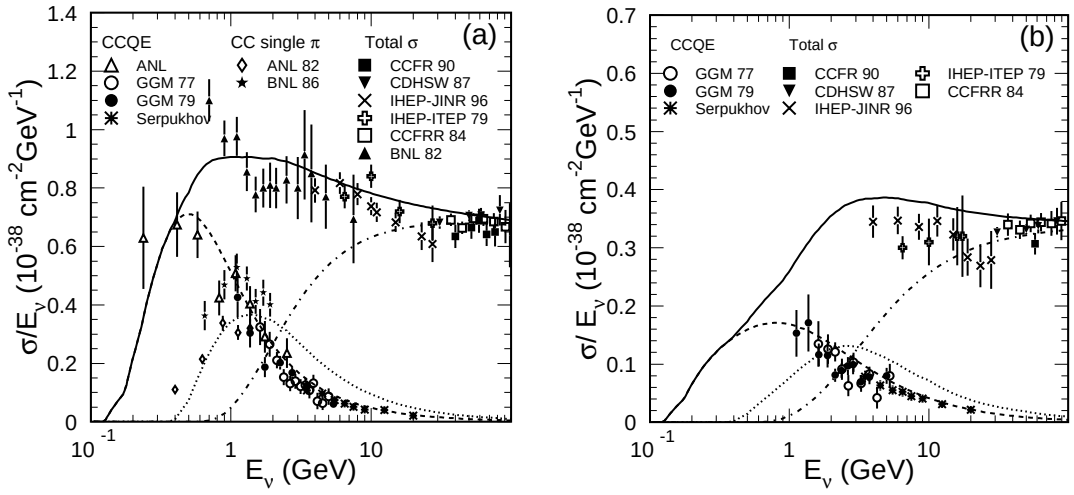

Figure 4.3: Total neutrino(a) and anti-neutrino(b) cross sections as a function of energy. The calculated quasi-elastic scattering cross section is shown in the dashed line, that of single meson production appears in the dotted line, and the dash-dotted line shows deep inelastic scattering. Overlaid are data from several experiments. Taken from [33].

4.3 Detector Simulation

After the simulation of the initial neutrino interaction outgoing particles are input into a detector simulation responsible for tracking. During the tracking particles undergo physics processes which may create secondary particles which are subsequently followed through the detector. The purpose of the simulation is to provide an accurate model of the Super-K tank itself as well as its electronic response to particles in the detector volume.

The simulation is implemented using CERN's GEANT[81] package modified to the detector geometry. Within GEANT particle decays and the production of Cherenkov light are simulated on request, though their interactions with SK specific materials, such as Tyvek, are handled by subroutines in the program framework. As Cherenkov photons travel through water they are subject to scattering effects. Rayleigh and Mie scattering effects in the water are simulated and tuned to match calibration data. At very long wavelengths absorption effects dominate and are similarly tuned. Light re-

flection off the black sheet and Tyvek surfaces of the detector is modeled and optimized separately. For the OD Tyvek in SK-I, isotropic reflection in both the azimuthal and polar angle was used, and then later upgraded to a combination of isotropic, Gaussian and Lambertian reflection for SK-II. The latter is more representative of the true Tyvek reflectivity and is correlated with the photon's incident angle. More details are presented below.

Hadronic processes with momenta above 500 MeV/c are simulated using the CALOR[82] package. Down to $\sim$ 1 GeV/c this package reproduces the interaction of pions well, but for lower pion momenta a separate custom program based on the data in [83] and [84] is used.

Additionally NEUT is used to simulate the production of upward-going muons in SK from the interactions of neutrinos in the rock surrounding the detector. The rock is assumed to be "standard" SiO_2, with an average density of 2.65 g/cm^3. Before reaching the detector volume most particles emerging from such interactions will stop inside the rock, and therefore only energetic muons are input to the detector simulation. These neutrino interactions are restricted to have an invariant mass greater than 1.4 GeV/c^2, and are also allowed to originate in the OD volume.

The detector electronics are simulated at the PMT signal level. The measured quantum efficiency and single photoelectron distributions of SK PMTs are used as inputs to simulate the amount of charge collected in a simulated PMT. Dark noise and saturation effects are included, and further in the analysis chain, physical PMTs which have been disconnected or failed during the experiment are masked-out of the simulation. The simulation's electronic response, when compared with the true detector response to data events helps determine the absolute energy scale of the detector.

4.3.1 Tuning the OD Monte Carlo

Recently the Super-K MC has undergone a series of upgrades. After these improvements, the OD portion of the simulation has been optimized under a new Tyvek

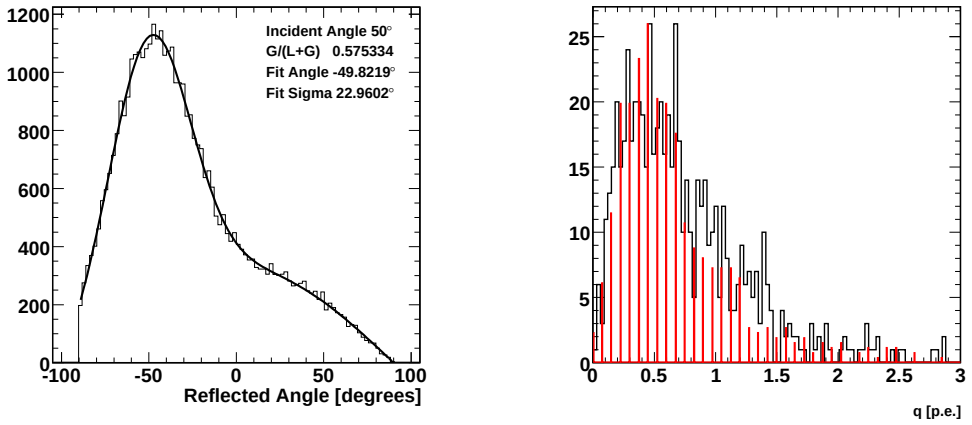

Figure 4.4: The angle of reflection distribution for simulated photons at an incident angle of 50° on the OD Tyvek overlaid with a Gaussian and Lambertian fit is shown in the left panel. At right, a comparison of the SK-I simulated (red) and measured (data) single photoelectron charge distribution for OD PMTs. The measured response is taken from hits preceding the main trigger window.

reflectivity model. The optimization (tuning) procedure is outlined in this section to provide a reference suitable for future modifications to the simulation. However, none of the MC generated under the new model is used in this dissertation.

The new OD MC is optimized using two cosmic ray muon samples and 14 tuning parameters that control the Tyvek optical model and the simulated PMT response. The top, bottom and barrel portions of the OD are independently tuned. However, since the number of parameters is large it is not efficient to tune them by a χ^2 method. Instead, a physicist is responsible for comparing the data and MC distributions of several event variables and adjusting the tuning parameters until they agree.

Cosmic ray muons provide a good tuning sample since they pass through the OD, are abundant and are usually well fit by the detector reconstruction algorithms. To tune the MC, a sample of through-going muons that enter the detector in the top region and exit out the bottom, as well as muons which enter the detector through the barrel region and stop in the ID are selected from the data. Reconstructing each muon's path length and energy, a muon with the same parameters is simulated with

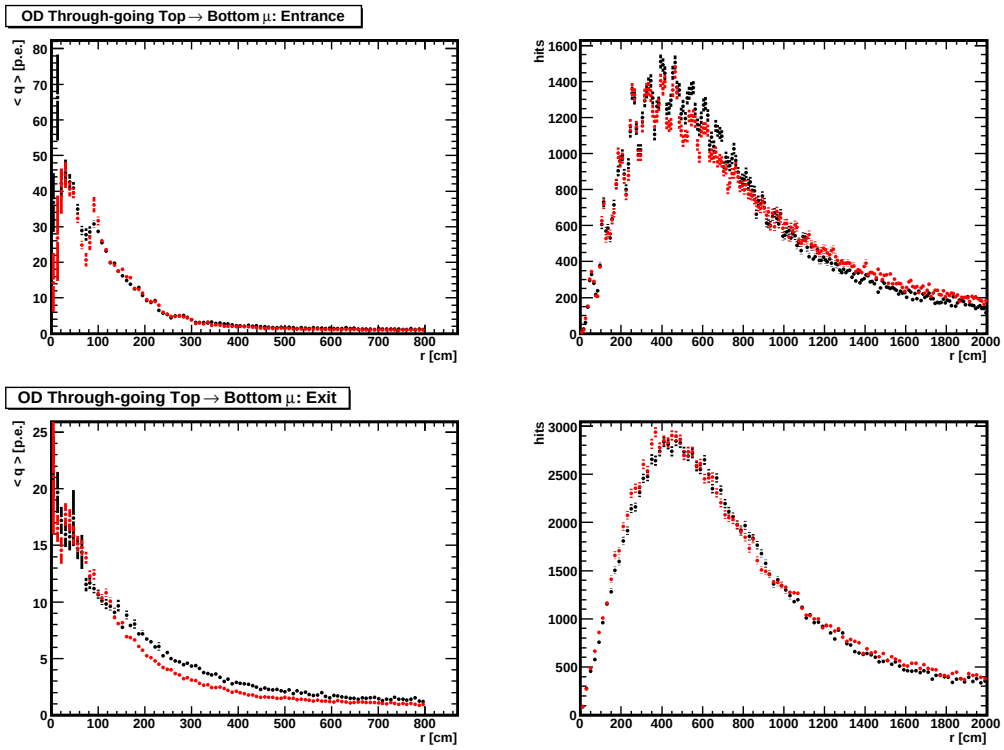

Figure 4.5: Average charge as a function of distance from the particle's fitted entrance (top left) and exit (bottom left) for the through-going muon sample entering the top and bottom regions of the detector. Saturation effects in the PMTs become visible at distances < 200 cm. The distributions of PMT hits as a function of distance from the entrance (top right) and exit (bottom right) points are also shown.

the MC. The simulated OD response is then compared with the observed response and the tuning variables are changed. With each adjustment of the tuning parameters the MC muons must be re-simulated and compared against the data.

Recently the SK-I MC has been tuned to incorporate a Tyvek reflectivity model based on the measurements in Ref. [85]. The measurement determined the fraction of Gaussian and Lambertian character in the reflection of light at various incident angles. Using the measured fractions a model has been constructed in the MC. The model is shown in the left panel of Figure 4.4 for photons incident at 50°. A peak at the angle of specular reflection is clearly seen and a fit to the distribution returns the proper ratio of components indicating the model is consistent with Ref. [85].

The tuning process is done in three steps: tuning the single photoelectron response,

tuning the PMT saturation and tuning the Tyvek reflection properties. The single photoelectron response is measured in the muon data by considering hits occurring prior to the main event window. In the data these dark noise hits usually represent one photoelectron, an effect which is also accounted for in the MC. For SK-I the OD tubes are well described by the combination of a plateau response at low charge and an exponential response at higher charges. The number of photoelectrons for a given PMT hit in the simulation is drawn randomly from this combined distribution. During the tuning process, parameters controlling the relative amount of plateau and exponential character in the distribution are adjusted. A discriminator threshold is simulated by discarding hits for which a generated uniform random number is below a tunable threshold. The results of adjusting these parameters on the PMT single photoelectron distribution are shown in the right panel of Figure 4.4.

Tuning the PMT saturation and collection efficiency is done using two distributions. Saturation effects become relevant in PMTs close to the exit or entry of an energetic particle in the tank. PMT saturation is modeled using the relation

$$Q = \frac{s_0 q_0}{1 + s_1 q_0}, \tag{4.2}$$

where Q is the saturation adjusted charge, q_0 is the charge drawn from the single photoelectron distribution above and $s_{0,1}$ are tuning parameters. Plotting the average charge as a function of distance from these points then provides a useful tuning distribution. The left panels of Figure 4.5 show this distribution for the fitted entrance and exit points of the through-going muon sample. In these plots saturation effects are most visible at distances less than ~ 200 cm. The data appear in black, the MC in red, and the entrance on the top shows good agreement between the two. Near the exit on the bottom the agreement is also good but the data and MC differ farther out. The right panel shows the distribution of hits as a function of distance from the entrance and exit points. This distribution is useful for tuning the efficiency for a PMT registering a hit in the simulation. Both the exit and entrance points show good agreement between data and MC. Note that the PMT efficiencies are independent among the top, bottom and barrel regions of the OD.

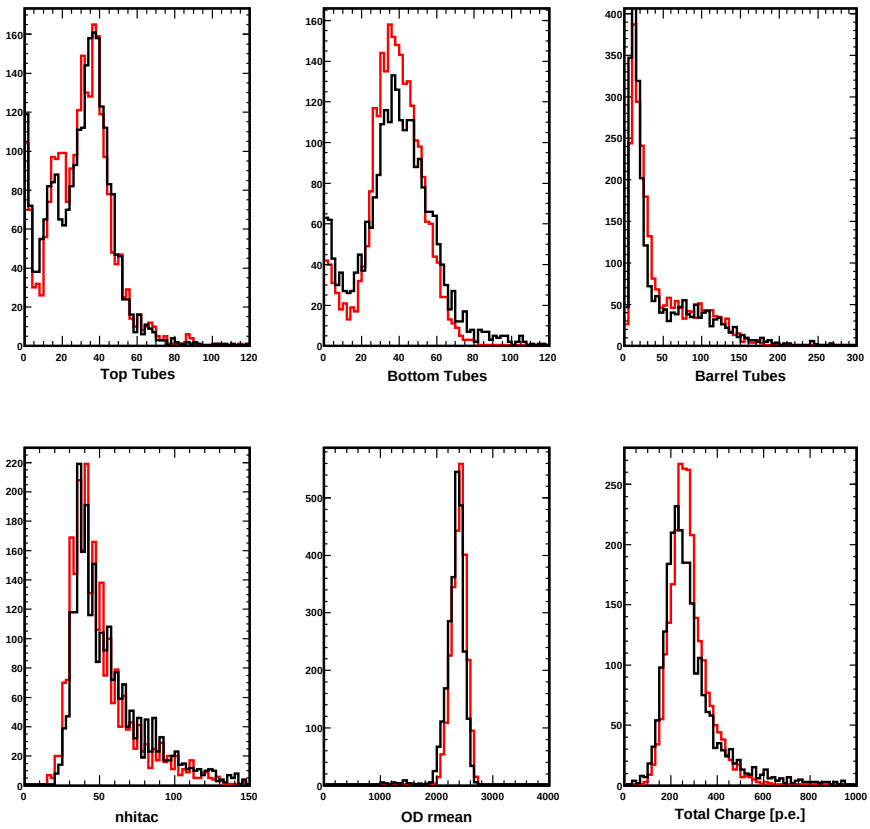

Figure 4.6: Tuning distributions for the SK-I MC (red) in comparison with the data (black). The variables are described in the text.

Up to this point the tuning parameters have been adjusted to provide agreement with the data at a very basic level. The next phase of the tuning is arguably more vital since tuning remaining pieces of the optical model is done using variables that appear in several aspects of the reduction process. Figure 4.6 shows the tuning variables for the through-going top to bottom muon sample. In the top row, the number of hit PMTs in the top, barrel and bottom portions of the detector are shown. Adjusting the probability of reflection on the Tyvek in each of these sections shifts the MC distribution. Larger reflection probabilities generally move the distribution towards a higher number of hit tubes. These distributions agree well in the figure, and though these plots are for through-going muons essentially traversing the detector vertically through its top, the distribution of barrel PMTs is also in agreement.

In the bottom row of the figure, from left to right, are the "nhitac", "OD rmean" and total charge distributions. Nhitac is a variable which records the number of hit PMTs in the cluster of OD PMTs that has the highest amount of charge among all clusters. This parameter is used in the PC reduction, (see Section **??**) and in terms of tuning parameters is related closely to the PMT collection efficiency and the Tyvek reflection probability. That is, if the charge distributions and reflection probabilities have been tuned in the previous steps the nhitac distribution agrees to a reasonable extent. Small discrepancies can be tuned with changes in the PMT collection efficiencies. The OD rmean parameter is the average distance taken among all pairs of hits and larger values indicate events that are more diffuse in the detector. Tuning this distribution is similar to tuning nhitac. Total charge is the sum of all charge accumulated in the OD and is tuned primarily by the PMT collection efficiencies provided the single photon distributions are in agreement. The distributions in Figure 4.6 are in good agreement.

Chapter 5

Atmospheric Neutrino Event Reduction

5.1 Fully Contained Reduction

Atmospheric neutrino events at Super-Kamiokande are classified into four main categories based upon their topology. Neutrino interactions that originate within the ID with no particles exiting into the OD are classified as "fully contained" (FC). Events that originate inside the ID but have one or more particles depositing visible light in the OD are classified as "partially contained"(PC). Muons produced by the interaction of neutrinos in the rock below the detector are subdivided into two categories. Upward-going muons (upmu) which originate in the OD but lose energy and stop in the ID are labeled "upward stopping muons", while those that continue on to traverse the detector volume are "upward through-going muon" events. Figure 5.1 is a schematic of each of the event types.

At SK roughly 10 atmospheric neutrino events per day are expected amidst a background of more than a million events. Each of the event categories above goes through a series of reduction steps to select candidate events from this background. Generally the initial steps of the reduction are not computationally intense and are designed to remove apparent backgrounds quickly and efficiently, while later steps focus on finer subtleties between events. The steps of the atmospheric reduction are

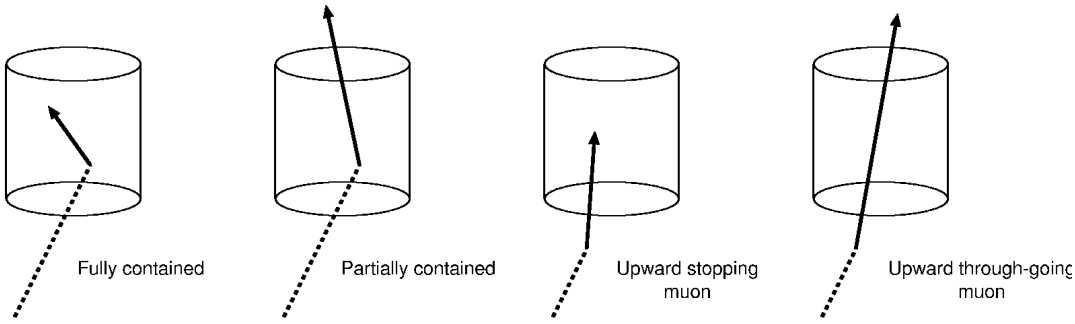

Figure 5.1: Schematic of fully contained, partially contained and upward-going muon event categories at Super-K.

described below.

5.2 Fully Contained Reduction

Fully contained events are distinguished from other types of events based on the lack of activity in the outer detector. Serving as an active veto, the OD removes entering cosmic rays from the data. The atmospheric neutrino analysis considers only events with visible energy E_{vis} greater than 30 MeV, where visible energy is defined as the energy of a showering electron that produces the same amount of observed Cherenkov light. A 300 MeV/c muon, for instance, gives a visible energy of $\sim$ 110 MeV. Where the reduction differs between SK-I and SK-II the latter has been written in parenthesis. The differences arise from the difference is photocathode coverage during the two run periods: 40% in SK-I and 19% in SK-II.

5.2.1 First and Second Reduction

These reduction steps are designed to remove the most consistent and numerous backgrounds including those from cosmic ray muons and low energy radioactive backgrounds. The latter are removed by requiring the total charge in the inner detector collected within a 300 ns wide time window be greater than 200 (100) p.e.'s; roughly the charge of a 22 MeV/c electron. This cut is strengthened by requiring that the

ratio of p.e.'s collected in any single ID PMT be less than half of the the total in the ID in a 300 ns window. Cosmic ray muons are in large part eliminated by requiring that less than 25 PMTs in the OD are hit within ± 400 ns of the initial trigger and $< 1 \times 10^6 (5 \times 10^5)$ p.e. in the ID. Finally, decay electrons coming from muons traversing the detector below the Cherenkov threshold are rejected by demanding that events precede each other by not less that 100 μs.

5.2.2 Third FC Reduction

Beyond the first two reduction steps the process begins to focus on muon events with little activity in the OD and electronic noise. Events are rejected if they are fit as a through-going muon with a goodness-of-fit > 0.75. Assuming the event's ID light pattern came from such a muon, events are cut if there are more than 10 hit OD PMTs within 8 m of the supposed muon's entrance and exit points on the ID. Candidate events are also fit under a stopping muon assumption and are rejected if the fit's goodness is > 0.5 and there are ≥ 5 OD PMTs hit within 8 m of the ID entrance point in 800 ns. Events passing this condition may still be rejected if there are ≥ 10 hit tubes in this window, regardless of the fit's goodness.

Muons which travel through one of the four large cable bundles supplying the detector PMTs leave little light in the OD and are therefore monitored by 2x2.5 m plastic scintillation counters placed atop the bundles. Events fail this stage of the reduction if there is a hit in one of these veto counters or if the reconstructed vertex of the event is within four meters of the cable hole.

Accidental coincidence events occur when a low energy event accompanies a cosmic ray muon in the same trigger. This class of background is eliminated by requiring ≤ 20 OD hits and ≤ 5000 (2500) p.e.'s in the ID within a 500 ns wide time window 400 ns after the main trigger. Separate low energy events are further reduced by removing any event with $\geq 50(25)$ hit ID PMTs in a sliding 50 ns time window if all of the event's light is assumed to originate at a single vertex. Finally, events originating from "flasher" PMTs (see Section 5.2.3) are cut when $\geq 15(20)$ ID PMTs fire within

a sliding 100 ns window 300 ns and up to 800 ns after the main event trigger. For SK-I only, if fewer than 800 ID tubes are hit in total, this criteria is reduced to ≥ 10 PMTs.

5.2.3 Fourth FC Reduction

The fourth step of the reduction is dedicated to removing events caused by the repetitive electrical discharge of PMTs, known as "flashers". These events therefore have characteristic patterns which occur successively and can be used to create a correlation parameter between the candidate event and other data events. Often these patterns include a cluster of rapidly firing PMTs. Accordingly, the correlation parameter is constructed using the charge accumulated in 1450 patches of $6 \sim 9$ PMTs in the detector. The correlation is computed between the candidate event and 10,000 events before and after. Highly correlated events are removed.

5.2.4 Fifth FC Reduction

In the fifth reduction step, remaining muon backgrounds are targeted for removal. Muons with momenta below the Cherenkov threshold may decay and produce an electron above threshold creating a spurious event. These invisible muon events are rejected if there are ≥ 10 OD hits in any 200 ns wide time window between 800 and 100 ns preceding the event trigger. Another stopping muon cut like that of the third reduction is performed, but using a more precise fitter to find the entrance point. Remaining coincident muon events are identified and cut when there are $< 300(150)$ p.e. in the ID accumulated between -100 ns and +400 ns around the main trigger accompanied by ≥ 20 OD PMTs firing in a sliding 200 ns window in the 800 ns starting at +400 ns. An additional cut to remove flashers is performed only for SK-II.

Table 5.1: FC event rate after each stage of the reduction. "Final" refers to the fidicial volume and visible energy cuts.

Reduction Step	Event Rate ($\sim$ evt/day)
Trigger	10^6
First	3×10^3
Second	2×10^2
Third	45
Fourth	18
Fifth	16
Final	10

5.2.5 Final FC Sample

The complete FC sample used for analysis is obtained after requiring each event's reconstructed vertex be within 2 m of the ID walls. This cut defines a fiducial volume (FV) of 22.5 kt at SK. A 30 MeV visible energy analysis threshold is set, and OD activity is restricted to be $\leq 9(15)$ PMTs to separate the FC and PC samples. This process has an efficiency of 99.4% for keeping neutrino events with a systematic uncertainty estimated below 1%.

The effect of each reduction step on the FC event rate is show in Table 5.1.

5.3 Partially Contained Reduction

PC events are most readily distinguished from FC events by the amount of activity in the OD. Accordingly, cuts based on OD information are used in the FC reduction to eliminate cosmic ray backgrounds. Such straight-forward cuts are not as useful for PC events, since by definition a particle is exiting the ID and depositing light in the OD, so the PC reduction focuses on more elaborate means of rejection of muon backgrounds. Where the cuts differ between SK-I and SK-II the latter has been included in parenthesis.

5.3.1 First PC Reduction

Particles in a PC event must travel a minimum of $\sim$ 2.5 m in the ID, which requires muons have a momentum $\geq$ 700 MeV/c. A conservative cut of 1000 (500) p.e., corresponding to muon momenta of 310 MeV/c, accumulated in the inner detector PMTs is applied to reject events unable to reach the OD. Many through-going muons are rejected at this stage by requiring that the width of the OD PMT timing distribution is $\leq$ 260 ns. For SK-I only there must also be no more than one cluster of PMTs collecting more than 8 p.e. within 8 m of the event's entrance into the OD. Through-going muons and those that clip the corner of the inner volume frequently have multiple clusters of hit PMTs well separated geometrically. Finally, as for the FC reduction, candidate events must be separated by at least 100 μs.

5.3.2 Second and Third PC Reduction

Muon backgrounds remaining at this point are targeted using a cluster-based cut slightly different than the first reduction. The OD is divided into 11×11 patches of PMTs and clusters are formed based upon charge gradients between patches. If there is exactly one such cluster found it must also have a corresponding cluster in the ID with $\Gamma > 1000$ p.e., to help eliminate stopping muons. Here Γ is the number of p.e. collected within 200 cm of highest charge ID PMT in the ID cluster. Further, events are rejected if the minimum number of hit OD tubes among the top, bottom and barrel regions is ≥ 7. Events are rejected if there are more than 6(10) tubes hit in the second highest charge cluster in the OD.

For SK-II only, events are cut if they have more hit PMTs among the top and bottom regions than a threshold returned by a function dependent upon the number of hit barrel tubes. Events are similarly cut if the number of top and bottom tubes exceeds 20. Candidate events also fail if there are more than $12 + 0.085\Gamma$ tubes in the highest charge OD cluster.

At the third step flashers are rejected using the same cut as the FC third reduction. Further, stopping muons are pared by requiring ≤ 10 hit OD PMTs within 8 m of the

OD entrance point in 500 ns. The entry point is determined by a simple point vertex fit of the ID and a p.e. weighted direction estimation.

5.3.3 Fourth PC Reduction

The fourth reduction focuses again on muons which have passed previous stages of the reduction due to limited OD activity. Two fits are employed: the simple point vertex fit and a full through-going muon fit. PC events which start in the ID should be fit poorly, particularly in terms of the entrance point to the ID and therefore have a low goodness-of-fit. Using the point fit, events are rejected if $\cos\theta \leq -0.8$, where θ is the angle between the fitted direction and the direction from the fitted vertex to the earliest saturated ID PMT. These two directions are anti-parallel for through-going muons. Events are also rejected if their reconstructed vertex is less than 150 cm to the nearest corner of the ID. Finally, events with a through-going muon fit goodness > 0.85 and a fitted track length > 30 m are removed.

5.3.4 Fifth PC Reduction

The fifth reduction is a series of specialized cuts designed to eliminate the most difficult remaining backgrounds. Low energy backgrounds are rejected if the ID observes less than 3000 (1500) p.e.. Next, if the distance between the highest charge OD hit cluster and the next highest one with more than 10 p.e. is more than 20 m the event is tagged as a through-going muon and removed. To detect other muons with more subtle OD signals, the OD is divided into patches containing 6×6 PMTs like in the second reduction. This time, the charge threshold for forming clusters is reduced to 0.5 p.e. per PMT, and if there are two or more clusters of ≥ 9 hit PMTs the event is rejected. If there are at least 7 hit PMTs in an 8 m sphere with more than 10 p.e. centered on each of the ID and OD fringes, and the difference between average timing among hits in each sphere is between 100 and 200 ns, the event is eliminated. This rather elaborate cut is designed to reject muons that travel very close to the ID wall and are reconstructed poorly. Finally, muons going through cable bundles are

Table 5.2: PC event rate after each stage of the reduction with estimated efficiencies. "Final" refers to the fiducial volume and eye-scanning performed on the sample.

Reduction Step	Event Rate ($\sim$ evt/day)	Efficiency (%)
Trigger	10^6	100.0
First	2×10^4	99.0
Second	3×10^3	94.2
Third	255	93.2
Fourth	36	87.9
Fifth	1	84.6
Final	0.6	79.7

rejected using the same counters noted in FC third reduction.

Stopping muons are considered by applying a more intensive fitter, MS-fit, which gives a better estimate of the event vertex and direction. The new vertex is projected backwards onto the ID wall to give a new entrance point, and the event is cut if there are $\geq$ 10 OD PMTs within 8 m of the entrance. Next, a separate precision fitter, TDC-fit, is applied and the angle between the reconstructed ring direction and the direction from the vertex to an OD cluster is estimated. This angle is expected to be small for PC events, and the candidate event is rejected when it is larger than 90°. Finally, a third stopping muon fit is applied. If the charge in a 42° cone defined by the reconstructed direction exceeds 60% of the total ID charge and there are more than 6 OD PMTs within 8 m of the fitted entrance position, the event is rejected when the fit goodness is > 0.

5.3.5 Final PC Selection

The final PC sample is also subject to the 2 m fiducial volume cut. Additionally PC events must have at least 10 (16) OD PMT hits in the highest charge OD cluster and more than 3000 (1500) p.e.'s seen in the ID. Each PC event is scanned by two physicists as a final check and the resulting sample is only 0.2% contaminated by

backgrounds. The list of event rates and selection efficiencies at each stage of the reduction is listed in Table 5.2. For the final data set, the PC events are divided into "OD stopping" and "OD through-going" depending on whether the particle exiting the ID stops in the OD. After a fit to the exiting particle's track, its projected length is used to compute the amount of charge expected in the OD. Events whose ratio of observed to expected charge is < 0.66 are classified as stopping and events whose ratio is larger than this cut are through-going.

5.4 Upward-Going Muon Reduction

Muon events created by the interaction of neutrinos below the detector are identical to other cosmic ray muon events in every way except for their direction. Consequently, most backgrounds arise in near horizontal bins as a result of limitations of the detector resolution. At event rates on the order of a few upward-going muons per day, the main job of the reduction is to separate these relatively few events from the continuous hail of $O(10^5)$ cosmic ray events. Each event passes through a variety of fitting algorithms and the final event sample is verified by eye.

5.4.1 Main Reduction

Upmu candidate events are required to have at least 10 in-time OD PMT hits within 8 m of a track's entry or exit point to the OD, as determined by the methods outlined in the PC reduction. Further, each event must have more than 8,000 but not more than 1.75×10^6 p.e. in the inner detector. The latter high energy cut is applied due to poor reconstruction ability of saturated electronics. Finally, corner clipping events or events with estimated track lengths less than 7 m are rejected.

The automated portion of the upmu reduction is based on the results of seven different muon fitters. Some fitters are designed to search for stopping muons and others are optimized for through-going muons or showering muons. Events are given successively to each fitter until all events have been classified, rejected or passed

through all the fitters. An event is kept if it is fit as an upward-going event with goodness above the particular fitter's threshold. Events are immediately rejected if they are fit as downward-going with goodness above threshold. If the event was below the goodness cut-off, or if it is classified as horizontal with high goodness, the event is passed on to the next fitting algorithm. After passing through all the fitters the event is kept if it was classified as horizontal by any one of the fitters, and it is rejected if it could not be fit accurately by any fitter.

Events which have made it beyond this step are passed to a more computationally intensive algorithm for estimating the event's direction. Its resolution based on MC studies is 1.5° for stopping and 1.05° for through-going muons. Details of these fitting algorithms may be found in [58, 86].

5.4.2 Eye Scanning and Final Sample

All events that have been labeled as an upward-going muon by the precise fitter are eye-scanned by two physicists for validity. If both experts agree the event is upward-going or horizontal the event is added to the final upmu sample. Discrepancies are resolved by the opinion of a third party, and about 50% of the events passing the automated portion are removed by eye-scan. The reconstructed information provided by the precise fitter is used as the official variables in the upmu sample. The detection efficiencies after the entire process are estimated at 96.2% for stopping muons and 97.2% for through-goers with 1.25% and 0.54% estimated systematic uncertainty, respectively.

After the eye-scan the final classification between stopping and through-going is made based on the following criteria. The upmu is considered stopping if there are ≥ 10 OD hits within 8 m of the projected entry in a 500 ns wide window 800 ns after the main trigger, and if there are less than 10 hits in the same time window 8 m around the exit point. If there are ≥ 10 hits near the exit point, the event is classified as through-going.

Table 5.3: Summary of the event samples used in this thesis. The 100 year SK-I and the 60 year SK-II MC are unoscillated and have been scaled to the indicated livetimes.

	SK-I		SK-II	
Event Sample	Data	MC	Data	MC
FC Livetime [days]	1489.2		803.9	
Sub-GeV e-like	3353	2891.1	1842	1613.5
Sub-GeV μ-like	3227	4286.7	1723	2320.8
Multi-GeV e-like	746	744.8	417	436.2
Multi-GeV μ-like	651	936.4	379	532.8
Multi-Ring e-like	469	645.1	247	280.8
Multi-Ring μ-like	647	1081.6	349	536.6
Upmu Livetime [days]	1645.9		827.7	
Up Through-going μ	1841	1681.4	880	1408.4
Up Stopping μ	417	714.3	208	350.7
PC Livetime [days]	1489.2		803.9	
PC Stopping	171	205.7	100	110.6
PC Through-going	740	931.5	327	488.4
Total	12262	14118.5	6472	8078.9

5.4.3 Event Summary

Both the data and MC are passed through the reduction and classified into sub-samples for analysis. The FC sample, is subdivided into six categories. Events with only one Cherenkov ring are labeled "single-ring" and separated into multi-GeV (visible energy $>$ 1.33 GeV) and sub-Gev (visible energy $<$ 1.33 GeV). Each of these is further classified as e- or μ-like based on the shape of the ring. This distinction is discussed in more detail in Section 6.3. If the event has more than one ring it is "multi-ring" and the most energetic ring determines whether it is e-like or μ-like. The PC sample and the upward-going muon samples are partitioned into "stopping"

and "through-going" as discussed above. The requirements cast upon the PC sample effectively select penetrating muons as the particle exiting the ID. Accordingly, the PC events are a very pure sample of ν_μ events. A summary of these subsamples and their respective livetimes is shown in Table 5.3.

Chapter 6

Event Reconstruction

The classification of each event discussed in the previous chapter relies heavily on the algorithms that convert the PMT charge and timing information into kinematic variables. The events used in this thesis are binned in the outgoing lepton momentum, and its direction. Direction is taken to be the cosine of the zenith angle, where by convention directly downward-going events are at an angle of zero radians relative to the vertical axis of the detector (see Figure 3.1). In this chapter the reconstruction of the vertex, direction, number of rings and particle type for contained events is discussed.

6.1 Vertex Fitting

The event vertex is estimated using two methods. Initially a vertex is sought under the assumption that all of the light collected in the inner detector was generated at a single point. Subtracting the time of flight from a tested vertex a distribution of residual PMT hit times is constructed. The point which gives maximal goodness-of-fit, defined by a Gaussian fit to this distribution, is taken as the event vertex. Then, the direction of the event is estimated as the vector sum of the charge weighted directions from the reconstructed vertex to each hit PMT. This fitting procedure is known as the point-fit.

With this vertex in hand, the opening angle of the Cherenkov cone of the brightest

ring in the event is measured to find the ring's edge. This angle is taken from the axis defined by the particle's direction. Using the amount of charge collected at an angle θ, $q(\theta)$, a pair of directions and opening angles is to tested to define a goodness-of-fit parameter,

$$G = \frac{\int_0^{\theta_t} q(\theta) d\theta}{\sin\theta_t} \times e^{-\frac{(\theta_t - \theta_0)^2}{2\sigma^2}}, \tag{6.1}$$

where θ_0 is the critical Cherenkov angle, θ_t is the tested opening angle and σ is resolution of hits taken around θ_t. Varying the direction returned by point-fit and testing various opening angles, the ring edge is found to be at the pair which maximizes G.

Now that the outer edge of the Cherenkov ring has been found, a more precise fit to the event vertex is made using an algorithm called TDC-fit. In this algorithm, PMTs that fall within the Cherenkov ring are treated differently than those outside of it when determining the best vertex and particle direction. Unlike point-fit, photons are assumed to be generated along the particle's track and the timing residual for PMTs inside of the Cherenkov ring incorporates this effect. The residual for those outside the ring is computed assuming all of the light originated at the vertex. The goodness-of-fit for a test vertex and direction is formulated incorporating this change and including the effect of water scattering.

6.2 Ring Counting

The number of rings is determined using a technique based on a Hough transformation [87] in combination with the likelihood method. The initial ring found by point-fit is treated as the main ring and other ring candidates found by the Hough method are tested against the hypothesis of a second ring. If a second ring is found to be more likely than just a single ring, the process is repeated against a possible third ring, and on up to a maximum of five rings. During this process previously found rings are kept fixed. When all rings have been found, particle type and momenta can

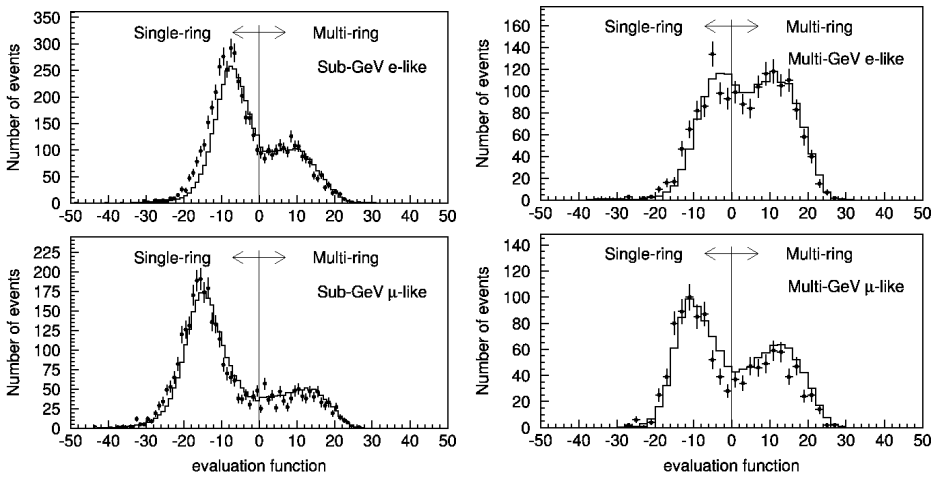

Figure 6.1: The ring counting likelihood distribution for sub-GeV events (left) and multi-GeV events (right). The data is shown by the black dots, and the MC with neutrino oscillations applied at $\Delta m^2 = 2.1 \times 10^{-3}$ eV^2 and $\sin^2 2\theta = 1.0$ is shown as the histogram. A cut at zero in the likelihood is used to separate single-ring from multi-ring events. Taken from [33].

be estimated for each of them. Using ring-separation algorithms, charge accumulated in an event can be allotted to each PMT based upon how much light it is expected to see from each ring. Finally, the FC data are separated into single-ring and multi-ring event categories based on a cut in the likelihood distribution at zero as shown in Figure 6.1.

6.3 E-like and Mu-like

Events are often further subdivided into two "e-like" and "μ-like" categories depending on whether their Cherenkov light pattern more closely resembles that of an electron or a muon. FC events are classified as such and for other reductions, individual Cherenkov rings receive the same designation. The nomenclature derives from the difference between the light projected onto the detector walls for electrons and muons. Electrons, having low mass, are continually scattered as they travel in water. As the electron scatters it emits a hard photon which, with sufficient energy may produce a separate $e^- e^+$ pair. Both the new electron and positron may produce Cherenkov

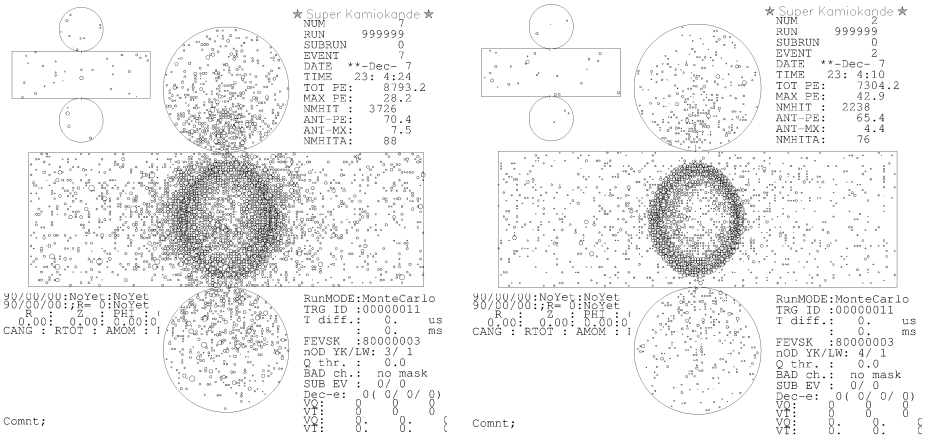

Figure 6.2: Typical MC single ring FC e-like(left) and μ-like(right) events shown in an unrolled event display of SK. The smaller cylinder in the upper left represents the OD activity and in both frames, dots represent individual hit PMT's with a radius proportional to the charge accumulated in the tube.

radiation of their own and may similarly be scattered themselves. The overlapping Cherenkov cones from the resulting electromagnetic shower coupled with the multiple scattering of the electron produces a diffuse ring in the detector. This is in sharp contrast to muons, whose large mass prevents them from being significantly deflected and therefore leave a ring with a well defined edge. Typical examples of e- and μ-like events are shown in Figure 6.2.

6.4 Particle Identification

Determining whether a ring is more e-like or μ-like is done using expected light patterns. The expected distribution of light for e-like events is computed using Monte Carlo simulations of electrons with momenta 100, 300 and 1000 MeV/c and recorded at 16.9 m from a test vertex. By interpolating these momenta the expected light pattern at a large range of distances and momenta can be extrapolated and projected onto the detector walls. For μ-like events the expected light distribution is computed analytically using muon energy loss and Cherenkov emission models. A term for knock-on electrons is also added. In both cases, the light reaching a given PMT is

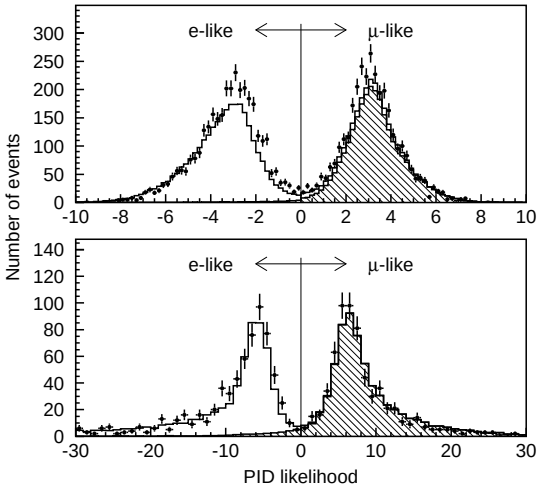

Figure 6.3: The distribution of particle identification likelihoods for Sub-GeV (top) and Multi-GeV (bottom) single-ring FC events. The hatched histogram shows the MC contribution due to CC ν_μ interactions, the black dots show the data and the empty histogram shows the total MC with neutrino oscillations applied as in Figure 6.1.

corrected for its acceptance, and the effects of water scattering and attenuation.

Using these expected light distributions the likelihood that each ring of the event is e-like or μ-like is computed. The distribution of the likelihood variable for single-ring events is shown in Figure 6.3. More details of the likelihood function can be found in Ref. [57].

6.5 Momentum Determination

After ring-separation and particle ID have been performed on the rings, precise momenta are assigned to them. The assigned momentum is dependent upon the fraction of charge accumulated in the PMTs falling within a 70° cone around target ring's reconstructed direction. Light reaching these tubes is corrected for the angular acceptance of the PMT and light attenuation in the water, and is restricted to hits falling within -50 and +250 ns of the peak of the residual timing distribution. The final charge is then combined with the particle ID results to estimate the momentum of the particle. The muon and electron reconstructed momentum resolution is estimated

Table 6.1: The vertex resolution as estimated by MC for the FC and PC event samples after the precision vertex fitter is applied.

Event Type	Resolution (cm)
Sub-GeV e-like	27
Sub-GeV μ-like	24
Multi-GeV μ-like	24
Multi-GeV e-like	49
Multi-Ring μ-like	67
PC	69

at $1.7 + 0.7/\sqrt{P \text{ GeV/c}}\%$ and $0.6 + 2.6/\sqrt{P \text{ GeV/c}}\%$ respectively.

6.6 Precision Vertex Determination

TDC-fit is based on timing information and gives a relatively poor reconstructed vertex for μ-like events. Longer track length muons are particularly susceptible due to the large time-of-flight correction to photons produced far away from TDC-fits point vertex. A more precise fitter, MS-fit, which incorporates the results of the particle identification and Cherenkov ring angle reconstruction at previous steps of the process is used to correct for this bias. The Cherenkov angle is held constant throughout the fit while the direction and vertex position are varied, comparing the expected light pattern with the observed patten. The fit is iterated to maximize both the goodness-of-fit and the particle ID likelihood. The reconstructed vertex resolutions for the contained data samples after MS-fit are shown in Table 6.1.

Chapter 7

Signatures of θ_{13} At Super-K

A non-zero θ_{13} can have a considerable effect on neutrino oscillations particularly when matter effects are involved. The interplay of the neutrino flux and detector resolutions with the matter structure of the Earth further complicate understanding the possible signatures of this parameter in the atmospheric neutrino sample. The effects of θ_{13} on Super-K data, and how the data are selected to highlight those effects using the probabilities laid out in Chapter 2 and the detector Monte Carlo are discussed below.

7.1 Preliminaries

The analysis presented in this thesis uses a radial density structure for the Earth based on the PREM model[88]. However, to save computation time, the full PREM model has been modified to provide roughly the median density predicted within its four most prominent regions: inner core ($0 \leq r < 1220$km) 13.0 g/cm^3, outer core ($1220 \leq r < 3480$km) 11.3 g/cm^3, mantle ($3480 \leq r < 5701$km) 5.0 g/cm^3 and the crust ($5701 \leq r < 6371$km) 3.3 g/cm^3. Both models are shown in Figure 7.1. In the right panel of the figure the difference between the $\nu_\mu \rightarrow \nu_e$ oscillation probabilities at θ_{13} near the CHOOZ limit for the two models is shown. Aside from a few islands, the probabilities are consistent between the full and simplified models, and when smearing introduced by the detector resolution is considered, these small differences have little

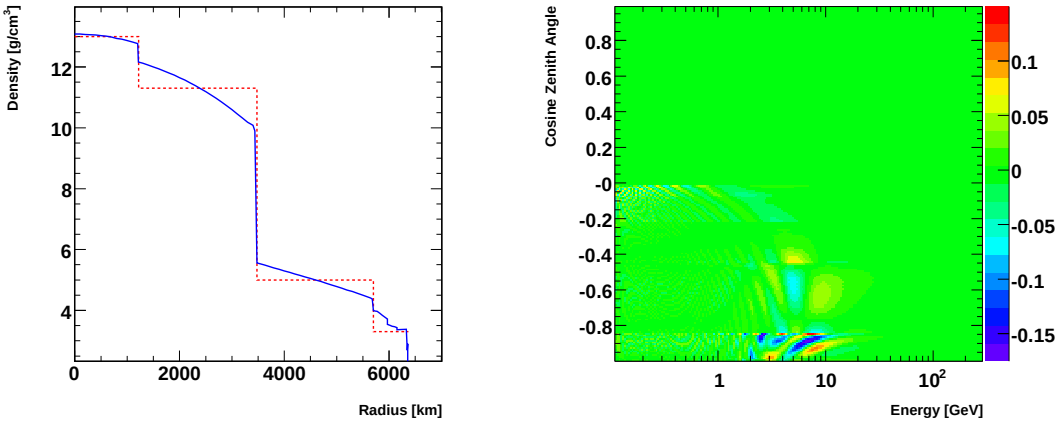

Figure 7.1: The PREM model[88] of the Earth's density in blue overlaid with the model used in this dissertation in red appears in the left panel. From left to right, the main features of the red model are denoted the inner core, outer core, mantle and crust. The right panel shows the difference between the two models on the $\nu_\mu \rightarrow \nu_e$ oscillation probability for θ_{13} at the CHOOZ limit.

effect on the final analysis.

When θ_{13} and the solar mixing terms are zero, the oscillation mechanism reverts to an effective two flavor scheme ($\nu_\mu \leftrightarrow \nu_\tau$). The survival probability, $\nu_\mu \rightarrow \nu_\mu$, in this scenario is shown in Figure 7.2 and forms the baseline for the analysis presented in [33]. It is used here as a reference against what can be expected when solar terms and θ_{13} are allowed to be non-zero for the present analysis. The vertical axis of this plot denotes the cosine of the angle the neutrino trajectory makes with the Super-K zenith. Here $\cos\Theta = -1$ corresponds to a neutrino traveling upward from beneath the detector and $\cos\Theta = 0$ represents a neutrino coming in from the horizon. Accounting for the production height in the atmosphere, P_h, the relationship between the neutrino path length, l, and $\cos\Theta$ is,

$$l = \sqrt{(\mathrm{R}_\oplus + P_h)^2 - \mathrm{R}_\oplus^2(1 - \cos^2\Theta)} - \mathrm{R}_\oplus \cos\Theta, \tag{7.1}$$

where $\mathrm{R}_\oplus$ is the Earth's radius. The relation is linear from below to very near the horizon as shown in Figure 7.2.

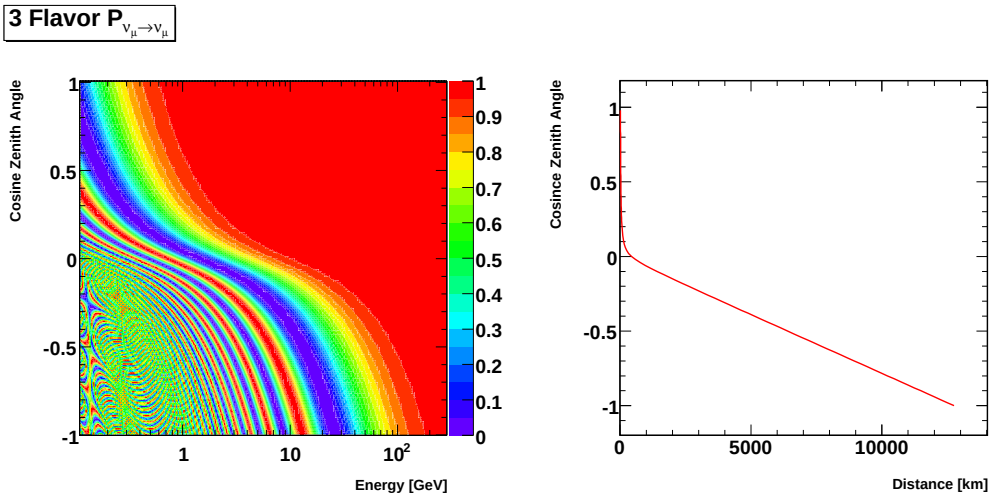

Figure 7.2: Two-flavor ν_μ survival probability as a function of energy and zenith angle (left panel). For this oscillation mode matter effects in the Earth contribute only an overall phase and do not alter the probability. The cosine of the zenith angle represents a path length as given in Equation 2.9. The relationship between the two is nearly linear (right panel) below the horizon.

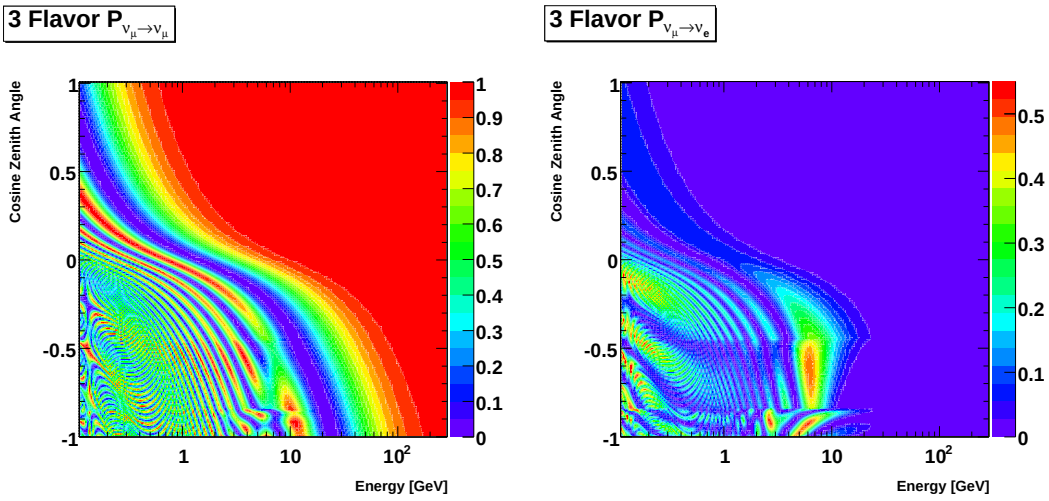

Figure 7.3: Three-flavor oscillation probabilities for θ_{13} at the CHOOZ limit for neutrinos under the normal hierarchy. The large resonance region between 3-10 GeV in the right panel arises because of the resonance effect in the Earth. Note that under the assumption of an inverted hierarchy, this resonance disappears in the neutrino channel, and instead manifests itself in the oscillations of anti-neutrinos. The effect of solar terms at the global best-fit [26] appears as the islands of probability at lower energies. Atmospheric mixing is included at $(\Delta m^2_{23}, \sin^2\theta_{23}) = (2.5 \times 10^{-3}\ \text{eV}^2, 0.5)$.

7.2 Pure Probabilities

In the context of this analysis the effect of θ_{13} is of the utmost importance. A non-zero value of this parameter implies that ν_μ oscillate into ν_e. At the CHOOZ limit the appearance probability can be quite large as shown in Figure 7.3. Interactions with the Earth's matter cause upward-going ν_μ neutrinos between 3 and 10 GeV to have up to a 50% chance of converting to ν_e. There are three main features in the figure. Resonant enhancement of the transistion probability by the MSW mechanism occurs in the Earth's core and mantle layers and is represented by the regions of large probability at 3 GeV and 7 GeV respectively. The region seen at 5 GeV and zenith angles < -0.8 arises because of interference arising at the boundary of the mantle and core layers [89]. Horizontal discontinuities appearing in the figure are a result of similar discontinuities at the boundaries of the density profile.

Depending on the magnitude of θ_{13}, the strength of this resonance varies. Figure 7.4 shows from left to right the effect of increasing θ_{13} on the ν_e appearance probability. Furthest left at zero θ_{13}, the GeV resonance structure has disappeared. At center, with a small but non-zero value of θ_{13}, the resonance is present but lacks both the breadth and intensity seen for values near the CHOOZ limit (right panel).

The inclusion of the solar mixing terms can be important as it leads to a non-zero $\nu_\mu \rightarrow \nu_e$ probability even for zero θ_{13}. Finger-like protrusions of probability for upward-going neutrinos at energies less than 1 GeV appearing in the figure illustrate this phenomenon. As the value of θ_{13} increases to the CHOOZ limit the extent and intensity of these structures increase correspondingly. For reasons outlined in Chapter 8 they are neglected in the final analysis but are included here for completeness.

At the same energies where ν_e appearance is largest there is a corresponding region of disappearance seen in the ν_μ survival probability. However, the effect of the resonance cuts across several bands of probability maxima and minima driven by the underlying atmospheric mixing. Whether this results in a possible overall observable excess or deficit of muon-like events is difficult to ascertain from the pure probability alone and is discussed below. In short, a non-zero θ_{13} would manifest itself

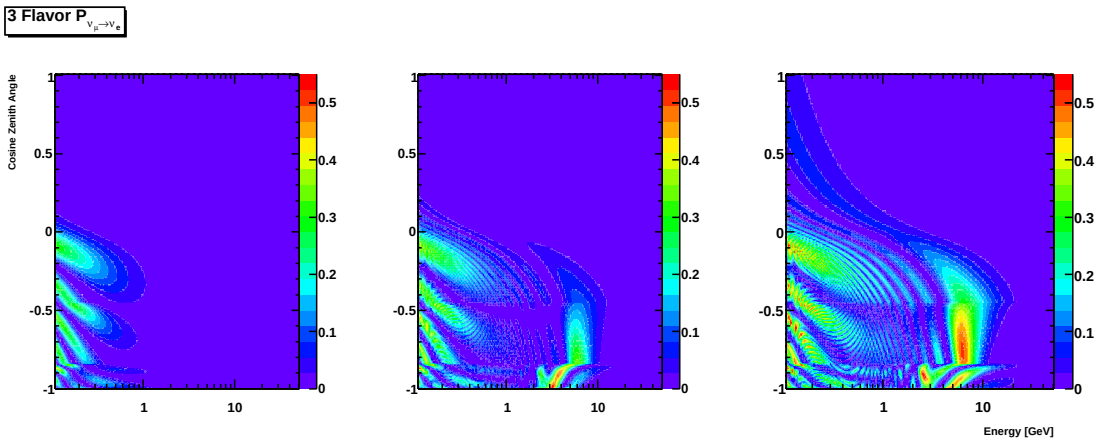

Figure 7.4: $\nu_\mu \rightarrow \nu_e$ oscillations in the normal hierarchy for increasing θ_{13} up to near the CHOOZ limit. From left to right, $\sin^2\theta_{13}$ is 0.0, 0.004 and 0.03 and all other oscillation parameters are as in Figure 7.3. The CHOOZ limit is $\sim$ 0.04 at these atmospheric mixing variables. Note that the intensity scales among the three images are the same.

at Super-K primarily as an increase in the high energy e-like event rate coming from below. Possible effects on the muon-like event rate are further discussed below.

7.3 Folding in the Neutrino Flux

Folding the expected neutrino flux at Super-K with the probabilities discussed in the previous section is used to determine the observable signals arising from θ_{13}. Since the analysis in [33] shows that the atmospheric neutrino signal at Super-K is well described by maximal two-flavor ν_μ disappearance, it is instructive to consider the influence of θ_{13} as a possible sub-leading effect relative to this more dominant mixing. In the three-flavor framework, not only is the transition $\nu_\mu \rightarrow \nu_e$ allowed, the disappearance of the ν_e flux through oscillations to $\nu_{\mu,\tau}$ becomes a competing process. Therefore, considering the $\nu_\mu \rightarrow \nu_e$ oscillation probability alone gives an incomplete picture of the effect of θ_{13}. Instead the net appearance of ν_e against the now allowed disappearance transitions needs to be examined.

Figure 7.5 shows the excess of MC events oscillated with θ_{13} at the CHOOZ limit

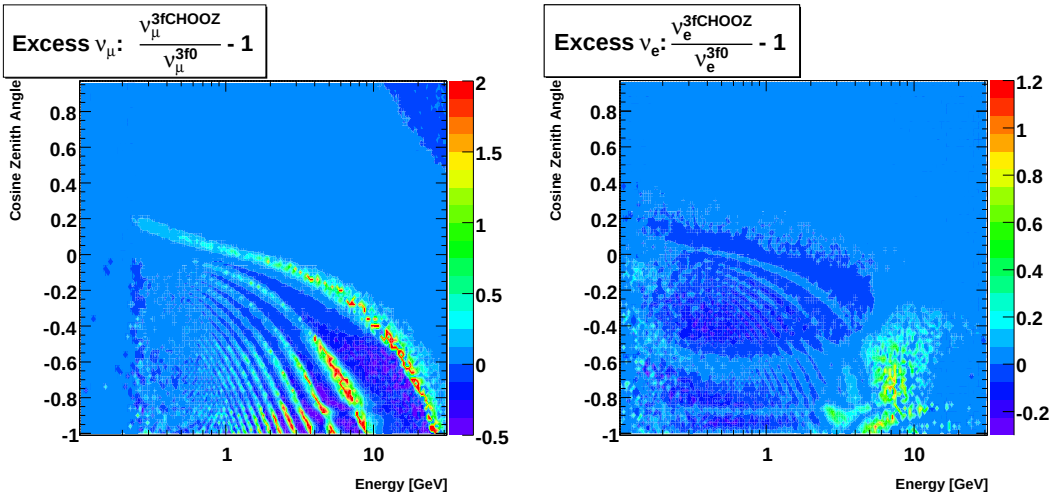

Figure 7.5: Excess of neutrino events in the SK-I 100 year MC sample for oscillations with θ_{13} at the CHOOZ limit relative to those at 0. Atmospheric and solar mixing parameters are the same as in Figure 7.3. The main MSW resonance remains visible in the ν_e event rate (right). For ν_μ events (left) the intensity scale has been restricted to a maximum of 200% relative increase to highlight alternating excess/deficit structure.

relative to oscillations at $\theta_{13} = 0$. Here, solar mixing is included, making the latter case not strictly two-flavor oscillations but representing only a small correction to the atmospheric mixing at these energies. The ν_μ event rate shows alternating bands of both excess and deficit. Deficits of near 40% next to excesses of 100% or 200% could be a useful constraint on the parameter if the neutrino energy could be perfectly reconstructed. Although energy reconstruction is imperfect, the plot indicates that μ-like events may offer additional clues from their high upward-going flux.

Electron neutrino events, however, still provide the clearest indication of θ_{13}. The high energy resonance remains visible in the atmospheric sample after incorporation of the flux. To make the most out of this expectation, the Super-K data have been refined to add a high purity high-energy e-like sample. The enhancement process is discussed in the next section.

7.4 High Energy e-like Enhancement

To exploit this possible excess of higher energy electron neutrino events, a refined multi-ring multi-GeV e-like sample has been added to the analysis. Previous analyses such as that in Ref. [33] used only single-ring e-like samples. A multi-ring e-like sample is extracted from the pool of multi-ring events using a likelihood method.

A likelihood function is constructed for each of five energy bins: 1.33-2.5 GeV, 2.5-5 GeV, 5-10 GeV, 10-20 GeV and $>$ 20 GeV using probability density functions (PDFs) built from Monte Carlo events whose most energetic ring is e-like. Four observed quantities are used to select signal events: the number of decay electrons, the maximum distance between the neutrino vertex and any muon decay electrons, the fraction of momentum carried by the event's most energetic ring, and the PID of the most energetic ring. For a given energy bin, j, the likelihood is,

$$\mathcal{L}_j = \sum_{i=1}^{4} \log(\Gamma_i^S(x_i)) - \log(\Gamma_i^B(x_i)), \tag{7.2}$$

where Γ_i represents the PDF for the i^{th} observable and x_i is the observable's measured value. The superscripts S and B label the signal and background PDFs respectively. In selecting electron neutrino events, the signal is taken to be CC $\nu_e + \bar{\nu}_e$, while the background is composed of NC and CC $\nu_\mu + \bar{\nu}_\mu$ events. An event makes it into the final sample if it passes all cuts in the FC reduction, if the event's most energetic ring is e-like, and if $\mathcal{L}_j > 0$.

An example PDF for the 5 GeV bin are shown in Figure 7.6. For both signal and background the predominant interaction mode is deep inelastic scattering. However, single pion production modes also contribute. Pions, through their decays to muons, are the main source of decay electrons in both the signal and the NC portion of the background. Signal events, though, must distribute the parent neutrino energy among the outgoing lepton as well as any pions. For this reason, pions produced by background events should in general be more energetic and thus their subsequent decay electrons should be further separated from the neutrino interaction vertex. Similarly,

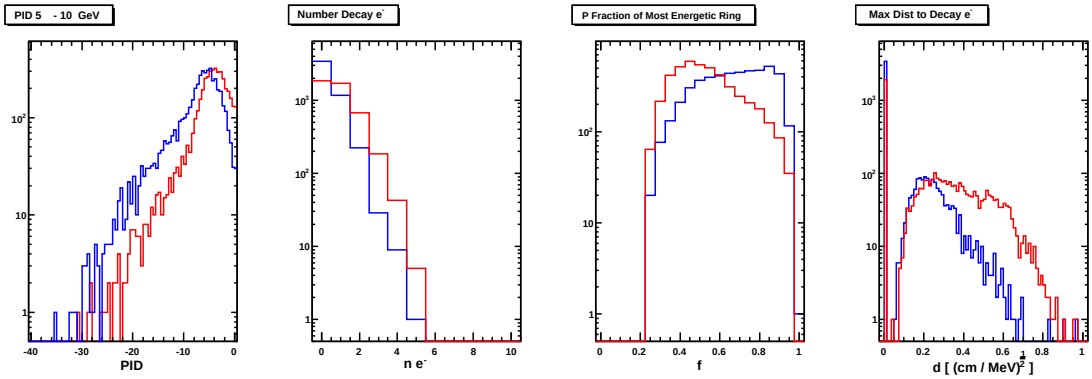

Figure 7.6: Probability density functions used to select multi-ring e-like events with total energy between 5 and 10 GeV for SK-I MC events whose most energetic ring is reconstructed as e-like. From left to right the variables are the PID of the event's most energetic ring, the number of decay electrons in the event, the fraction of momentum carried by the most energetic ring, and the maximum distance to a decay electron from the reconstructed event vertex divided by the energy of the most energetic ring. The blue histogram contains the signal CC ν_e and $\bar{\nu}_e$ events and the red histogram contains the background. The corresponding SK-II plots do not differ appreciably.

background events should have more such electrons. These ideas are reflected in the figure. The PID variable is itself the output of a likelihood function. More negative numbers indicate a stronger agreement with the e-like hypothesis for the ring.

The most clearly distinct variable between the signal and background is the fraction of momentum carried by the most energetic ring, f. Charged current ν_μ events in the multi-GeV energy regime do not differ appreciably from ν_e's in terms of this variable and should therefore be peaked at higher fractions. Plotting the same variable for ν_μ events whose leading ring is properly reconstructed as μ-like yields a distribution with the same shape as the ν_e histogram in the figure. However in these plots each event's primary ring has already been reconstructed as e-like, which for ν_μ events represent failures of the reconstruction algorithm. Using this variable is thus an exploitation of those failures and results in background events more often having lower values of f.

The method is the same as in Ref. [44] and the resulting sample purities after the likelihood selection for both SK-I and SK-II appear in Table 7.1.

Table 7.1: The expected number of events for each interaction component of the multi-ring multi-GeV e-like sample after likelihood selection for the SK-I and SK-II MC scaled to 1489.2 and 803.9 livetime days respectively. Two-flavor neutrino oscillations $\nu_\mu \leftrightarrow \nu_\tau$ have been applied at $\Delta m^2 = 2.5 \times 10^{-3}$ eV^2 and $\sin^2 2\theta = 1.0$.

	CC $\nu_e + \bar{\nu}_e$	CC $\nu_\mu + \bar{\nu}_\mu$	NC	Total
SK-I	421.5	47.5	86.5	555.2
Percentage (%)	75.8	8.6	15.6	100.0
SK-II	196.2	27.1	46.4	269.6
Percentage (%)	72.8	10.0	17.2	100.0

7.5 Incorporating Reconstruction

With the enriched multi-ring multi-GeV e-like sample, the signature of a large θ_{13} in the ν_e and ν_μ fluxes would manifest itself according to Figure 7.5. However, this plot does not include the various smearing effects the event reconstruction has on the final analysis bin contents. Plots illustrating the relative excess binned using reconstructed information appear in Figures 7.7 and 7.8.

Unfortunately the effect of imperfect reconstruction is rather striking. Though the main MSW resonance is still clearly visible in the multi-ring e-like sample, its strength has been cut by nearly a factor of two and distributed across several bins. As seen in the right panel of each figure there are still roughly 10 or more events in each of the bins in the affected region. Such an observable change will become the primary signal for the analysis in this thesis. The single-ring multi-GeV e-like sample exhibits similar effects but with slightly smaller statistics.

On the other hand, the possible alternating signatures in the high energy μ-like samples are less promising. The PC OD through-going sample, which is comprised mostly of ν_μ events, indeed illustrates bands of relative excess and deficit at high energies. However, the magnitude of the net change in each bin is small relative to the predictions of Figure 7.5. despite the relatively strong bin populations. Other muon-based samples offer slightly larger expected changes in the bin contents but

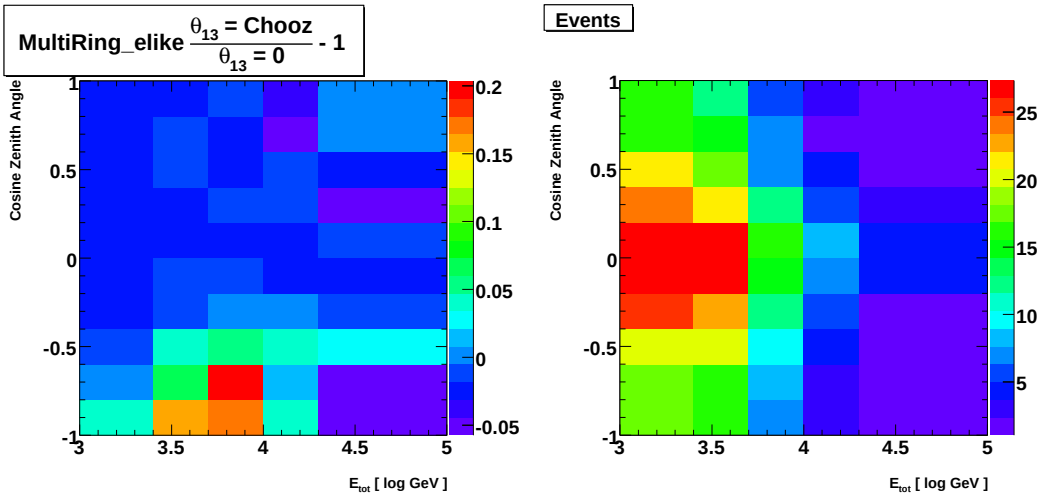

Figure 7.7: Excess of multi-ring e-like events in the SK-I 100 year MC sample for oscillations with θ_{13} at the CHOOZ limit relative to those at $\theta_{13} = 0$ and binned in reconstructed quantities (left). The plot reflects the potential signature of non-zero θ_{13} after incorporating the neutrino fluxes, oscillation probabilities and effects of the event reconstruction. E_{tot} refers to the total energy of all rings in the event. The MSW resonance is still visible but its magnitude has decreased significantly relative to Figures 7.5 and 7.3. The number of MC events after oscillations at the CHOOZ limit in the same binning is shown for the SK-I livetime (right).

with smaller statistics. Certainly the μ-like events will provide additional constraints on the size of θ_{13}, but their effect is much smaller relative to that of the high energy e-like samples. Accordingly, they are considered a much weaker potential signal here.

7.6 Normal vs. Inverted Hierarchy

The plots presented above have all been created under the assumption of the normal mass hierarchy. If the inverted hierarchy is used instead, the resonance will affect anti-neutrino events. Due to the lower cross section for $\bar{\nu}_e$ interaction (see Figure 4.3), the overall effect of a large θ_{13} is expected to be smaller than for the normal hierarchy. Figure 7.9 shows that at the strongest point of the resonance, the expected excess has been cut by more than a factor of two. In consequence, less sensitivity is expected from an analysis using the inverted scheme.

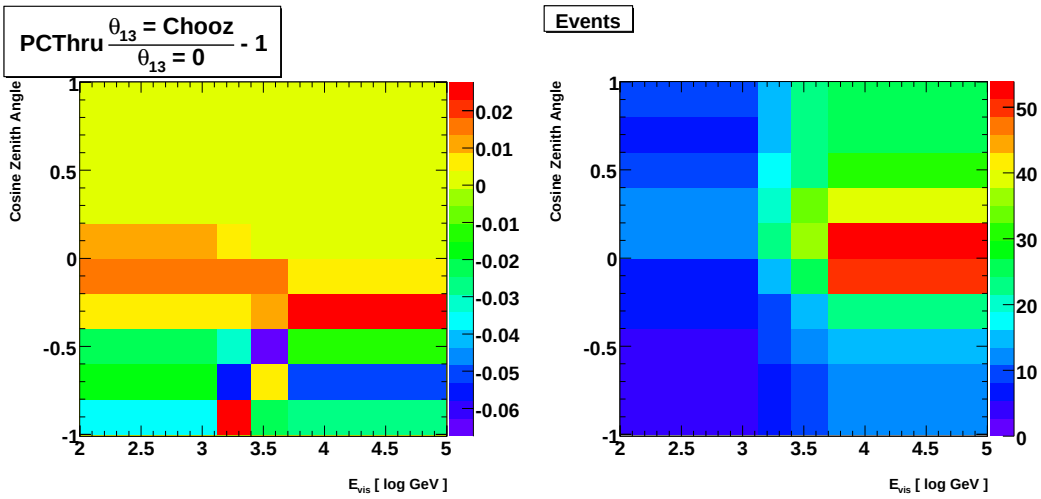

Figure 7.8: As in Figure 7.7 but for the PC through-going sample which is dominated by ν_μ. Here the horizontal axis specifies the visible energy of the event.

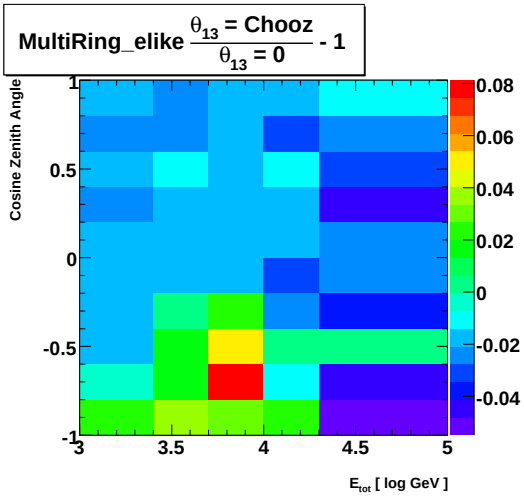

Figure 7.9: As in Figure 7.7 but under the inverted mass hierarchy assumption.

Chapter 8

Oscillation Analysis

After the reduction and reconstruction phases of reprocessing, the data and MC are suitable for analysis. The general analysis framework aims to compare the data against the MC for different oscillation models. A particular oscillation model specifies a value of each of the oscillation parameters and the MC is then oscillated according to that model. To test a model's compatibility with the data, a goodness of fit statistic is computed between the two. A set of oscillation models forming a grid in the parameter space is chosen and this analysis performs a search over the lattice for the best agreement with the data. This condition is defined as the minimum χ^2 among the test points. Confidence level contours are then drawn expressing the degree of agreement with the data relative to the model giving the best fit. Both the SK-I and SK-II datasets are fit individually and then combined and re-fit jointly as the SK-I+SK-II data. Further, each of these is fit under the assumption of both a normal and inverted mass hierarchy. Detailed descriptions of the process and the results are presented below.

8.1 Oscillation Space

To perform the analysis a lattice consisting of 83,025 points is chosen among three oscillation parameters. The dimensions of the grid are specified in Table 8.1. Only three parameters are considered because the analysis adopts a single dominant mass

Table 8.1: Details of the oscillation space considered in the analysis. The solar terms, $\sin^2\theta_{12}$ and Δm^2_{21}, have been excluded.

Parameter	Points	Minimum	Maximum
$\sin^2\theta_{13}$	81	0.0	0.5
$\sin^2\theta_{23}$	25	0.2	0.8
Δm^2_{23} [eV^2]	41	1×10^{-3}	1×10^{-2}

framework. That is, experimentally the "solar" mass splitting, Δm^2_{12}, is known to be much smaller than the "atmospheric" mass splitting Δm^2_{23} in magnitude [25, 23, 33]. For neutrinos with a few hundred MeV of energy the effect on the oscillation probability of the solar mass splitting is the most relevant. Excesses in the ν_e event rate at these energies arising from $\nu_\mu \to \nu_e$ transitions driven by this mass splitting when the ratio of the neutrino fluxes $\nu_\mu/\nu_e \sim 2$ can be upwards of 5% but are strongly suppressed in the atmospheric sample when $\sin^2\theta_{23} = 0.5$ [90]. This latter condition is favored by [33] suggesting that in conjunction with averaging performed in this region (see below) it is reasonable to exclude this parameter from the analysis. Accordingly, only the atmospheric splitting is considered with $\Delta m^2_{23} > 0$ representing the normal mass hierarchy and $\Delta m^2_{23} < 0$ the inverted hierarchy. The solar terms, Δm^2_{21} and $\sin^2\theta_{21}$, are set to zero in this analysis.

8.2 Monte Carlo Manipulations

The analysis presented here relies on 100 years of SK-I and 60 years of SK-II Monte Carlo constructed as discussed in Chapter 4. However, individual events contribute differently to the analysis bins as described below.

8.2.1 Oscillation Probabilities and Weights

Each CC MC event's true zenith angle direction is used to compute an event path length. If the event is coming from below the horizon the matter density profile

along its trajectory is also computed as in Chapter 7. Accordingly, the neutrino crosses several layers of constant density and the transition matrix across each layer is calculated using the techniques in Sections 2.3 and 2.3.2. The total amplitude is then the product of these n matrices,

$$A = \prod_{i=0}^{n-1} A_{n-i} \tag{8.1}$$

and the corresponding oscillation probability is

$$P(\nu_\alpha \to \nu_\beta) = |A_{\alpha\beta}|^2. \tag{8.2}$$

Neutral current MC events are not oscillated.

In the three-flavor framework, oscillations from $\nu_e \leftrightarrow \nu_\mu$ are allowed and the effect is incorporated by weighting each charged current event as

$$w = \begin{cases} P(\nu_e \to \nu_e) + \frac{\phi_e}{\phi_\mu} P(\nu_\mu \to \nu_e), & \text{if } \nu_e \\ P(\nu_\mu \to \nu_\mu) + \frac{\phi_\mu}{\phi_e} P(\nu_e \to \nu_\mu), & \text{if } \nu_\mu \end{cases}$$

where ϕ_x is the energy and zenith angle dependent neutrino flux from Ref. [60]. In this way the second term in each of these equations includes the appearance probability with the flavor-correct energy and zenith angle distribution.

Finally, all events are then weighted to adjust for the solar modulation of the neutrino flux. Changes in the intensity of the solar wind modulate the flux of low energy cosmic rays impinging upon the atmosphere, which in turn affects the low energy neutrino flux. In order to account for the solar cycle during the run period SK-I (SK-II) MC events are weighted by 70% (30%) of the predicted neutrino flux at minimum solar activity and 30% (70%) of the flux at the solar maximum. These flux weights are a function of the neutrino direction, energy and type.

8.2.2 Averaging

Recalling Equation 2.9 and Figure 7.2 the oscillation probability $\nu_\mu \leftrightarrow \nu_\tau$ changes rapidly for small changes in the neutrino path length to energy ratio (L/E) when this

ratio is large. Rapid changes in this oscillation phase are difficult to sample completely when the accumulated statistics are small, making the final oscillation contours more sensitive to statistical fluctuations in the MC. Given a large amount of MC, the effect of incomplete sampling can be alleviated, but alternative methods are employed when the MC statistics are not sufficient.

For each of SK-I and SK-II there are 20 times more MC than collected data but because of the large value of the oscillation phase in several bins of the analysis this is not sufficient. In the case of a pure ν_μ disappearance analysis, where a two-flavor oscillation scheme is valid and matter effects are not considered, a simple cut can be made. The standard zenith angle analysis at Super-K [33] averages the second sine function in Equation 2.9 to 0.5 when its argument is $> 2\pi$, roughly corresponding to L/E $> 2 \times 10^3$ km/GeV. Making the cut at 2π is a somewhat arbitrary choice and is made based on changes in the expected sensitivity to oscillations. Since this averaging implies a loss of information on one of the measured parameters, Δm^2, care is appropriate. Increasing values for this cut imply fewer averaged events but beyond 2π the effect on the extent of the expected sensitivity to Δm^2 ceases to change. Averaging more events by lowering the cut, though, begins to erode sensitivity, particularly below π.

The effect of this averaging is shown in Figure 8.1. In both panels the weight including two-flavor oscillations assigned to each CC ν_μ event in the MC is shown as a function of its L/E value. Oscillations without any averaging are shown in the left panel. The change induced by the above averaging is shown as the cluster of black points around 0.5 extending above the cut value in the right panel. In both cases the sinusoidal nature of the oscillations is clear but has a width that results from the application of the solar flux weights discussed in Section 8.2.1.

Averaging in this manner is straightforward. However, as discussed in Chapter 2 the three-neutrino oscillation probability in varying matter cannot be written in a simple closed form. Further, the presence of matter obfuscates quantities one might average with such as the oscillation length. The problems associated with "low" MC

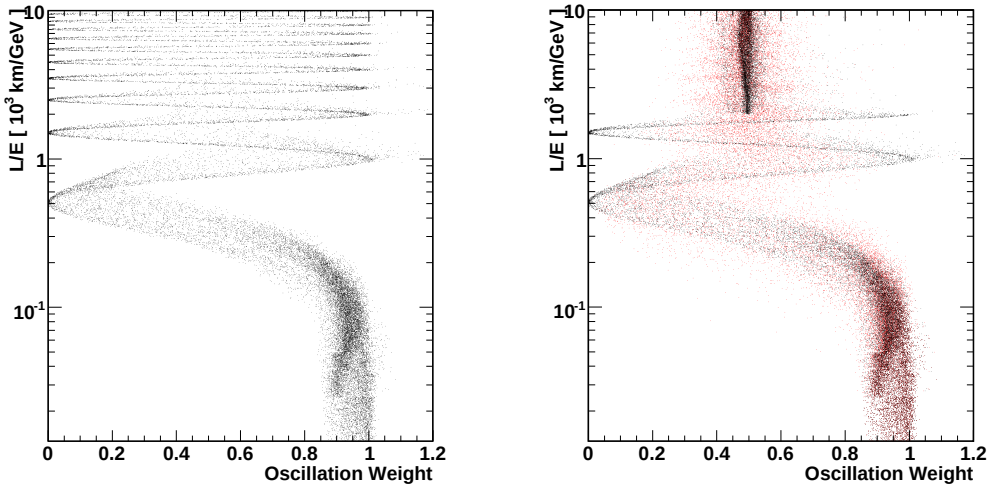

Figure 8.1: Muon MC event weights as a function of L/E after oscillations with and without averaging effects at $(\Delta m^2, \sin^2\theta_{23}, \sin^2\theta_{13}) = (2.5 \times 10^{-3}\ \mathrm{eV}^2, 0.5, 0.0)$. The left panel illustrates clearly the sinusoidal dependence on L/E reminiscent of Equation 2.9 for oscillation without any averaging. At right, the effects of simple phase averaging for $1.2667\Delta m^2 L/E > 2\pi$ (black) and for the full averaging performed in this dissertation (red) are shown (see Sections 8.2.4 and 8.2.5).

statistics are still present in the three-flavor analysis, however, so alternative methods to overcome the deficiency must be invoked. Since the two-flavor disappearance is the dominant oscillation effect, the three-flavor averaging scheme must also remain consistent with the two-flavor result. This is achieved using the production height, mantle and nearest neighboring averaging schemes discussed below.

8.2.3 Neutrino Production Height

It is not possible to know the production height above ground level in the atmosphere of neutrino events entering Super-K. For low energy neutrinos near the horizon the effect of small changes in the production height can lead to changes in the total path length large enough to significantly alter the oscillation probability. Events coming from well below the horizon on the other hand are only marginally affected by this uncertainty as the production height represents only a small fraction of the overall path length. To account for this effect in near-horizontal and downward-going events,

the production height is averaged over. Using 20 production heights chosen from the data in Ref. [60], 20 oscillation probabilities are computed for each MC event. The final probability assigned to the event, however, is their average. Production heights vary as a function of neutrino energy, direction and flavor but are typically less than 40 km.

8.2.4 Mantle Averaging

Incorporating matter effects into the oscillation framework prohibits the use of simple cuts on the oscillation phase since this phase is no longer well defined along the entire neutrino path. Statements can be made, however, piecewise along its length. The path length in the mantle region (see Figure 7.1), l_m, of each event is compared to its vacuum oscillation length, λ. If $l_m > 2\lambda$ four probabilities are computed for the event using $l_m + n\lambda/2, n = 0, .., 3$ as the path length in the mantle. The probability assigned to the event is then the average of these four. For events whose trajectory through the mantle is interrupted by passage through the core region, l_m is taken as the distance across the section of the mantle nearest the detector.

Using this procedure many events in the high L/E region are averaged while preserving the effect of interactions with the matter beneath the mantle. Figure 8.2 shows the effect this averaging has on the ν_μ survival probability from Figure 7.3. Notice that averaging in the mantle does not extend into the MSW region and hence does not affect this analysis' main sensitivity to θ_{13}. On the other hand, the averaging only partially covers the high phase oscillation region in Figure 8.2 and is not by itself sufficient.

8.2.5 Nearest Neighbor Averaging

To complement the mantle averaging, a third averaging scheme based on the Super-K Monte Carlo is employed. Before computing oscillation effects, the 20 nearest neighbors in reconstructed energy (lepton momentum if single-ring) for each event are found. Then, the true neutrino energy of each of these neighbor events is used to

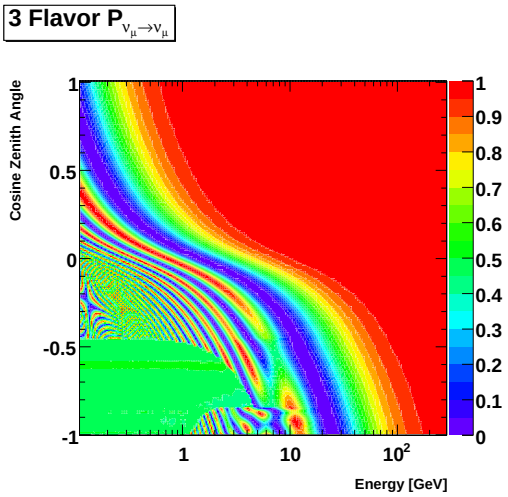

Figure 8.2: The effect of mantle averaging on the $\nu_\mu \to \nu_\mu$ survival probability. The unaveraged probability appears in the left panel of Figure 7.2.

compute an oscillation probability for the parent event using the parent's trajectory. Again, the final oscillation probability is the average of these 20. Events that undergo mantle averaging however, are already well averaged and are not subjected to this averaging. Moreover, to avoid excessive calculations the production height and neighbor averaging schemes are merged. Instead of averaging the 20 neighbors over each of the 20 selected production heights, each production height is assigned to only one of the neighbors during the computation neighbor probabilities.

The combination of the nearest neighbor, production height and mantle averaging represents the full scope of averaging in the analysis. Its effect on the ν_μ MC weights appears as the red marks in the right panel of Figure 8.1. Under this averaging scheme the first dip in the oscillation probability remains visible much like the simple phase averaging case above. Beyond the first dip the probability is increasingly obscured and begins to collapse to the averaged value from the phase cut at higher L/E. Since the averaging is based indirectly on the inefficiency of the reconstruction algorithm and taken from the MC, it represents roughly a flux-weighted averaging effect. Its strength is apparent from the diffusion of the red marks in the figure. For events with low reconstructed energy, the distribution of MC truth energies among its neighbor

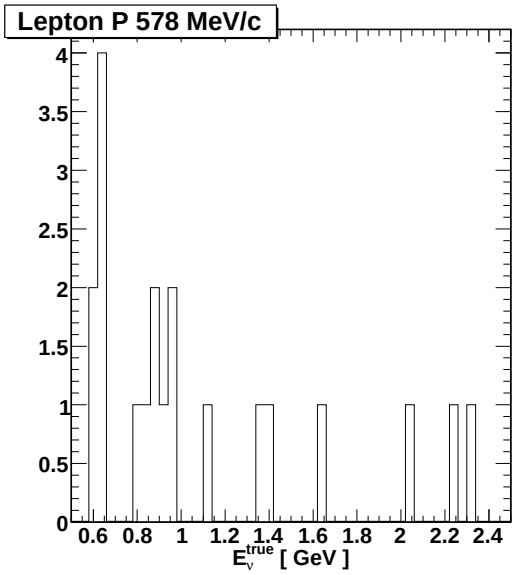

Figure 8.3: The 20 nearest neighbor energies for a single ring muon event in the SK-I MC with reconstructed lepton momentum of 578 MeV/c. The width of this distribution makes the oscillation probabilities computed in the nearest neighobr avergaing scheme to be diffuse.

events can be broad and thereby result in a well averaged probability. See Figure 8.3. Since this type of averaging depends heavily on the choice of MC sample used it is not an ideal averaging scheme.

8.3 Formulation of χ^2

In order to take advantage of the improved sensitivity accompanying a finer binning scheme, the likelihood in this thesis is based on Poisson probabilities. For $\sim O(1)$ number of expected events, with small error on that expectation, the resulting reduced χ^2 of a sparsely populated bin is only marginally larger than 1.0. The likelihood for N bins indexed by n is taken to be

$$\mathcal{L}(E, \mathcal{O}) = \prod_n \frac{e^{-E_n} E_n^{\mathcal{O}_n}}{\mathcal{O}_n!} \tag{8.3}$$

In this equation E_n and $\mathcal{O}_n$ are the expected and observed bin contents respectively.

Defining a χ^2 as the log likelihood ratio yields

$$\chi^2 \equiv -2\ln\frac{\mathcal{L}(E,\mathcal{O})}{\mathcal{L}(\mathcal{O},\mathcal{O})} = 2\sum_n \left(E_n - \mathcal{O}_n + \mathcal{O}_n \ln\frac{\mathcal{O}_n}{E_n}\right). \tag{8.4}$$

8.4 Pull Method of Systematic Errors

A prescription given by the authors of Ref. [91] can be used to incorporate the effect of systematic errors into the bin expectation for independent sources of error. That is, the expected number of events in a bin changes with changes to an added systematic error parameter. In this scheme Equation 8.4 can be rewritten with the substitution

$$E_n \to E_n(1 + \sum_i f_n^i \epsilon_i). \tag{8.5}$$

In this equation the quantity f_n^i represents the fractional change in the n^{th} bin's event rate due to a variation of the systematic error parameter ϵ_i. For each error, i, the parameter ϵ_i is estimated during the fit to the χ^2 and the resulting distribution of the quantity ϵ_i/σ_i is Gaussian univariate. In this way, the size of the fitted ϵ and hence the strength of its systematic error's effect is constrained through the addition of a penalty term to Equation 8.4. The full χ^2 becomes

$$\chi^2 = 2\sum_n \left(E_n - \mathcal{O}_n + \mathcal{O}_n \ln\frac{\mathcal{O}_n}{E_n}\right) + \sum_i \left(\frac{\epsilon_i}{\sigma_i}\right)^2. \tag{8.6}$$

$$\chi^2 = 2\sum_n \left(E_n(1 + \sum_i f_n^i \epsilon_i) - \mathcal{O}_n + \mathcal{O}_n \ln\frac{\mathcal{O}_n}{E_n(1 + \sum_i f_n^i \epsilon_i)}\right) + \sum_i \left(\frac{\epsilon_i}{\sigma_i}\right)^2. \tag{8.7}$$

The advantage of using this method is that with the incorporation of the "pulls" in Equation 8.5 the χ^2 can be minimized over the ϵ_i readily. At the χ^2 minimum $\partial\chi^2/\epsilon_l = 0$ for every l. Therefore, differentiating χ^2 and grouping terms in only one power of ϵ the minimization problem is specified by the solution of a $K \times K$ linear

matrix equation,

$$\sum_k \mathcal{M}_{lk}\epsilon_k = \mathcal{V}_l \tag{8.8}$$

$$\Rightarrow \sum_{k,n}\left(f_n^l f_n^k \mathcal{O}_n + \delta_{lk}\frac{1}{\sigma_k^2}\right)\epsilon_k = \sum_n \mathcal{O}_n f_n^l \left(\frac{1}{1+\sum_i f_n^i \epsilon_i} + \sum_i f_n^i \epsilon_i + \frac{E_n}{\mathcal{O}_n}\right). \tag{8.9}$$

The matrix, $\mathcal{M}$, is symmetric and invertible so long as there does not exist an error i with $f_n^i = 0$ for every n. If the number of bins is much larger than the number of systematic errors this method has considerable advantage relative to a covariance-matrix approach as the solution is found by inverting a $K \times K$ matrix, rather than an $N \times N$ matrix. Since the right hand side of Equation 8.9 itself contains terms in ϵ this equation is solved iteratively beginning with $\epsilon_i = 1$ for every i until the value of χ^2 stabilizes.

8.5 Systematic Errors

By using the "pull" method, the incorporation of the effect of systematic errors is handled by the systematic error coefficients, f_n^i , in Equation 8.5. In this analysis these f_n^i are calculated using the atmospheric neutrino Monte Carlo. The systematic error coefficients are assumed to have a linear effect on the bin content B^0 and f_n^i is taken to be the slope of the line between its contents at $\pm\sigma$,

$$f_n^i = \frac{B_n(+\sigma_i) - B_n(-\sigma_i)}{2B_n^0}. \tag{8.10}$$

$B_n(\pm\sigma)$ is the sum of the weights, $\gamma_i^{\pm}$, of each MC event falling in the bin adjusted by the effect of the i^{th} systematic error. The weights are of the form

$$\gamma_i^{\pm} = (1 \pm g_i)P_s, \tag{8.11}$$

where P_s is the event's survival probability computed at $(\Delta m^2, \sin^2\theta_{23}, \sin^2\theta_{13}) = (2.0 \times 10^{-3}\ \mathrm{eV}^2, 0.5, 0.0)$ and g_i is a function dependent upon the event kinematics. Equation 8.10 is often different from one due to errors being applied asymmetrically

across the bin via g. That is, not every event in a bin is subject in the same way to the effect of a particular error.

As an example, for the systematic error on the ν_μ to ν_e flux ratio whose uncertainty is σ_j, g_j is taken to be

$$g_j = \begin{cases} \sigma_j/2, & \text{if } \nu_\mu \\ -\sigma_j/2, & \text{if } \nu_e. \end{cases}$$

Since the number of each flavor in a given bin is not the same due to differences in the respective fluxes, the corresponding f_n^i is different from one. The weighting function for the systematic uncertainty in the ratio $(\nu_\mu + \bar{\nu}_\mu)/(\nu_e + \bar{\nu}_e)$ is

$$g_k = \begin{cases} 0.1 \log_{10} E^{2.7} - 0.004, & \text{if } \nu_\mu \text{ or } \bar{\nu}_\mu \\ -0.1 \log_{10} E^{2.7} - 0.004, & \text{if } \nu_e \text{ or } \bar{\nu}_e, \end{cases}$$

where E is the event's energy. Now the weight has an explicit energy dependence and therefore the value of the corresponding f_n^i is sensitive to the bin size and event reconstruction. Note that depending on the bin populations an individual f_n^i may be either positive or negative. More detail on the systematic errors is presented in Section 8.5.1.

From Equation 8.11 the systematic error coefficients are dependent upon the choice of oscillation parameters in P_s. Accordingly, f_n^i should be computed for every point in the oscillation space of the analysis. The effect of computing a different f_n^i for each point in the oscillation space under investigation here, though, is small. Therefore they have been computed only at the best fit oscillation parameters from Ref. [33] as stated above.

8.5.1 Listing of Systematic Errors

Below is a brief description of the systematic errors considered in this analysis and their corresponding widths, σ. Where these widths differ between SK-I and SK-II, the value for the latter has been included in parentheses. In total there are 66 sources

of systematic error considered for the fit to SK-I+SK-II, 26 of which are common between SK-I and SK-II. When the data sets are fit individually the 20 errors from the unused data set are excluded giving a total of 46 systematic errors.

Neutrino Flux Errors

Errors on the neutrino flux, spectrum and flavor ratios are considered common between the SK-I and SK-II data sets.

1. **Absolute Normalization**

   The absolute normalization is known poorly and its error is considered free during the fitting. The systematic does not contribute to the penalty factor in Equation 8.6.

2. **Flux Ratios**

   Though the absolute value of the neutrino flux is known relatively poorly, the ν_μ to ν_e flux ratio is much better understood. The error on the quantity $(\nu_\mu + \bar{\nu}_\mu)/(\nu_e + \bar{\nu}_e)$ is taken to be 3% for neutrino energies both below 5 GeV. Above 5 GeV the error scales linearly with log E_ν from 3% to 10% at 100 GeV. During the fit a positive value of the ϵ corresponding to this error indicates an increase in the total flux of muon neutrinos. Further, the error on the $\nu_\mu/\bar{\nu}_\mu$ and $\nu_e/\bar{\nu}_e$ ratios below 10 GeV is taken to be 5% uncertain. Beyond 5 GeV however, the uncertainty again rises log-linearly in E_ν from 5% to 10% for ν_e and to 25% for ν_μ at 100 GeV. Positive values of the fitted parameter indicate an increase in MC neutrino events, while negative values indicate an increase in anti-neutrino events. The rigidity cutoff of the Earth's magnetic field contributes an energy-dependent uncertainty on the ratio of upward-going to downward-going events. For each of the event subsamples this uncertainty is less than 5%. The error is assumed to be fully correlated among the samples through a single ϵ which

when fit positively increases the number of upward-going events. Accordingly, the penalty term for this systematic uses a conservative value of $\sigma = 5\%$. Finally, the enhancement of the horizontal flux relative to the vertical flux is also treated as a systematic that is fully correlated among the various subsamples. Conservatively, the error is again set to 5%.

Production Uncertainties

1. K/π **Ratio**

   There is a 20% uncertainty placed on the ratio of K to π production by cosmic ray interactions in the atmosphere. At increasingly large primary cosmic ray energies neutrino production becomes dominated by K decays and uncertainty in this ratio contributes to the uncertainty in the high energy portion of the flux ratios.

2. ν **Production Height**

   Uncertainty in the neutrino production height in the atmosphere affects only the oscillation probability assigned to the MC as discussed above. For upward-going events this uncertainty produces a negligible effect, but for events near and above the horizon it is treated as a systematic error. This error is treated by considering the effect on the production height and hence oscillation probability in the f_n^i computation stemming from a 10% change in the atmospheric density. Accordingly, the width assigned is 10%.

3. **Energy Spectrum And Sample-by-Sample Normalization**

   The energy spectrum of the primary proton flux is well described by $E^{-2.74}$ where E is the proton energy. The uncertainty in this spectral index above 100 GeV

is estimated as 0.05% and 0.03% below. Changes in the predicted flux are made arbitrarily around 10 GeV. However, an error on the spectral index is not sufficient to account for the differences in various flux calculations. Variations among these models are accounted for via a normalization error on the FC multi-GeV and PC+upward stopping muon samples, whose energy spectra peak above 10 GeV and thereby avoid overlapping with the energy spectrum systematic. The size of the uncertainty in both of these samples is estimated as 5%.

Neutrino Interaction Systematics

Systematic errors arising from the interaction cross sections and the resulting kinematics are common between SK-I and SK-II.

1. **Axial Mass**

   A 10% error on the axial mass parameter, M_A, is assumed in the analysis. Fitting a positive value for the systematic results in a larger axial mass and hence a larger quasi-elastic CC interaction cross section. The SK interaction MC has been generated at $M_A = 1.1\ GeV$ though more recent measurements measure its value at 1.2 GeV[69].

2. **Meson Production**

   The systematic uncertainty on the single meson production cross section is assumed to be 10%. For multiple π production there are two sources of error. First, there is a 5% uncertainty in the cross section. The difference in the q^2 dependence of the cross section between the models in Refs [92] and [93] is applied as an additional 1-σ systematic error of width 1%. Coherent-pion production is also assigned a 30% systematic error, though this production mode represents only a small fraction of the events in the MC.

3. **Quasi-Elastic Scattering**

   Quasi-elastic (QE) scattering off bound nucleons in ^{16}O is modeled using the relativistic Fermi-gas model in [68] which assumes a flat momentum distribution up to a fixed Fermi-momentum. However, an independent model by Singh and Oset [94] uses a local and varying Fermi-momentum distribution. Therefore, a model dependent systematic error is ascribed as the difference between the cross-section predictions of the two with $\sigma = 1\%$. Additionally, a separate 10% systematic is assigned representing the total uncertainty in the QE scattering cross section.

4. **Nuclear Effect in ^{16}O**

   The uncertainty in the mean free path of hadrons inside of the ^{16}O nucleus is considered as a 30% error. Pion scattering and absorption processes are considered in tandem and a positive fit to this ϵ implies stronger nuclear interactions. The $1 - \sigma$ uncertainty in the out-going pion energy spectrum is taken to be the difference in the predictions of [65] and [66] and is 1%.

5. **Other Cross Section Uncertainties**

   An uncertainty of 20% is attributed to the NC to CC ratio. The large neutrino energy needed to produce the τ lepton makes ν_τ interactions in SK relatively rare, but they are nonetheless present in the data [95]. Accordingly, ν_τ events are added to the MC and an error on the CC cross-section is included as a 30% systematic.

Event Selection Systematics

Since the photo-coverage differs between SK-I and SK-II the two phases differ in

their event reconstruction ability. Improvements to the reduction and reconstruction algorithms in SK-II, though, have in parts compensated for its decreased coverage.

1. **Contained Reduction**

   Systematic errors are placed on the FC and PC reduction processes outlined in Chapter 5. The errors themselves are measured by comparison between the data and MC for cuts made in the reduction process. For FC reduction in SK-I (SK-II) the error assigned is 0.2%(0.19%). PC reduction is 2.6% (4.0%) uncertain. An additional error is placed on the separation of FC and PC events due to systematic uncertainty in the discriminating cut on the number of hit tubes in an OD cluster. This systematic is therefore assumed to be completely anti-correlated such that a positive fit to the error parameter simultaneously provides more FC and less PC events. Its width is 0.9%(0.5%). Similarly an uncertainty of 12%(12%) is placed on the cut separating PC stopping from PC through-going events.

2. **Upward-Going Muons**

   A goodness parameter is used to select the upward-going muon sample. The MC and data have different distributions of the parameter and that difference is taken as a correlated error between upward-stopping and upward-through-going events. This error is taken to be $\sigma = 1\%(1\%)$ in the analysis. Additionally the uncertainty in the separation of stopping and through-going is taken to be 0.4%(0.3%).

3. **Event Contamination**

   Systematic uncertainties in the propagation of hadrons arising from the differences between the GEANT and FLUKA simulation packages are considered.

This systematic error affects the number of hadrons that are reconstructed as μ-like for single-ring NC events and has a width of 1.0%. Backgrounds arising in e-like events, such as PMT flasher and neutron-induced events, are considered a source of systematic error with uncertainty 1.0%(1.0%). The contamination of μ-like events by cosmic rays is similarly a 1.0%(1.0%) error. Finally, non-ν backgrounds are considered in the most horizontal bin of the upward-going muon samples and are described by an error of width 3%(3%) for the through-going sample and by a separate error of width 17%(24%) for stopping muons.

4. **Multi-GeV e-like Backgrounds**

   Contamination of the multi-ring multi-GeV sample by CC ν_μ events is considered as a separate systematic error. The size of the error is computed by performing a fit of the MC to the data likelihood distribution discussed in Section 7.4. During the fit the CC ν_μ normalization in the MC is changed independently of the signal + NC normalization. By comparing the ratio of the fitted fraction of ν_μ events to the unfitted fraction a systematic uncertainty of 20%(55%) is assigned. A similar procedure is followed to estimate the contamination in the single-ring multi-GeV e-like sample, but using the ring counting likelihood instead. The results provide a systematic uncertainty of 14%(32.6%) on this sample.

Event Reconstruction Systematics

1. **Ring Separation**

   Like the sample reduction errors the ring separation error is considered by examining the differences in reduction variables between the data and MC. For this analysis, the ring separation determines the whether an event falls into the single-ring or multi-ring sample and therefore the systematic error on this selection is assumed to be fully anti-correlated. That is, an increase in the number

of single-ring events, whether e- or μ-like is accompanied by a decrease in the number of multi-ring events. The width assigned is 10%(10%).

2. **Particle Identification**

   Particle identification systematic errors are treated similarly. The uncertainty is assumed to be anti-correlated between e-like and μ-like events but there is no correlation among single- and multi-ring events. Single-ring PID is assigned an uncertainty of 1%(1%) and multi-ring PID is 10%(10%).

3. **Energy Scales**

   A 2.0% (2.5%) uncertainty is assigned to the absolute energy scale of SK such that a positive fitted parameter increases the amount of visible energy in the MC. This change in visible energy affects the binning and oscillation probability assigned to MC events. The up/down asymmetry of the energy scale in the detector effects the visible energy of upward-going events relative to down-ward going ones and is estimated to be 0.6%(0.6%). Finally, the effect of the energy scale on the 1.6 GeV/c momentum cut used in the reconstruction of stopping muon events induces another source of uncertainty for that sample only and is taken as a 1.1%(1.1%) systematic.

8.6 Analysis Binning

The analysis bins have been chosen to optimize two conditions, the sensitivity to θ_{13} and the robustness of the χ^2 in Equation 8.6. Due to the nature of the resonant enhancement in the $\nu_\mu \rightarrow \nu_e$ transition probability, it is advantageous to select binning narrow enough to be sensitive to the effect. However, for an increasingly fine binning scheme, the number of expected events from the MC decreases accordingly and the

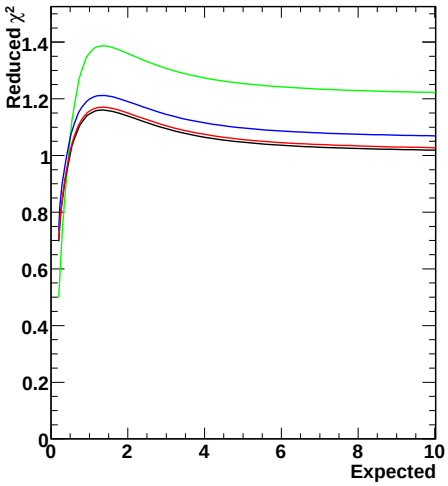

Figure 8.4: Average contribution to the reduced χ^2 for the χ^2 defined in Equation 8.6 as a function of the expected number of events in a bin. Incomplete estimation of the expected number of events for various amounts of MC is also shown. MC factors of 5× (green), 20× (blue) , 100× (red) and no error (black) are shown. The SK-I and SK-II MC have both been generated at 20 times their respective accumulated livetimes and are described by the blue line.

contribution to the χ^2 can become artificially large if the error on the expectation is sufficiently large. That is, the formulation of χ^2 may not be χ^2-distributed for very low bin populations.

If the true number of expected events in a bin is assumed to be μ_T for an amount of livetime l, the number of expected events μ_M in a MC with livetime αl will be $\alpha\mu_T$. In practice, however, μ_T is unknown and due to the finite nature of the MC itself, the number of events generated in the bin will be Poisson distributed about $\alpha\mu_T$. For a given value, n, from this distribution the best estimate of μ_T is therefore n/α. Computing the average contribution to the reduced χ^2 is thus an average over the possible values of n and all possible observations, i, from the Poisson distribution about μ_T,

$$h(\mu_T) = \sum_{i=0}^{\infty} \lambda(i, \mu_T) \sum_{n=0}^{\infty} \lambda(n, \alpha\mu_T)\chi^2(i, \frac{n}{\alpha}). \tag{8.12}$$

Here $\chi^2(\mathcal{O}, E)$ is as in Equation 8.4 and $\lambda(n, \mu)$ is the probability of observing n events

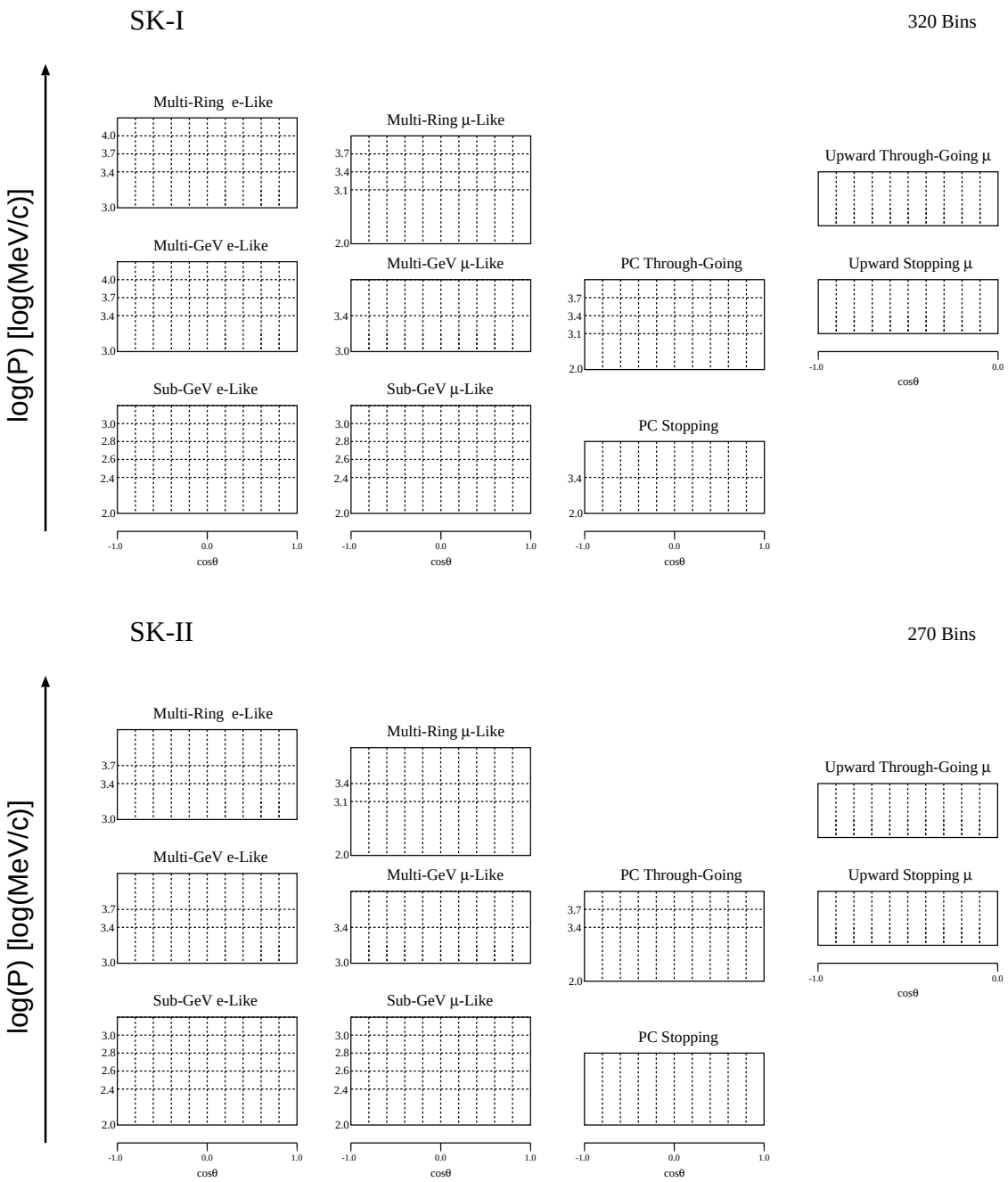

Figure 8.5: Binning for SK-I (top) and SK-II (bottom) for each of the ten samples used in the analysis. SK-I has a total of 320 bins and SK-II has 270.

from a Poisson distribution of mean μ. Figure 8.4 this average reduced χ^2 for varying amounts of uncertainty in the expected number of events arising from the MC.

At present, the SK-I and SK-II MC have been generated with 20 times the livetime of their respective data and are therefore subject to the behavior of the blue line. For less than three expected events, the contribution to the χ^2 is considerably greater than one. Around five expected events the curve begins to flatten appreciably and continues smoothly with an increasing number of expected events. Therefore, to avoid the feature at low expectation, analysis binning has been chosen such that there are ≥ 6 expected events in each bin. Since the livetimes between SK-I and SK-II differ they similarly have different binning.

The resulting bin scheme is summarized in Figure 8.5. Based on the MC the expected sensitivity to each of the oscillation parameters can be computed using this binning. Choosing a point in the oscillation space the MC is binned and oscillated. The result is then treated as the observed data and the MC is then re-oscillated at all of the points in the oscillation space and fit against the presumed observation. Contours are then drawn as they are normally made in the full analysis (see below). Sensitivity contours at 90 % C.L. from the SK-I and SK-II MC are shown in Figure 8.6. Note that in all of the variables SK-II is less sensitive than SK-I. The sensitivities have been generated at different values of Δm^2 for SK-I and SK-II and results in their relative displacement.

8.7 Results

8.7.1 Normal Hierarchy

The results of the fit to the SK-I, SK-II and SK-I+SK-II data sets appear in Figures 8.7 and 8.8 and the numerical details are summarized in Table 8.2. Each figure shows the 90% and 99% confidence level contours for each pairwise combination of the three parameters considered. The remaining parameter has been minimized over, meaning that instead of taking the contour as the $\Delta\chi^2$ projection in the two variables of interest

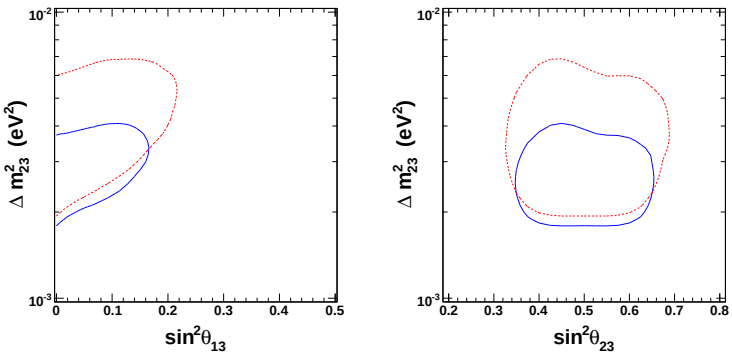

Figure 8.6: Sensitivity contours for SK-I (blue) and SK-II (red-dashed) at 90% confidence level for the normal hierarchy. The sensitivity has been computed at different values of the atmospheric mass splitting and results in the displacement between the two contours. SK-I has been generated at $\Delta m^2 = 2.5 \times 10^{-3}$ eV^2 and SK-II at 3.2×10^{-3} eV^2. Both have been generated at $(\sin^2\theta_{13}, \sin^2\theta_{23}) = (0.0, 0.5)$.

at the best fit point of the third, the projection is made along a path on the three-dimensional $\Delta\chi^2$ surface. The path is taken at the minimum value on the surface in the direction of the third parameter for each fixed pair of the other two parameters. The $\Delta\chi^2$ surface is constructed as $\Delta\chi^2 \equiv \chi^2 - \chi^2_{\text{min}}$, where χ^2_{min} is the χ^2 at the best fit in the parameter space. A cut is made on the $\Delta\chi^2$ to describe the confidence levels as specified by the coverage probability for simultaneously estimating two parameters [50]. The 90% C.L. satisfies $\Delta\chi^2 \leq 4.61$ and the 99% C.L. satisfies $\Delta\chi^2 \leq 9.2$.

For SK-I the fit results in the atmospheric variables can be compared against the two-flavor analysis presented in Ref. [33]. Notably, the best fit point (see Table 8.2) is consistent with the 90% C.L. in the reference. At $\theta_{13} = 0$ the three-flavor oscillation probabilities are equivalent to the two-flavor case in the present scheme so this consistency is a good cross-check of the current analysis. Further, the extent of the Δm^2 contour is consistent though slightly improved over Ref. [33]. The improvement stems primarily from the finer binning scheme used in the present analysis. Finally, consistency between the two schemes suggests that the current analysis framework is robust and can suitably be applied to the SK-II and SK-I+SK-II data sets.

The SK-II results can best be categorized by their larger atmospheric parameters contours relative to SK-I. This is consistent with the factor of almost two difference

Table 8.2: Summary table of the results of the fits to the SK-I, SK-II and SK-I+SK-II data under the assumption of a normal mass hierarchy.

Normal Hierarchy	SK-I	SK-II	SK-I+SK-II
χ^2_{min}	317.4	289.6	602.7
D.O.F	318	268	587
$\sin^2\theta_{13}$	0.0	0.0	0.0
90% C.L.	≤ 0.12	≤ 0.10	≤ 0.03
$\sin^2\theta_{23}$	0.5	0.5	0.5
90% C.L.	[0.40, 0.63]	[0.35, 0.65]	[0.40, 0.60]
Δm^2 [eV^2]	2.5×10^{-3}	2.8×10^{-3}	2.6×10^{-3}
90% C.L. $\times 10^{-3}$	[0.18, 0.30]	[0.17, 0.42]	[0.21, 0.30]

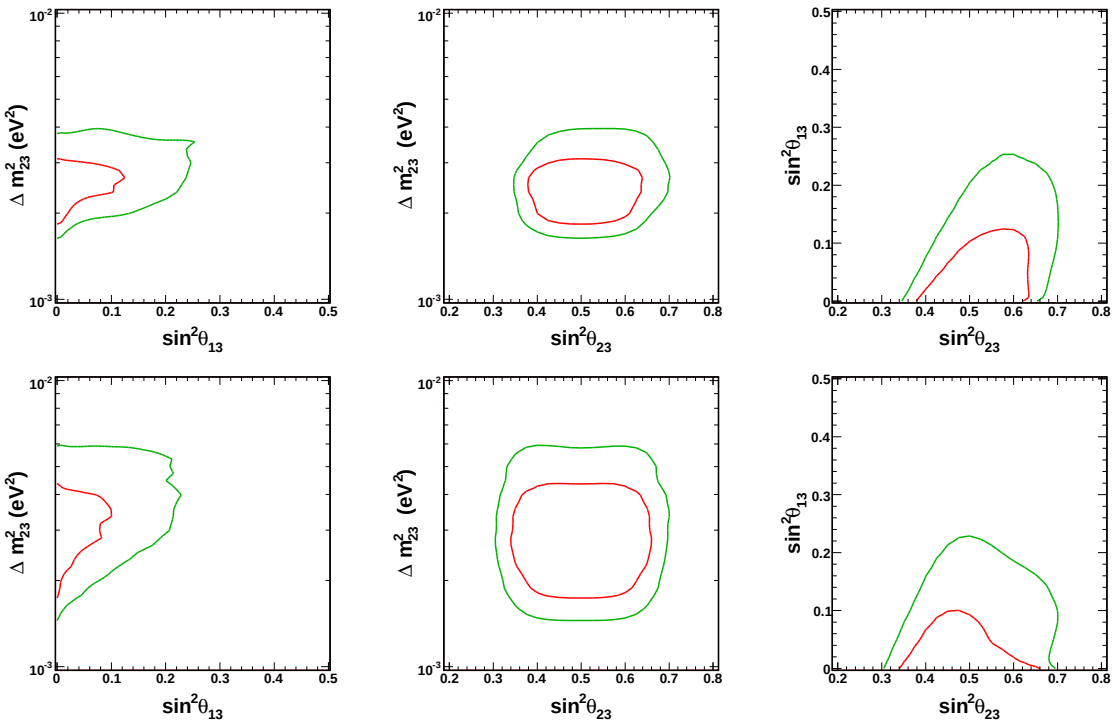

Figure 8.7: The 90% (red) and 99% (green) confidence level contours for the SK-I (top) and SK-II (bottom) data sets for the three combinations of variables fit during the normal hierarchy analysis. In each plot the third variable has been minimized over when drawing the contours. The best fit is at $(\Delta m^2_{23}, \sin^2\theta_{23}, \sin^2\theta_{13}) = (2.5 \times 10^{-3}\ \text{eV}^2, 0.5, 0.0)$ in SK-I and $(2.8 \times 10^{-3}\ \text{eV}^2, 0.5, 0.0)$ in SK-II.

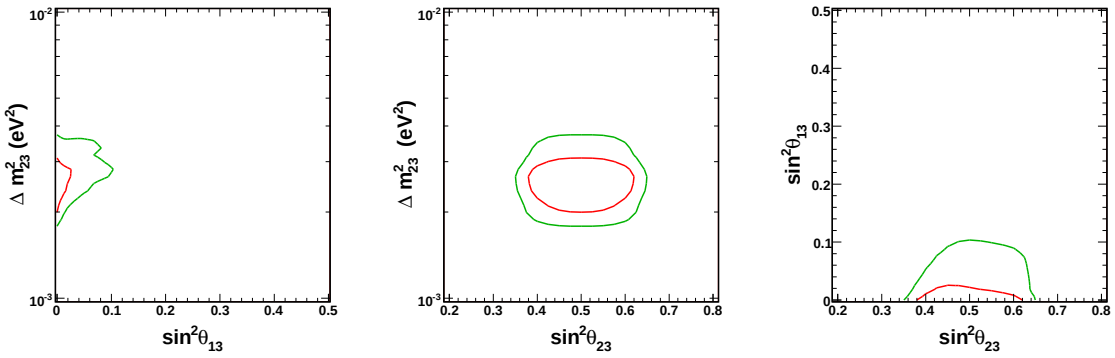

Figure 8.8: The 90% (red) and 99% (green) confidence level contours for the combined SK-I+SK-II data set for the three combinations of variables fit during the normal hierarchy analysis. In each plot the third variable has been minimized over when drawing the contours. The best fit is at $(\Delta m^2_{23}, \sin^2\theta_{23}, \sin^2\theta_{13}) = (2.6 \times 10^{-3}\ \mathrm{eV}^2, 0.5, 0.0)$.

in livetime between the two data sets and the decreased resolution of SK-II. In terms of the sensitivity shown in Figure 8.6 the data contours are slightly smaller in all of the parameters. Though the contours among all the variables overlap with the SK-I result the best fit for SK-II is at a slightly higher value, 2.8×10^3 eV^2 compared to 2.5×10^3 eV^2, and displaces the contours. However, the SK-I value is consistent with the SK-II contour, and the broad shape of the $\Delta\chi^2$ distribution of Δm^2 shown in Figure 8.9 indicates that there is almost no difference between the two models from the perspective of the SK-II data. Finally, the extent of the $\sin^2\theta_{13}$ contours is less than that of SK-I, a point which is discussed more below.

Adding SK-II to SK-I gives atmospheric contours that are slightly smaller than SK-I alone. Since the SK-II contour is so much larger in these variables this is not too surprising. Further, the best fit in these variables is consistent with the result from the two-flavor analysis in Ref. [33]. On the other hand the SK-I+SK-II data set provides a considerable improvement in $\sin^2\theta_{13}$ over SK-I alone. Interestingly, the 90% confidence level is more restrictive than the CHOOZ [42] result. Further discussion of this variable is postponed until Section 8.7.3.

Fitted values of the systematic error parameters, ϵ_i, for each of the data sets are listed in Tables 8.4, 8.5 and 8.6.

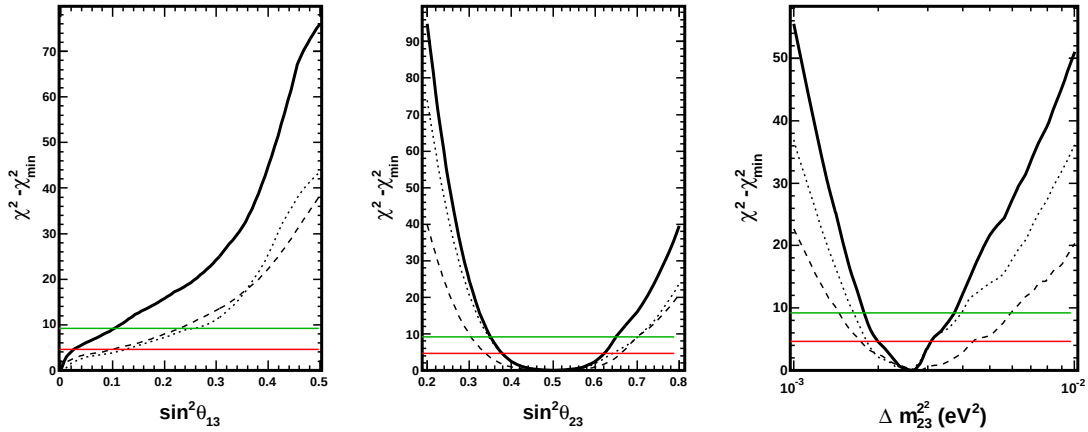

Figure 8.9: The $\Delta\chi^2 = \chi^2 - \chi^2_{\text{min}}$ distributions minimized over over the appropriate variables for each of Δm^2_{23}, $\sin^2\theta_{23}$ and $\sin^2\theta_{13}$ in the normal hierarchy. The SK-I+SK-II distribution appears as the solid line, SK-I alone is the dotted line, and SK-II is the dashed line. The 90% and 99% confidence level cuts are shown as the red and green horizontal lines, respectively.

8.7.2 Inverted Hierarchy

Similar results for fits to the inverted hierarchy hypothesis appear in Figures 8.10 and 8.11 and the fit information is summarized in Table 8.3. At a glance the best fit points among all of the data sets are similar in the normal and inverted hierarchies. Moreover, except for SK-I the best fit points are all at $\sin^2\theta_{13} = 0$, a model which is equivalent to two-flavor oscillations. In this mode there is no $\nu_\mu \rightarrow \nu_e$ transition driven by matter effects. Therefore the MC oscillated at this point is the same between the normal and inverted hierarchies and explains the equivalence of the respective χ^2 minima. SK-I in the inverted hierarchy, though, is fit to a value of $\sin^2\theta_{13}$ marginally different from 0, and to the same atmospheric variables so the small difference between its minimum χ^2 values is expected.

In each of the fits the resulting contours are larger than their normal hierarchy counterparts. The decrease in sensitivity arises from two sources. Under the inverted hierarchy anti-neutrinos are subject to the MSW resonance while neutrinos remain unaffected. However, due to the roughly factor of two reduction in the anti-neutrino interaction cross section relative to the neutrino cross section, there is a corresponding

Table 8.3: Summary table of the results of the fits to the SK-I, SK-II and SK-I+SK-II data under the assumption of at inverted mass hierarchy.

Inverted Hierarchy	SK-I	SK-II	SK-I + SK-II
χ^2_{min}	317.2	289.6	602.7
D.O.F	318	268	587
$\sin^2\theta_{13}$	0.006	0.0	0.0
90% C.L.	≤ 0.27	≤ 0.15	≤ 0.12
$\sin^2\theta_{23}$	0.5	0.5	0.5
90% C.L.	[0.40, 0.68]	[0.35, 0.65]	[0.40, 0.63]
Δm^2 [eV^2]	2.51×10^{-3}	2.8×10^{-3}	2.6×10^{-3}
90% C.L. $\times 10^{-3}$	[0.18, 0.35]	[0.17, 0.42]	[0.20, 0.30]

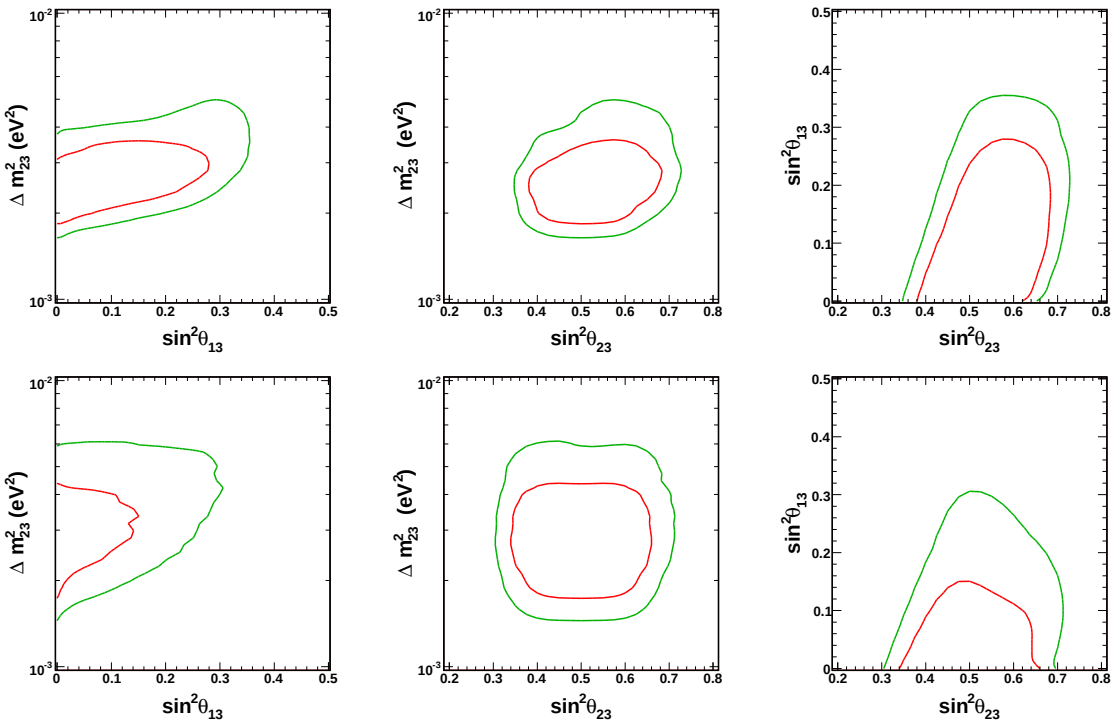

Figure 8.10: The 90% (red) and 99% (green) confidence level contours for the SK-I (top) and SK-II (bottom) data sets for the three combinations of variables fit during the inverted hierarchy analysis. In each plot the third variable has been marginalized when drawing the contours. The best fit is at $(\Delta m^2_{23}, \sin^2\theta_{23}, \sin^2\theta_{13}) = (2.5 \times 10^{-3}\ \text{eV}^2, 0.5, 0.0)$ for SK-I and $(2.8 \times 10^{-3}\ \text{eV}^2, 0.5, 0.0)$ for SK-II.

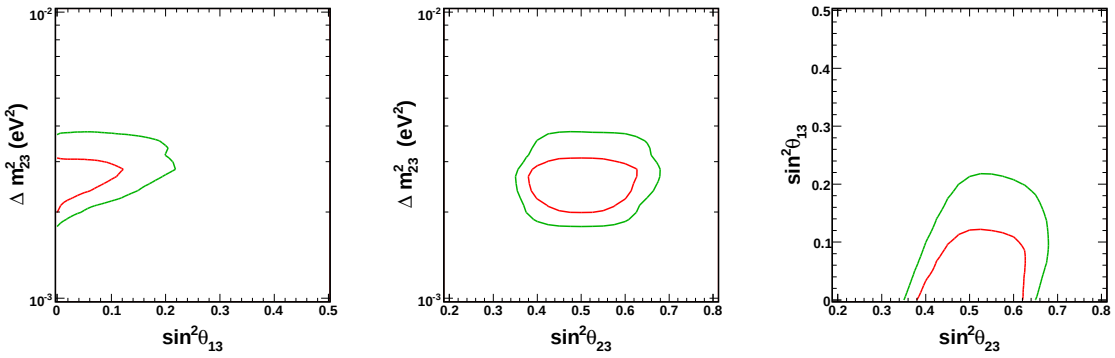

Figure 8.11: The 90% (red) and 99% (green) confidence level contours for the combined SK-I+SK-II data set for the three combinations of variables fit during the inverted hierarchy analysis. In each plot the third variable has been marginalized when drawing the contours. The best fit is at $(\Delta m^2_{23}, \sin^2\theta_{23}, \sin^2\theta_{13}) = (2.6 \times 10^{-3}\ \mathrm{eV}^2, 0.5, 0.0)$.

reduction of anti-neutrino events in the data sets. Accordingly, a larger θ_{13} is required to produce an observable excess of anti-neutrino events relative to the normal hierarchy. These ideas are represented here in the the data and are consistent with the MC studies presented in Section 7.5. This in conjunction with the equivalence of the χ^2 at the best fit points suggests that the data are consistent with both the normal and inverted hierarchies.

8.7.3 θ_{13} in the Normal Hierarchy

Under the assumption of the normal mass hierarchy the combination of SK-I and SK-II data sets provides a strong constraint on the value of $\sin^2\theta_{13}$. The 90% C.L. constraint is more restrictive than the CHOOZ limit. Figure 8.13 shows the fits to this variable for the three data sets overlaid on the CHOOZ exclusion region. Both SK-I and SK-II have 90% C.L. contours that are comfortably overlapping with the CHOOZ result. The SK-I+SK-II data set, however, is completely outside of the exclusion at 90% confidence. Note that this contour is considerably smaller than the expected sensitivity shown in the left panel of Figure 8.16.

To address the question of why the contour is so unexpectedly small it is beneficial

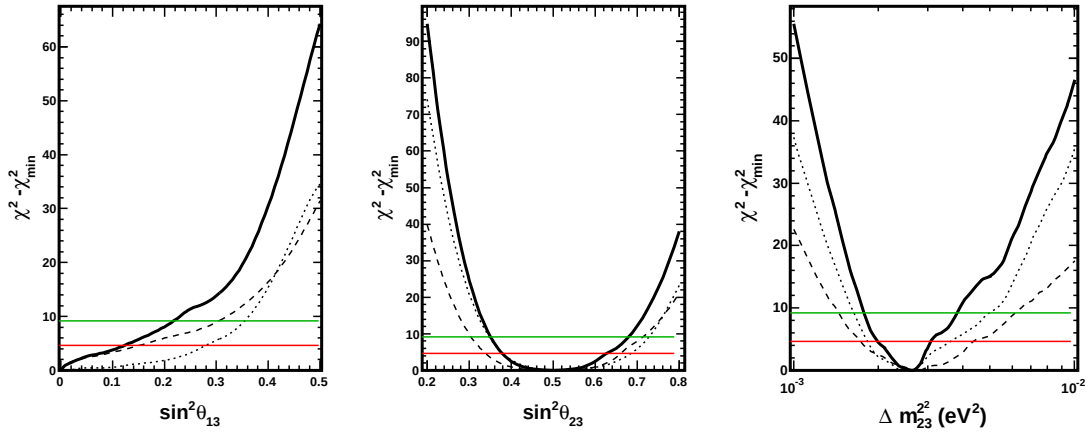

Figure 8.12: The $\Delta\chi^2 = \chi^2 - \chi^2_{\text{min}}$ distributions for each of the fit variables $\Delta m^2_{23}, \sin^2\theta_{23}, \sin^2\theta_{13}$ in the inverted hierarchy. The SK-I+SK-II distribution appears as the solid line, SK-I alone is the dotted line, and SK-II is the dashed line. The 90% and 99% confidence level cuts are shown as the red and green horizontal lines, respectively.

to view the plots in Figures 8.14 and 8.15. The former shows the up-down asymmetry of the multi-ring e-like sample in terms of the data, the MC at the best fit point and at the same point but with θ_{13} at the CHOOZ limit. The latter shows the same information for the single-ring multi-GeV e-like sample. In the multi-ring plots, although the SK-II data shows some excess consistent with larger θ_{13} the size of the error bars suggest it is not statistically significant. A similar excess with large errors is also present in a few bins of the single-ring plots and so the combination of the two effects explains why the SK-II fit by itself is slightly smaller than the SK-I result (see Figure 8.7). However, it is not sufficient to explain the large change in the contour seen with the SK-I+SK-II data.

Without a statistically significant excess of events consistent with non-zero θ_{13} the smallness of the combined contour is thought to be a well distributed effect in the data. Under this assumption it is necessary to determine how likely it is to observe a contour of similar extent. To this end, toy MC data sets were generated at the SK-I+SK-II data's best fit point. Instead of using the data, oscillated MC at this point is statistically fluctuated 500 times and fit against the rest of the models in

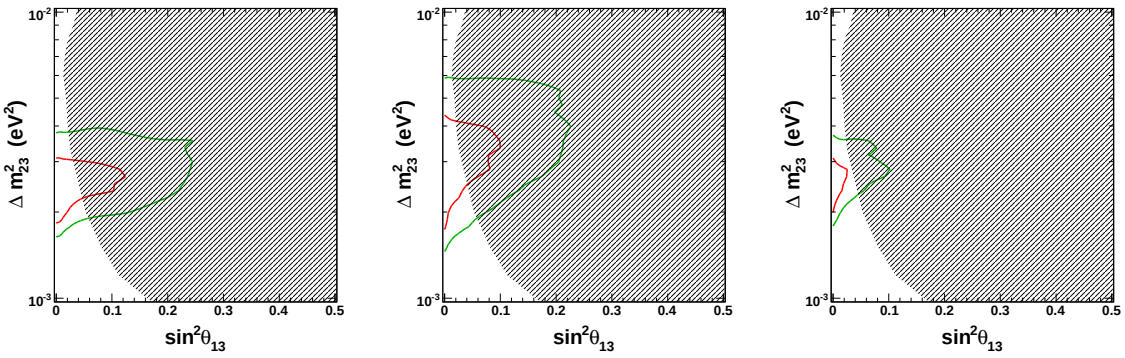

Figure 8.13: Results of the fit to $\sin^2\theta_{13}$ for (from left to right) SK-I, SK-II and the SK-I+SK-II data set with the CHOOZ 90% exclusion region (shaded). The exclusion result has been taken from [42].

the parameter space. The effect is to simulate 500 experiments under the assumption that the data is indeed drawn from the distribution specified by the best fit oscillation model. After fitting, the extent of the $\sin^2\theta_{13}$ contours can be compared against the data.

Figure 8.16 shows the distribution of the maximum end-point of the 90% C.L. $\sin^2\theta_{13}$ contour for these simulated experiments. The red line shows the location of the data's contour in the distribution and the blue line indicates that of the expected sensitivity. Of the 500 experiments, 98 were fit at or below the data's extent. In comparison, the sensitivity contour represented the lower 57% of the experiments. Since these numbers are not appreciably close to zero, the SK-I+SK-II data's result is sufficiently likely. Accordingly, though the data's contour is more restrictive than the CHOOZ limit, based on the MC studies above it is consistent with statistical fluctuations and occurs 20% of the time.

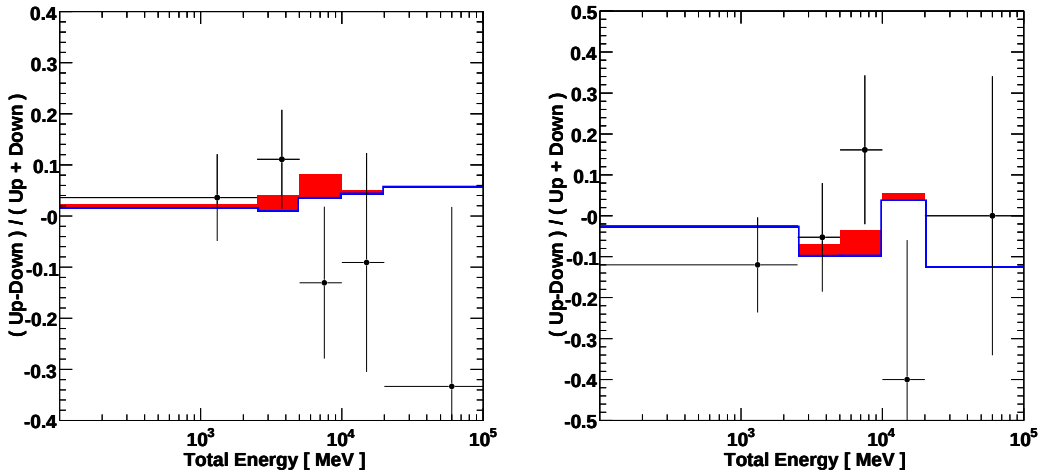

Figure 8.14: The up-down asymmetry of the SK-I (left) and SK-II (right) multi-GeV multi-ring e-like samples as a function of total energy. Note that the vertical axes between the two plots differ. The black dots represent the data while the blue line is the MC prediction at the best fit point. The red bars denote the excess expected at the best fit with θ_{13} at the CHOOZ limit.

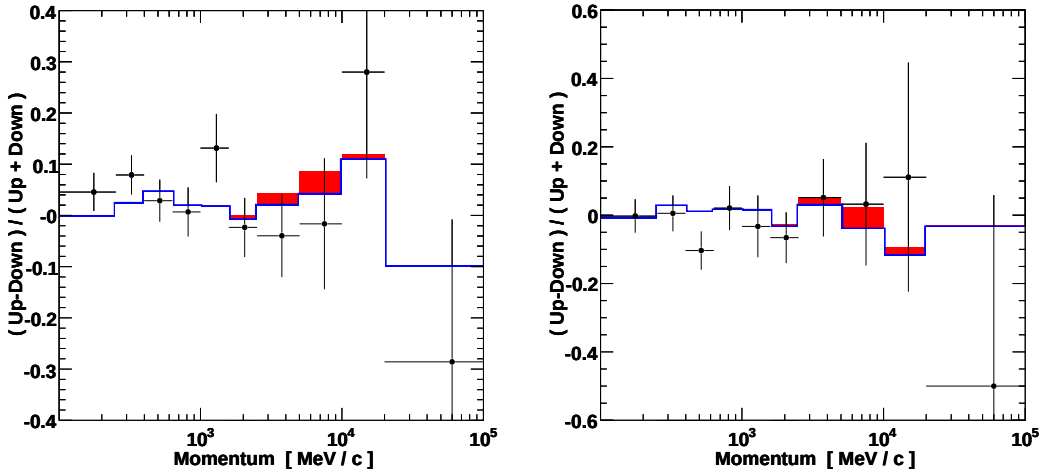

Figure 8.15: As in Figure 8.14 for the single ring e-like sample.

Table 8.4: Fitted systematic error parameters for systematics common among the data sets. The columns show ϵ/σ at the best fit.

Flux Errors	SK-I	SK-II	SK-I + SK-II
Absolute Normalization	-0.83	-0.47	-0.94
ν_μ/ν_e $E_\nu < 5$ GeV	0.56	0.61	0.82
ν_μ/ν_e $E_\nu > 5$ GeV	0.37	0.3	0.49
$\nu_e/\bar{\nu}_e$ $E_\nu < 5$ GeV	-0.089	-0.096	-0.16
$\nu_e/\bar{\nu}_e$ $E_\nu > 5$ GeV	-0.23	-0.16	-0.27
$\nu_\mu/\bar{\nu}_\mu$ $E_\nu < 5$ GeV	0.33	0.47	0.56
$\nu_\mu/\bar{\nu}_\mu$ $E_\nu > 5$ GeV	0.39	-0.46	0.044
Up/down	0.15	0.22	0.28
Horizontal/vertical	-0.29	-0.14	-0.41
K/π	0.1	0.0048	0.12
Neutrino production height	1	0.73	0.97
Cosmic ray energy spectrum	-1.2	-1.1	-1.3
FC multi-GeV norm.	-1.1	-1	-1.4
PC + upward-stopping norm.	0.25	0.05	0.3
ν Interaction Errors			
M_A, axial mass	-1.2	0.085	-0.9
QE (model)	0.92	0.66	0.98
QE (cross-section)	-0.5	-0.25	-0.46
Single-π cross-section	1.1	1.5	1.2
Multi-π (model)	-0.21	-0.22	-0.26
Multi-π (cross-section)	-0.061	0.1	-0.007
Coherent-π cross section	-0.17	-0.34	-0.49
NC/CC	-0.33	0.48	-0.05
Nuclear Effect in ^{16}O	-0.39	-0.037	-0.31
CC ν_τ cross-section	-0.22	-0.17	-0.31
π energy spectrum	-0.0059	0.0	-0.028
FC NC Background	0.47	0.57	0.46

Table 8.5: Summary of the fitted systematic error parameters that are specific to SK-I, for SK-I and the Combined data under the normal mass hierarchy. The columns show ϵ/σ for each of the errors.

Reduction Errors	SK-I	SK-I + SK-II
FC reduction	0.0042	0.24
PC reduction	-0.16	-0.04
Upward-going muon Reduction	-0.32	-0.41
FC/PC separation	0.11	0.042
non-ν e-like Background	-0.13	-0.13
non-ν μ-like Background	-0.13	-0.12
Upward stopping/through-going	0.43	0.36
Reconstruction Errors		
Ring separation	-0.2	-0.17
Single-ring PID	-0.53	-0.26
Multi-ring PID	-0.35	-0.27
Energy calibration	-0.24	-0.17
1.6 GeV muon cut	-0.065	-0.013
Energy calibration Up/Down	-0.082	-0.096
Upward-through going background	0.13	0.22
Upward-stopping background	-0.042	-0.048
Multi-GeV single-ring e-like BG	-0.15	-0.14
Multi-ring e-like BG	-0.01	-0.0076
Multi-ring e-like normalization	0.41	0.41
PC stop/through-going separation	0.26	-0.017
Solar Activity	0.011	0.03

Table 8.6: Summary of the fitted systematic error parameters that are specific to SK-II, for SK-II and the Combined data under the normal mass hierarchy. The columns show ϵ/σ for each of the errors.

Reduction Errors	SK-II	SK-I + SK-II
FC reduction	-0.93	-0.94
PC reduction	0.18	-0.022
Upward-going muon Reduction	0.09	0.14
FC/PC separation	0.031	0.03
non-ν e-like Background	-0.094	-0.063
non-ν μ-like Background	-0.011	0.017
Upward stopping/through-going	0.14	0.17
Reconstruction Errors		
Ring separation	-0.17	-0.11
Single-ring PID	0.55	0.35
Multi-ring PID	-0.71	-0.87
Energy calibration	0.028	0.026
1.6 GeV muon cut	-0.37	-0.4
Energy calibration Up/Down	0.53	0.41
Upward-through going background	-0.68	-0.73
Upward-stopping background	0.07	0.093
Multi-GeV single-ring e-like BG	0.061	0.057
Multi-ring e-like BG	0.0066	0.0045
Multi-ring e-like normalization	1.3	1.3
PC stop/through-going separation	0.48	0.76
Solar Activity	0.01	0.01

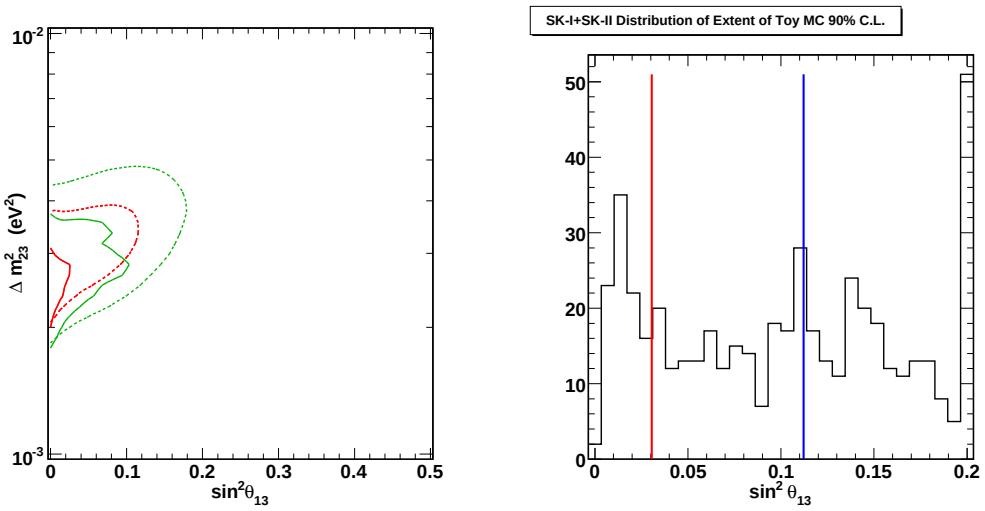

Figure 8.16: The fitted contours (solid) overlaid with the expected sensitivity (dashed) generated at the best fit point for the SK-I+SK-II data set appears in the left panel. Red lines indicate the 90% C.L. and the 99% C.L. appears in green. In the right hand panel, the distribution of the upper limit of the 90% C.L. on the measurement of $\sin^2\theta_{13}$ for 500 toy MC data sets generated at the data's best fit point. Nearly 20% of the toy data sets fell at or below that of the data (red line) and 57% fell below the expected sensitivity (blue line). The last bin is the integrated contents of $\sin^2\theta_{13} \geq 0.20$.

Chapter 9

Conclusion

Super-Kamiokande has collected more than 18,000 atmospheric neutrino events over the combined 1489 day SK-I and 803 day SK-II running periods. The SK-I data has already been used to provide strong evidence for two-flavor $\nu_\mu \leftrightarrow \nu_\mu$ oscillations at $\sin^2 2\theta = 1.0$ and $\Delta m^2 = 2.4 \times 10^{-3}\mathrm{eV}^2$ [34, 33]. These oscillations have a marked zenith angle dependence and to leading order there are no oscillation effects seen in the e-like samples.

The analysis presented in this dissertation searches for the appearance of ν_e events at high energy as a signature of sub-leading oscillations in the atmospheric data driven by non-zero θ_{13}. Further, θ_{13}-induced resonant enhancement of the three-flavor $\nu_\mu \rightarrow \nu_e$ transition probability in the Earth's matter has been studied to explore the question of the neutrino mass hierarchy. Fits have been performed using a χ^2 analysis with "pulled" systematic errors to the SK-I, SK-II and their combination under both the normal and inverted hierarchies. Each result remains consistent with the previous Super-K analyses and the present knowledge of the atmospheric mixing parameters. The best fit to the SK-I+SK-II data set is $(\Delta m^2, \sin^2\theta_{23}, \sin^2\theta_{13}) = (2.6 \times 10^{-3}\mathrm{eV}^2, 0.5, 0.0)$ for both hierarchies with $\chi^2_{min} = 602.7$ for 587 degrees of freedom.

The SK-I and SK-II data sets are both consistent with the CHOOZ experiment's limit on θ_{13} in both hierarchies as is the inverted hierarchy fit to the SK-I+SK-II data. Under the normal hierarchy the this data set's 90% C.L., however, is slightly more

restrictive than the current best limit and below its expected sensitivity. Since there is not a significant excess of ν_e events in the data and because similar contours appear in $\sim 20\%$ of toy MC samples, the data is consistent with statistical fluctuations. With the current data, this analysis is not capable of differentiating between the normal and inverted neutrino mass hierarchies.

Super-Kamiokande is currently taking data as SK-III after detector upgrades in 2006. Recent improvements to the Super-K reconstruction algorithms and the detector MC will offer a better understanding of the current atmospheric neutrino data. Further, as data accumulates, so too does the possibility of improved measurements of the oscillation parameters.

Appendix A

Oscillation Software

The analysis performed in this dissertation is an extension of a search for non-zero θ_{13} presented in ref [44]. To extend and improve existing features of the search, the analysis has been modernized and rewritten in C++ to utilize object oriented programming techniques. Further, since oscillation analyses at Super-K have many common aspects, the code was written as to provide a generalized analysis package allowing for more modular program design. A description of the concept of the software and how it is applied to perform the oscillation analysis in this dissertation is presented below. The software maybe obtained from the Super-K CVS repository under `analysis/Osc3++`.

A.1 Generic Oscillation Analyses

The oscillation analyses at Super-K, and other analyses for that matter, have several features in common. First, the analysis chain is nearly identical. Given a set of data and a corresponding MC, the MC is oscillated at every point in the oscillation space and fit against the data. Acceptance regions are then drawn around all points in the oscillation space that differ from the best fit point in their χ^2 value by less than some threshold. In principal, the differences in the analyses amount mostly to the type and number of bins, the number of points in the oscillation space and the type of oscillations. However, from the point of view of performing a fit to the data the software doesn't need to know these particulars. Instead, a listing of bins in no particular order, filled with data and the MC to be tested is the minimum amount of necessary information. The meaning, or edges of the bins are secondary concerns and

can be abstracted away. This abstraction is at the heart of the software used in this analysis.

A.2 Design Strategy

The analysis software has been written with the GEANT4 [96] framework in mind. That is, its backbone is a set of global parent classes that in principal can run nearly independently, requiring only minimal input from the user. However, in order to make the analysis more productive the user is responsible for deriving child classes from these parents which specify particular actions. Since inherited objects retain the characteristics of their parent, generic calls to parent functions in the backbone of the software exist in their children classes but may be overridden. By demanding sufficient generality in the arguments of the parent routines there is no need to define analysis specific functions in the backbone code. The parent module responsible for oscillating an event, for instance, is generically termed `Oscillator` and its default action is to return a two-flavor oscillation probability at the best fit point of ref [33]. However, the analysis in this thesis derives an object `ThreeFlavorOscillator` from this class, which overrides the default method to return a full three-flavor probability. Several objects in the software follow this scheme.

GEANT has provided one other major source of inspiration for the development of the analysis code, the use of input cards. Since certain parameters change while studying an analysis, the number of oscillation points to consider or the amount of averaging to apply (see section 8.2.2), for instance, these otherwise hard-coded parameters have been moved to card based inputs. Not only does this eliminate the need to recompile when testing new parameters but it also provides a possible record of the parameters used for executions of the software.

A.3 Code Layout

There are two main pieces to the analysis: oscillation of the MC and fitting the MC against the observed data. The ensemble of code that performs these tasks is managed by a central object, the `profiler`. `Profiler` manages information that is more specific to the analysis and is registered by the user. By using an inherited class `ThreeFlavorProfiler`, the user registers, for instance, the number, range and step size for the oscillation parameters. The `profiler` automatically generates a `ProfileSpace` object for each of the requisite oscillation points. The binning scheme is also maintained in this manner.

After registering, the `profiler` then brokers the exchange of information between other objects in the software. When the data and MC are being binned, for instance, objects provide `profiler` with an event's kinematic variables and are returned the bin into which the event should be filled. In this way it is not necessary to pass and store indexing information among other classes. The `profiler` is instantiated in the main program loop and passed to the objects that interface with it at their creation.

Events are passed to the analysis software through an `Event` object. This structure is registered with `profiler` and used by an `EventParser` object to pass information from a ROOT tree to the analysis. The tree should be prepared before hand and for the analysis in this dissertation represents the final reconstructed and reduced atmospheric neutrino data and MC. During the analysis sequence a loop is performed over this tree and the `Event` object is overwritten at each iteration. A particular event's information is disseminated to other parts of the software via the interactions of `EventParser` and `profiler`.

Binning in the analysis is handled by `bin` objects and each bin in the analysis is an instantiation of this class. A `bin` object maintains a variable representing the data content and an array of MC content (one index for each point in the oscillation space), but its dimensions are kept separate. Instead it is assigned a unique label at its instantiation that is maintained by the `profiler`. Bin creation is handled by a container class, `BinContainer`, which interacts with `profiler` to produce the

registered number of `bins`.

The oscillation of the MC is performed by the parent class `OscMaestro`. Generically this class holds a `BinContainer`, a pointer to an `Oscillator` and one to a `profiler`. `OscMaestro` is provided events from the data and MC externally and by interacting with these objects manipulates the bin contents. Fitting the output of these oscillations is done with a `FitMaestro` that houses the same objects and additionally an instance of the `ChiSquared` class. By inheriting from these "maestro" classes the user is able to maintain control over specific parts of the program flow.

Fitting is the most generic aspect of the analysis. The `ChiSquared` object performs the fit and maintains pointers to a `profiler` and a `BinContainer`. If the user has registered bins with `profiler` that should not be included during a fit to a subset of the data `ChiSquared` has access to this information. However, the parent `profiler` is sufficiently general that a `ChiSquared` object can function without a user having registered any detailed information. `ChiSquared` can then use a simple text file containing the data and MC to be compared. In this way fits to data from non-oscillation analyses can be performed readily.

A.4 Summary

The `Osc3++` code suite is designed for optimal flexibility. Based on this flexibility it has been used at Super-K for other non-oscillation analyses. The analysis output is written in ROOT files and is independent in large part from Super-K specific libraries. For this reason the code is portable and continually evolving. More details are available in the documentation of the software in the Super-K CVS repository.

REFERENCES

[1] T. Schwetz, Plenary talk at NuFact07, Okayama Japan, CERN-PH-TH-207 , hep-ph/07105027.

[2] W. Pauli, *Open Letter to Radioactive Ladies and Gentlemen* (1930), Physics Today **31**, 27 (1978).

[3] E. Fermi, Z. Phys. **88**, 161 (1934).

[4] B. Pontecorvo, Chalk River Laboratory Report PD-205 (1946), unpublished.

[5] F. Reines and C. Cowan, Nature **178**, 446 (1953).

[6] F. Reines and C. Cowan, Phys. Rev. **92**, 830 (1953).

[7] G. D. *et. al*, Phys. Rev. Lett. **9**, 36 (1962).

[8] K. K. *et. al*, Phys. Lett. B **504**, 218 (2001).

[9] L. Collaborations and the LEP Electroweak Working Group, *XX International Symposium on Lepton and Photon Interatcitons at High Energy*, Rome, Italy (2001).

[10] M. Honda *et. al*, Phys. Rev. **D75**, 043006 (2007).

[11] Ch. Kraus *et. al*, Euro. Phys. J. **C40**, 447 (2005).

[12] K.A. Assamagan *et. al*, Phys. Rev. **D53**, 6065 (1996).

[13] R. Barate *et. al*, Euro. Phys. J. **C2**, 395 (1998).

[14] V. Barger *et. al*, Phys. Lett. **B595**, 55 (2004).

[15] C. Arnaboldi *et. al*, *hep-ex/08023439*.

[16] B. Cleveland *et. al*, ApJ **496**, 505 (1998).

[17] R. Davis, Harmer, and K. Hoffman, Phys. Rev. Lett. **21**, 1205 (1968).

[18] A.I. Abazov *et. al*, Phys. Rev. Lett. **67**, 3332 (1991).

[19] D.N. Abdurashitov *et. al*, Phys. Rev. Lett. **77**, 4708 (1996).

[20] P. Anselmann *et. al*, Phys. Lett. **B235**, 376 (1992).

[21] W. Hampel *et. al*, Phys. Lett. **B388**, 384 (1996).

[22] Y. Fukuda *et. al*, Phys. Rev. Lett. **77**, 1683 (1996).

[23] J. Hosaka *et. al*, Phys. Rev. **D73**, 112001 (2006).

[24] Bahcall and Serenelli and Basu, ApJ **621**, L85 (2005).

[25] B. Aharmim *et. al*, Phys. Rev. **C72**, 055502 (2005).

[26] T. Araki *et. al*, Phys. Rev. Lett. **94**, 081801 (2005).

[27] K.S. Hirata *et. al*, Phys. Lett. **B280**, 146 (1992).

[28] D. Casper *et. al*, Phys. Lett. **B66**, 2561 (1991).

[29] W.W.M. Allison *et. al*, Phys. Lett. **B391**, 491 (1997).

[30] M. Sanchez *et. al*, Phys. Lett. **B566**, 35 (2003).

[31] Y. Fukuda *et. al*, Phys. Lett. **B335**, 237 (1994).

[32] G. Giacomelli *et. al*, Phys. Atom. Nucl. **67**, 1139 (2004).

[33] Y. Ashie *et. al*, Phys. Rev. **D71**, 112005 (2005).

[34] Y. Ashie *et. al*, Phys. Rev. Lett. **93**, 101801 (2004).

[35] P. Adamson *et. al*, in submission to Phys. Rev. D (*hep-ex/0711.0769*).

[36] M.H. Ahn *et. al*, Phys. Rev. **D74**, 072003 (2006).

[37] A. Aguilar *et. al*, Phys. Rev. **D64**, 112007 (2001).

[38] B. Armbruster *et. al*, Phys. Rev. **D65**, 112001 (2002).

[39] E. Church *et. al*, Phys. Rev. **D66**, 013001 (2002).

[40] A.A. Aguilar-Arevalo *et. al*, Phys. Rev. Lett. **98**, 231801 (2007).

[41] M. Maltoni and T. Schwetz, Phys. Rev. **D76**, 093005 (2007).

[42] M. Apollonio *et. al*, Eur. Phys. J. **C27**, 331 (2003).

[43] S. Yamamoto *et. al*, Phys. Rev. Lett. **96**, 181801 (2006).

[44] J. Hosaka *et. al*, Phys. Rev. **D74**, 032002 (2006).

[45] Y. I. *et al.*, hep-ex/0106019.

[46] See For Instance M.G. Albrow *et. al*, FERMILAB-FN-0778-AD-E (*hep-ex/0509019*).

[47] D. A. *et al.*, hep-ex/0503053.

[48] M. G. *et al.*, hep-ex/0503053.

[49] J. Beacom and M. Vagins, Phys. Rev. Lett. **93**, 171101 (2004).

[50] W.M. Yao *et. al*, Journal of Physics G **33**, 1 (2006).

[51] Z. Maki, N. Nakagawa, and S. Sakata, Prog. Theor. Phys. **28**, 870 (1962).

[52] L. Wolfenstein, Phys. Rev. **D17**, 2369 (1978).

[53] S.P. Mikheyev and A.Y. Smirnov, Sov. J. Nucl. Phys. **42**, 1441 (1985).

[54] M. Blom and H. Minakata, New J. Phys. **6**, 130 (2004).

[55] V. Barger *et. al*, Phys. Rev. **D22**, 2718 (1980).

[56] Super-Kamiokande Collaboration, Nucl. Inst. Meth. **501A**, 418 (2003).

[57] M. Ishitsuka, Ph.D. Thesis, University of Tokyo (2004).

[58] S. Desai, Ph.D. Thesis, Boston University (2004).

[59] http://www-sk.icrr.u-tokyo.ac.jp/cause-committee/index-e.html.

[60] M. Honda *et. al*, Phys. Rev. **D64**, 053011 (2001).

[61] G. Battistoni *et. al*, Astropart. Phys. **19**, 269 (2003).

[62] G. Barr *et. al*, Phys. Rev. **D70**, 023006 (2004).

[63] P. Lipari, Astropart. Phys. **1**, 195 (1993).

[64] D. Perkins, Astropart. Phys. **2**, 249 (1994).

[65] Y. Hayato, Nucl. Phys. Proc. Supl. **112**, 171 (2002).

[66] D. Casper, Nucl. Phys. Proc. Supl. **112**, 161 (2002).

[67] C.H. Llewellyn-Smith, Phys. Rept. **3**, 261 (1972).

[68] R.H. Smith and E.J. Moniz, Nucl. Phys. **B43**, 605 (2002).

[69] R. Gran *et. al*, Phys. Rev. **D74**, 052002 (2006).

[70] D. Rein and L.M. Sehgal, Ann. Phys. **133**, 79 (1981).

[71] D. Rein, Z. Phys. **C35**, 43 (1987).

[72] T. Kitagaki *et. al*, Phys. Rev. **D34**, 2554 (1986).

[73] S.K. Singh *et. al*, Phys. Rev. **B416**, 23 (1998).

[74] D. Rein and L.M. Sehgal, Nucl. Phys. **B223**, 29 (1983).

[75] M. Gluck *et. al*, Z. Phys. **C67**, 433 (1995).

[76] M. Nakahata *et. al*, J. Phys. Soc. Jap **55**, 3786 (1986).

[77] T. Sjostrand, Compt. Phys. Commun. **84**, 72 (1994).

[78] R. Woods and D. Saxon, Phys. Rev. **95**, 577 (1954).

[79] L.L. Salcedo *et. al*, Nucl. Phys. **A484**, 577 (1954).

[80] D. Ashery *et. al*, Phys. Rev. **C23**, 2173 (1981).

[81] R. Brun and F. Carminati, CERN Programming Long Writeup **W5013** (1993).

[82] C. Zeitnitz and T.A. Gabriel, Nucl. Instrum. Meth. **A349**, 106 (1994).

[83] E. Bracci, CERN/HERA **72-1** (1972).

[84] A.S. Carroll *et. al*, Phys. Rev. **C14**, 635 (1976).

[85] A. Chavarria, http://www.phy.duke.edu/~schol/superk/alvaro_thesis.pdf, Senior Thesis, Duke University (2007).

[86] K. Nitta, Ph.D. Thesis, Osaka University (2003).

[87] E. Davies, *Machine Vision: Theory, Algorithms, Practicalities* (Academic Press, San Diego, 1976).

[88] A.M. Dziewonski and D.L. Anderson, Phys. Earth, Planet, Interiors **25**, 297 (1981).

[89] M. Chizhov, M. Maris and S.T. Petcov, *hep-ph/9810501* .

[90] O.L.G Peres and A.Yu. Smirnov, Nucl. Phys. **B680**, 479 (2004).

[91] G.L. Fogli *et. al*, Phys. Rev. **D66**, 053010 (2002).

[92] C.H. Albright and C. Jarlskog, Nucl. Phys. **B84**, 467 (1975).

[93] A. Bodek and U.K. Yang, Nucl. Phys. Proc. Suppl. **112**, 70 (2002).

[94] S.K. Singh and E. Oset, Phys. Rev. **C48**, 1246 (1993).

[95] K. Abe *et. al*, Phys. Rev. Lett. **97**, 171801 (2006).

[96] S. Agostinelli, Nucl. Instrum. Meth. **A506**, 250 (2003).